
GIANT MOLECULAR CLOUDS: A VIEW THROUGH
MOLECULAR TRACERS AND SYNTHETIC IMAGES

Camilo H Peñaloza C.

A THESIS SUBMITTED TO
CARDIFF UNIVERSITY
FOR THE DEGREE OF
DOCTOR OF PHILOSOPHY

21ST OF MARCH 2018

*“To exhibit the perfect uselessness of knowing the answer
to the wrong question”
Ursula Le Guin*

ACKNOWLEDGEMENTS

I'm thanking people

ABSTRACT

Line emission is strongly dependent on the local environmental conditions in which the emitting tracers reside. In this work, we focus on modelling the CO emission from simulated giant molecular clouds (GMCs), and study the variations in the resulting line ratios arising from the emission from the $J = 1 - 0$, $J = 2 - 1$ and $J = 3 - 2$ transitions.

We first study the ratio ($R_{2-1/1-0}$) between CO's first two emission lines and examine what information it provides about the physical properties of the cloud. To study $R_{2-1/1-0}$ we perform smooth particle hydrodynamic simulations with time dependent chemistry (using GADGET-2), along with post-process radiative transfer calculations on an adaptive grid (using RADMC-3D) to create synthetic emission maps of a MC. $R_{2-1/1-0}$ has a bimodal distribution that is a consequence of the excitation properties of each line, given that $J = 1$ reaches local thermal equilibrium (LTE) while $J = 2$ is still sub-thermally excited in the considered clouds. The bimodality of $R_{2-1/1-0}$ serves as a tracer of the physical properties of different regions of the cloud and it helps constrain local temperatures, densities and opacities.

Then to study the dependence line emission has on environment we perform a set of smoothed particle hydrodynamics (SPH) simulations with time-dependent chemistry, in which environmental conditions – including total cloud mass, density, size, velocity dispersion, metallicity, interstellar radiation field (ISRF) and the cosmic ray ionisation rate (CRIR) – were systematically varied. The simulations were then post-processed using radiative transfer to produce synthetic emission maps in the 3 transitions quoted above. We find that the cloud-averaged values of the line ratios can vary by up to ± 0.3 dex, triggered by changes in the environmental conditions. Changes in the ISRF and/or in the CRIR have the largest impact on line ratios since they directly affect the abundance, temperature and distribution of CO-rich gas within the clouds. We show that the standard methods used to convert CO emission to H_2 column density can underestimate the total H_2 molecular gas in GMCs by factors of 2 or 3, depending on the environmental conditions in the clouds.

One of the underlying assumptions in star formation is that stars are formed in long lived, bound molecular clouds. This paradigm comes from examining the virial parameter of molecular clouds. To calculate the virial parameter we rely on three quantities: velocity dispersion, size and mass, each of which have their own underlying assumptions, uncertainties and biases. It should come as no surprise that variations in these quantities can have a significant impact on our assessment of cloud dynamics and hence our overall understanding of star formation. We therefore use CO line emission from synthetic observation to study how the dynamical state of clouds changes as a

function of metallicity and to test how accurately the virial parameter traces these changes. First we show how the "observed" velocity dispersion significantly decreases with lower metallicities and how this is reflected on the virial parameter. Second we highlight the importance of understanding the intrinsic assumptions that go into calculating the virial parameter, such as how the mass and radius are derived. Finally, we show how the virial parameter of a cloud changes with metallicity and how the 'observed' virial parameter compares to the 'true' value in the simulation.

CONTENTS

List of Figures	4
1 Introduction	9
1.1 ISM phases	10
1.1.1 Multi-phase ISM	10
1.2 Heating and Cooling	13
1.3 Chemistry in the ISM	15
1.4 Giant Molecular Clouds	18
1.4.1 Dynamical state of clouds	19
1.4.2 CO-to-H ₂ conversion factor	21
1.4.3 Star formation rate	22
1.5 Synthetic Observations of CO	23
1.6 Aim of this Thesis	25
1.6.1 Thesis structure	26
2 Numerical Codes	27
2.1 Hydrodynamics	27
2.1.1 Smooth Particle Hydrodynamics	28
2.1.2 GADGET-2	29
2.2 Radiative Transfer	30
2.2.1 Line Transfer	31
2.2.2 Non-LTE line transfer	32
2.2.3 Ray-tracing	34
3 Numerical Methods	39
3.1 Achieving convergence	39
3.2 Sobolev-Gnedin approximation	46
4 Using CO line ratios to trace the physical properties of molecular clouds	51
4.1 Introduction	51
4.2 Method	53
4.2.1 Numerical setup	53
4.2.2 Post-processing	54
4.3 The CO 2-1 / CO 1-0 line ratio	55
4.3.1 CO emission maps	55
4.3.2 The value of $R_{2-1/1-0}$	57

4.3.3	The dependence of $R_{2-1/1-0}$ on density and temperature . . .	61
4.3.4	Optical depth effects	63
4.4	Discussion	66
4.5	Conclusions	66
5	CO line ratios in molecular clouds: the impact of environment	69
5.1	Introduction	69
5.2	Method	71
5.2.1	Initial conditions	71
5.2.2	Post-processing	72
5.3	Results	74
5.3.1	Cloud morphology and appearance	74
5.3.2	Systematic variations of R_{21}	76
5.4	R_{21} from observationally unresolved clouds	80
5.4.1	Averaged R_{21} for the whole cloud	81
5.4.2	CO emission as a probe of physical conditions	82
5.4.3	Alternative line ratios	83
5.5	Discussion	86
5.5.1	X_{CO} on unresolved clouds	86
5.5.2	R_{21} as a probe of CO abundance	89
5.6	Conclusions	91
6	Can the virial parameter reliably trace the dynamical state of molecular clouds?	93
6.1	Introduction	93
6.2	Method	95
6.3	Numerical and Observational techniques	95
6.3.1	Velocity Dispersion	95
6.3.2	Radius	96
6.3.3	Mass	97
6.3.4	Virial parameter	98
6.4	Results	99
6.4.1	σ , M and R	100
6.4.2	α Variability	105
6.5	Discussion	107
6.5.1	‘True’ values	107
6.5.2	Caveats and limitations	109
6.6	Conclusions	110
7	Summary	111
7.1	CO line ratios	111
7.2	Environmental dependence of CO emission	112
7.3	The virial parameter	112
7.4	Future Work	113
7.4.1	Global GMC evolution	113
7.4.2	Non-LTE effects	114

Bibliography**115**

LIST OF FIGURES

1.1	Image showing the different stages of star formation and how it is a multi scale process ranging from galactic scales to cloud scales (Kulesa et al., 2013)	10
1.2	Graph showing the thermal pressure equilibrium between the WNM-CNM phases of the ISM and its points of stability and instability. (Vazquez-Semadeni, 2009)	12
1.3	The different heating and cooling mechanisms in a typical molecular cloud. These results are obtained from hydrodynamical simulations that use time-dependant chemistry and a reduced chemical network (Glover & Clark, 2012b)	13
1.4	Image of the galactic plane as observed by CO. (Dame & Thaddeus, 2011; Dame, Hartmann & Thaddeus, 2001)	19
1.5	The Kennicutt-Schimdt relationship. (Kennicutt & Evans, 2012) . . .	22
1.6	An example of how different systematic effects as well as background contaminants can impact ideal synthetic observations. (Koeperl et al., 2017)	25
2.1	Schematic image that represents different ways in which a ray can interact with the medium when doing ray-tracing. a) an outer radiation source, b) an inner radiation source, c) a scattering event, d) a region with an optical depth near 1, e) a coarse regular outer grid, and f) rays to the observer Steinacker, Baes & Gordon (2013).	35
2.2	Image illustrating when a strong velocity gradient combined with a narrow linewidth profile results in a ray being unchanged by the medium.	36
3.1	Left: A schematic diagram representing how the nested structure of the tree where brown represents the base grid or tree, orange the branches i.e. no interacting cells and green the leaves, cells where physical properties will be interpolated. The diagram structure is meant to reflect the structure of the cell depicted on the right. Right: a single cell from the base grid with an overlapped distribution of SPH particles. The refinement of each cell is done according to the distribution of cells. Note that this is a 2-D schematic, however the refinement algorithm does this in 3-D.	40

3.2	A slice through the unstructured AMR grid created with our refinement algorithm. Each colour corresponds to a different, more refined layer of the grid	41
3.3	Checking interpolation	43
3.4	The cumulative luminosity from the PPV cube plotted against the brightness temperature of CO 1-0 (top panel) and CO 2-1 (bottom panel). The black solid line represents the resolution used for this study. The other lines correspond to different grid resolutions: the green dotted and red dotted lines correspond to fixed grids with resolutions of 256^3 and 512^3 respectively, while the remaining three lines correspond to different choices for the refinement criterion in the adaptive approach.	44
3.5	Similar plot to Fig. 3.4, however in this case the cumulative luminosity of the integrated intensity map is plotted against integrated intensity.	45
3.6	The setup of the grid used as an input for the radiative transfer. All the cells in the the front slice have the same density, temperature and velocity. The back slice has a temperature of 0 K. Densities and velocities take a value according to dv or $d\rho$, which are increased such that $dv = d\rho$ over the diagonal. dv is increase accordingly over the x -axis and $d\rho$ over the y -axis.	47
3.7	The integrated intensities of CO $J = 1 - 0$ for each run on each cube. Each row has a different method for calculating level populations: top = LTE, middle = LVG, bottom =LVG+. Similarly each column has a different number density for the front slice, left: $n = 50 \text{ cm}^{-1}$, middle: $n = 100 \text{ cm}^{-1}$, right: $n = 500 \text{ cm}^{-1}$. Note that even though the colours are similar the colourbar for each column is different	49
3.8	The image on the left shows the integrated intensity for CG15-M4-G1 with an LVG treatment while the middle image does so for LVG+. The image on the right is the ratio of LVG/LVG+ integrated intensities .	50
4.1	Top left: Column density of hydrogen nuclei, N_{gas} , at the end of the simulation. Since the gas in the cloud is primarily molecular, the H_2 column density is given approximately by $N_{\text{H}_2} \simeq N_{\text{gas}}/2$. Top right and bottom right: the velocity-integrated intensity of the cloud at the same time, for the $J= 1 - 0$ and $J= 2 - 1$ emission lines, respectively. Bottom left: the emission line ratio $R_{2-1/1-0}$, as defined in Equation 4.1.	56
4.2	(i) Probability density function (PDF) of $R_{2-1/1-0}$, illustrating its bimodal behaviour. (ii) Cumulative PDF of $R_{2-1/1-0}$. (iii) PDF of $R_{2-1/1-0}$, weighted by the integrated brightness temperature W_{CO} of the 1-0 line (red solid) or the 2-1 line (blue dashed-dotted). (iv) Cumulative version of (iii).	58

- 4.3 $R_{2-1/1-0}$, plotted as a function of the integrated intensity of the CO 1-0 line, W_{10} . Values are plotted for all pixels in the synthetic emission maps that have $W_{10} > 0.01 \text{ K kms}^{-1}$ and $W_{21} > 0.01 \text{ K kms}^{-1}$. The diagonal red dashed line indicate this selection criterion. Note that in practice, $R < 0.4$ when $W_{10} < 0.1 \text{ K kms}^{-1}$, so a number of points are removed that have $W_{21} < 0.01 \text{ K kms}^{-1}$ but $W_{10} > 0.01 \text{ K kms}^{-1}$ 60
- 4.4 Different physical quantities are plotted and colour coded with $R_{2-1/1-0}$: (i) N_{CO} vs $\langle T \rangle$; (ii) N_{H_2} vs $\langle T \rangle$; (iii) $\langle n \rangle$ vs $\langle T \rangle$; (iv) $\langle n \rangle$ vs N_{CO} 62
- 4.5 Panels i) and ii) show Integrated opacity image weighted by integrated intensity for both lines ($\tau_{W_{10}}$ and $\tau_{W_{21}}$ respectively). Panels iii) and iv) show τ_W , plotted as a function of $R_{2-1/1-0}$ for both lines illustrating how the ratio and opacity are correlated. Panels v) and vi) show $T_{\text{ex}}/T_{\text{kin}}$ plotted as a function of τ_W for each line and colour coded with $R_{2-1/1-0}$ the same colour scale as Fig. 4.4 64
- 5.1 Top row: Column density maps for simulations CG15-M4-G1, CG15-M5-G1, CG15-M5-G100 and GC16-Z1-G1. Middle row: The integrated intensity of the second rotational transition line of CO for each simulation. Bottom row: The ratio, R_{21} , of the integrated intensity of the first two rotational transition lines of CO for each simulation. . . 75
- 5.2 The cumulative PDF of R_{21} weighted by W_{CO} for different sets of clouds grouped by variations in their physical parameters. Top left: Small clouds ($10^4 M_{\odot}$), at solar metallicities and with varying ISRF, CRIR or both. Top right panel: Small clouds ($10^4 M_{\odot}$), with a solenoidal turbulent seed and varying metallicities. Bottom left panel: Large clouds ($10^5 M_{\odot}$) with variations in both ISFR and CRIR. Cyan lines are clouds that start atomic and yellow lines clouds with initial $n = 10000 \text{ cm}^{-3}$ Bottom right panel: Small clouds ($10^4 M_{\odot}$) with changes to α_{vir} , initial density or the turbulent seed 77
- 5.3 The averaged value of R_{21} for each cloud as a function of their respective ISRF (G_0). Large circles represent clouds that have a mass of $M = 10^5 M_{\odot}$ and small shapes represent clouds with a mass of $M = 10^4 M_{\odot}$. Blue, green and red shapes represent an increase of the ISRF and/or CRIR by 1,10 or 100 respectively. Xs, squares and triangles represent metallicities of Z_{\odot} , $0.5Z_{\odot}$ and $0.2Z_{\odot}$ respectively. Large cyan circles denote an initial hydrogen fraction of $f(\text{H}_2) = 0$. Yellow circles are the two runs with an initial number density of $n = 10000 \text{ cm}^{-3}$. Plus signs are clouds where the ISRF and the CRIR have been varied independently. Diamonds are the additional runs plotted in the bottom right panel of Figure 5.2 and have the same colours. Finally the dashed line represents the standard value used for converting W_{21} to W_{10} . Note: we have not included GC16-Z02-G100 since the gas is not able to form enough molecular gas and therefore there's little to none CO emission 81
- 5.4 The average temperature of H_2 as calculated by equation 5.2 plotted against the average temperature of CO. Each point represents a cloud and have the same colour and shapes as in Figure 5.3 83

5.5	Similar to Figure 5.3 but for $J = 3 - 2$ and $J = 2 - 1$ rotational transition lines. Colour coding is the same as in Figure 5.3. The dashed line is the commonly used value for R_{32} (Vlahakis et al., 2013)	84
5.6	Similar to the top panel of Figure 5.3 but for $J = 3 - 2$ and $J = 1 - 0$ rotational transition lines. The dashed line represents the commonly used conversion factor for R_{31} (Aravena et al., 2014)	85
5.7	X_{CO} plotted against ISRF for all the clouds using the same labels as in Figure 5.3. The line represents the typical value for X_{CO} and the shaded region the scatter as given by Bolatto, Wolfire & Leroy (2013). Note that clouds with metallicities of $Z \neq Z_{\odot}$ are not included	87
5.8	Shows the ratio of $N_{\text{obs}}/N_{\text{real}}$ against ISRF for all the clouds using the same labels as in Figure 5.3, where N_{obs} is calculated using R_{21} . Note that clouds with metallicities of $Z \neq Z_{\odot}$ are not included	87
5.9	Similar to Figure 5.8 but using R_{31} instead of R_{21}	88
5.10	Each coloured line represent a different simulation. Solid lines track the H_2 fractional abundance as a function of the number density of the gas. Dashed lines track the same behaviour but for CO	89
5.11	Illustrates how CO/ H_2 abundance ratio changes with average number density.	90
6.1	Top row: H_2 Column densities for GMCs with metallicities of $Z = Z_{\odot}$, $Z = 0.5Z_{\odot}$ and $Z = 0.2Z_{\odot}$ from left to right. Bottom row: Integrated intensities of the first rotational transition line of ^{12}CO for each cloud.	99
6.2	Figure showing how σ changes as a function of metallicity. Blue symbols represent quantities calculated from simulations while red symbols are calculated from synthetic observations.	100
6.3	Figure showing how R changes as a function of metallicity. Blue symbols represent quantities calculated from simulations while red symbols are calculated from synthetic observations.	101
6.4	Figure showing how σ as a function of metallicity. Blue symbols represent quantities calculated from simulations while red symbols are calculated from synthetic observations.	101
6.5	Graph showing the different values of α depending on the method used. α_{Gas} , α_{H_2} and α_{CO} represent the virial parameter calculated from the numerical simulations using Equation 6.7. α_{SOGas} is calculated by using Equation 6.1 and σ_{Gas} , R_{Gas} and M_{Gas} which are obtained directly from the numerical simulations. To calculate α_{RAMWX} , α_{RTMWX} , α_{RAZX} and α_{RTZX} we use Equation 6.1 and a different combinations of σ, R and M as derived from the synthetic observations. Finally each color represents clouds at different metallicities	106

CHAPTER 1

INTRODUCTION

Understanding the process of star formation is a complex and multi-scale problem, making the study of it all the more interesting and continually challenging. Even though the entire process for the formation of stars ranges over several orders of magnitude, both in time and space, it can also be understood as closed cycle of death and rebirth.

This cycle can be seen to start once molecular clouds are created, allowing for cold and dense gas to be formed. Gravitational instabilities and/or turbulence will then lead the cloud to fragment and create denser regions called cores. These cores can either disperse or further contract depending on how turbulent and massive they are. If the core further contracts it will start accreting surrounding material and eventually form a protostar. Protostars are young stellar objects (YSOs) embedded within dense material and are classified depending on how much of the YSO is exposed to direct observation. Once the YSO is fully exposed and the surrounding gas and dust has been completely dispersed, the star starts its steady evolution and reaches hydrostatic equilibrium, where the force of gravity is balanced out by hydrogen fusion. After its long evolution, and once the star runs out of fuel, the star dies, leading to chemical enrichment of the ISM and re-injection of turbulent energy, closing the cycle of star formation.

Figure 1.1 helps illustrate the different and necessary steps of this process in a simplified way. Particularly I am interested in studying the interstellar medium (ISM), since it is the link between galaxies and stars.

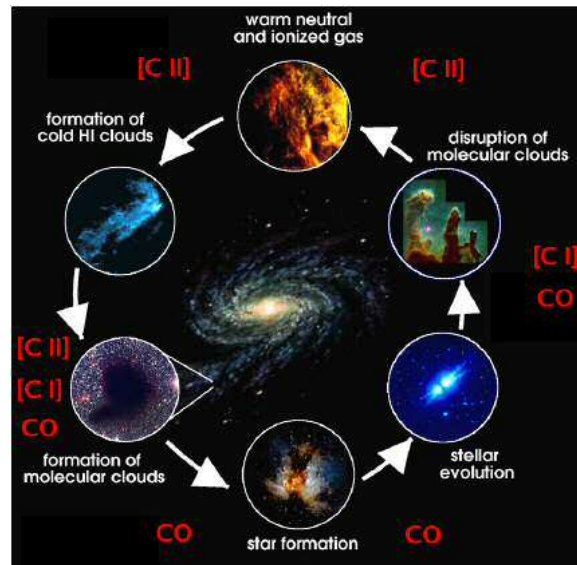


Figure 1.1. Image showing the different stages of star formation and how it is a multi scale process ranging from galactic scales to cloud scales (Kulesa et al., 2013)

1.1 ISM PHASES

The ISM is a multi-phase medium that is constantly changing, both dynamically and chemically. The chemical composition and physical state of the ISM is an important factor in mediating the onset of star formation. It follows then that understanding the different ISM phases as well as the different chemical components that comprise it is a key step in understanding the star formation process.

1.1.1 MULTI-PHASE ISM

The reason the ISM is often called a multi-phased medium is due to the fact that it spans an incredibly large range of temperatures ($10 - 10^6$ K) and densities ($10^{-2} - 10^8$ cm^{-2}). This idea of a multi-phased ISM originated from Field, Goldsmith & Habing (1969) where the equilibrium between the heating and cooling processes of the ISM would lead to pressure stable regions called phases. This division into phases of the ISM is a practical one and naturally assumes a static, stable and ideal picture of the ISM where the gas in each phase has the same physical properties. Needless to say, the ISM is a dynamically active medium where each phase has a boundary and the interaction between these boundaries will be unstable.

This picture has evolved throughout the years with larger number of stable and unstable phases being identified and definitions revisited. Nonetheless the ISM is commonly divided in the following 5 different phases that describe the temperature, density and chemical state of the gas. These values are summarized in Table 1.1.

Hot Ionized Medium (HIM)

The hot ionized medium (HIM) accounts for approximately $\sim 50\%$ of the total volume of the ISM and it mainly contains ionized hydrogen (HII). Shocks driven by stellar winds from massive stars or supernovae keep the gas very hot ($\sim 10^6$ K), ionized and diffuse ($\sim 0.003 \text{ cm}^{-3}$). Additionally supernova explosions help drive the ionization front even further and therefore contributing to the diffuse nature of the HIM. The HIM is observed through the UV emission, X-ray emission or synchrotron radiation.

Warm Ionized Medium (WIM)

The warm ionized medium (WIM), also thought of as HII regions, contains most of the HII in the galaxy, it is considerably colder (~ 8000 K) and denser ($\sim 0.3 \text{ cm}^{-3}$) than the HIM. Therefore the volume filling factor (f_V) of the HIM is about $\sim 10\%$ of the ISM. HII regions are mostly driven by young O-type stars and therefore mostly observed through optical or thermal radio emission.

Warm Neutral Medium (WNM)

As the name suggests, the warm neutral medium (WNM) is composed of neutral gas, most of it in the form of atomic hydrogen (HI). It takes up about $\sim 40\%$ of the volume of the ISM as well as contains most of the HI gas in the galaxy. As such, the WNM accounts for most of the HI emission and absorption in the ISM. HI emission is considered a proxy of star formation since it is considered to be a necessary step in the formation of H_2 and therefore stars.

Cold Neutral Medium (CNM)

The cold neutral medium (CNM) sits at much lower temperatures (~ 80 K) and higher densities ($\sim 50 \text{ cm}^{-3}$). As such it only accounts for about $\sim 1\%$ of the total volume of the ISM. The composition of the CNM is that of neutral atomic gas, similar to the WNM, however it is the very effective cooling of the ionized carbon hyperfine line ([CII]) that allows the gas to transition from a warm diffuse phase to a cold compact one. Therefore the CNM and the WNM are in thermal pressure equilibrium that is mediated by the heating and cooling mechanisms (See Figure 1.2).

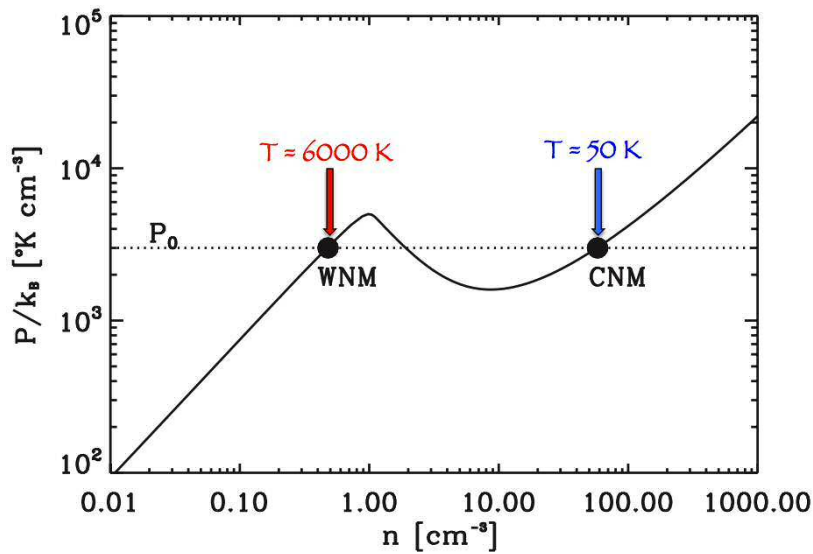


Figure 1.2. Graph showing the thermal pressure equilibrium between the WNM-CNM phases of the ISM and its points of stability and instability. (Vazquez-Semadeni, 2009)

Phase	$n(\text{cm}^{-3})$	$T(K)$	$M(10^9 M_{\odot})$	f_V
HIM	~ 0.003	10^6	–	$\sim 50\%$
WIM	0.1	8000	1.0	$\sim 10\%$
WNM	0.5	8000	2.8	$\sim 40\%$
CNM	50	80	2.2	$\sim 1\%$
GMC	$10^3 - 10^6$	10	1.3	$\sim 0.01\%$

Table 1.1. The density, temperature, mass and volume filling factor of the different phases of the ISM (Draine, 2011; Tielens, 2005).

Giant Molecular Clouds(GMCs)

The final phase of the ISM is reached once the densities are high enough ($> 10^3 \text{ cm}^{-3}$) so H_2 gas can quickly self-shield from the ambient UV radiation. This quickly increases the production of molecular gas creating gravitationally bound gas clumps called giant molecular clouds (GMCs), where the gas is cold (10 – 50 K) and thanks to the H_2 self shielding other more complex molecules start to form. Due to its compact nature GMCs account for a very small fraction ($\sim 0.01\%$) of the volume of the ISM. However, as we shall see in the next section they are a key step in the star formation process.

Naturally the interplay between heating and cooling mechanisms is what gives rise to the different ISM phases. Unfortunately this nicely defined picture of the ISM is still under much debate. There is a wealth of observational and numerical

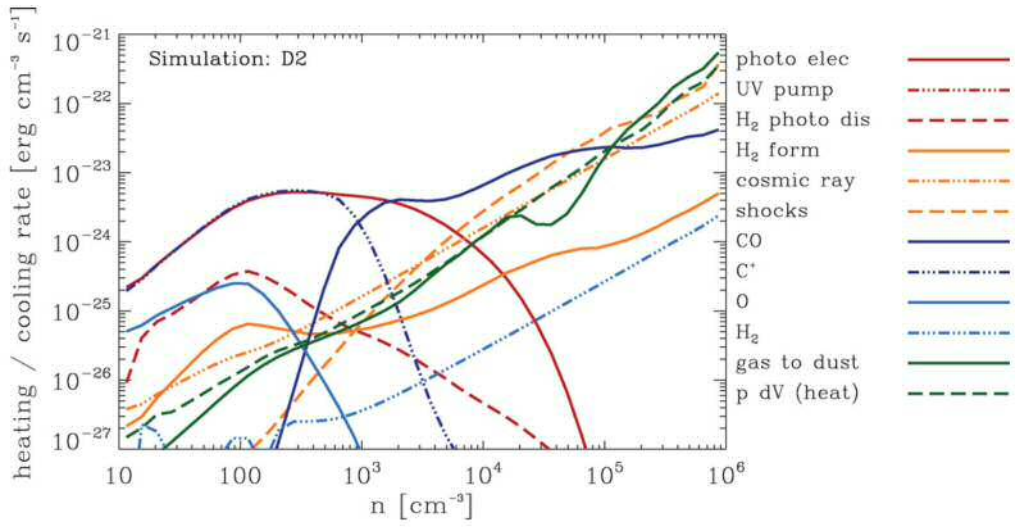


Figure 1.3. The different heating and cooling mechanisms in a typical molecular cloud. These results are obtained from hydrodynamical simulations that use time-dependant chemistry and a reduced chemical network (Glover & Clark, 2012b)

evidence that suggest the ISM is much more chaotic and unstable than initially pictured (Wolfire et al., 2003; Cox, 2005; Vazquez-Semadeni, 2009; Ostriker, McKee & Leroy, 2010). Some recent studies suggest that up to 50% of the ISM is in unstable phases (Begum et al., 2010; Heiles & Troland, 2003). What initially was conceived to be a 2 phase stable medium has quickly become a multi-phase dynamically unstable medium.

1.2 HEATING AND COOLING

As mentioned in the previous Section the different phases in the ISM are mediated by heating and cooling processes. These become increasingly important as the gas becomes colder and denser, enabling the formations of more complex chemical species. Figure 1.3 from Glover & Clark (2012b) illustrates the role different heating and cooling mechanisms play in the ISM as well as the regime in which they are important or negligible.

Figure 1.3 paints a clear picture of the many and diverse processes that are involved in the ISM heating and cooling. However upon further inspection it becomes evident that only a few dominate and this is well correlated with the average number density.

The interstellar radiation field (ISRF) (Draine, 1978) describes the constant influx of photons from different sources and at different wavelengths in the ISM. At low number densities ($n < 10^3 \text{ cm}^{-3}$) the dominant heating process is photoelectric

heating caused by UV photons that will heat or ionise the neutral gas as long as the densities, and therefore the total extinction (A_V), is low. A convenient way of quantifying the intensity of UV radiation in the ISRF is by defining a dimensionless parameter

$$G_0 \equiv \frac{u(6 - 13.6 \text{ eV})}{5.29 \times 10^{-14} \text{ erg cm}^{-3}}, \quad (1.1)$$

where the denominator is the estimate by Habing (1968) since it was the earliest estimate of intensity of the UV radiation and u the energy density integrated between 6 – 13.6 eV since this is the energy regime at which UV photons are responsible for photoelectric heating. By definition $G_0 = 1$ for a solar-like environment, however a more accurate estimate by Draine (1978) showed that in the solar neighbourhood $G_0 = 1.69$ in units of Habing (1968). Naturally the larger the radiation field the hotter the gas will get, usually this is regulated by the neighbouring star population.

The contrasting effect to the ISRF and the biggest coolant at low densities is the [CII] hyperfine line that emits at $\lambda = 158 \mu\text{m}$. The excitation energy of the first line, that is the difference between the ground state ($^2P_{1/2}$) and the first excited state ($^2P_{3/2}$), is $E_{3/2-1/2} = 91.21 \text{ K}$. The reason that [CII] is such an efficient coolant of the WNM and CNM has to do with the fact that the critical density (n_{cr}) of [CII] is much higher than the medium it sits in. The critical density is defined as the density at which the rate for spontaneous decay, usually denoted by the Einstein coefficient A_{ul} , is equal to the collisional de-excitation rate. That means if $n > n_{cr}$, for a particular species, then the gas is in local thermodynamic equilibrium (LTE) and the intensity will be that of a black body for a given frequency ν which is described by the Planck function. Given that for [CII] $n_{cr} \sim 10^3 \text{ cm}^{-3}$ (Note that the critical density is dependent on temperature), this means that for low densities ($n < 10^3 \text{ cm}^{-3}$) the [CII] hyperfine line will be sub-thermally excited. This explains why [CII] is such a good coolant of the ISM, since collisional excitations of $^2P_{3/2}$ will be radiated away and effectively remove energy of the gas. Additionally, photons emitted by the [CII] hyperfine line are quite energetic given their high frequency.

Moving onto higher densities, as H_2 begins to self-shield the ISRF is unable to penetrate the cloud and heat the gas. At which point cosmic rays, that are highly energetic protons, take over as one of the main heating sources in the interior of the cloud since they are able to penetrate the cloud. Whether this is the case or there is actually some shielding of cosmic rays its still a topic of much debate, since they can play a role in regulating the chemical processes within the cloud (Clark et al., 2013; Bisbas et al., 2017). The other main heating source comes from the turbulent

nature of the ISM that drives shocks of material that can eventually dissipate into warm gas. Once the gas temperature is under $E_{3/2-1/2} = 91.21$ K, then [CII] becomes unable to cool down any longer, CO takes over as the main coolant. This drives the temperatures of the cloud from $T \sim 100$ K to $T \sim 10$ K. This is only possible because there is now enough CO that is well shielded and able to emit.

Finally at very high densities (10^5 cm^{-3}) then another source of heating becomes important, pdV i.e. the work done by the gas as it starts to contract. At this point CO also becomes less efficient at cooling due to freeze-out and dust takes over. The dust is heated by collisions with gas particles which then is radiated away in the far-infrared and is always assumed to be optically thin emission. Thermal emission from dust, therefore how efficient it is at cooling, is a function of the dust-to-gas ratio as well as the grain size of the dust. This is true so long as the optical thin assumption holds, at column densities of $N \sim 10^{23} \text{ cm}^{-2}$ this assumption starts to break down. At what wavelengths this happens depends on several factors such as grain size and temperature as well as ice mantles covering the dust particles (Ossenkopf & Henning, 1994).

1.3 CHEMISTRY IN THE ISM

An important step into forming GMCs is the transition from an atomic medium to a molecular medium. The two most important molecules in the ISM are H_2 , since it accounts for most of the mass in a GMC, and CO, since it is an important cooling mechanism in the ISM as well as the second most abundant molecule in the ISM and main tracer of molecular gas.

H_2

H_2 can be formed in the ISM by radiative association i.e. collision of two H atoms, however this is a very slow process ($\sim 10^{-23} \text{ cm}^3 \text{ s}^{-1}$) since it is a strongly forbidden transition (Draine, 2011). Other processes such as three body collisions require very high temperatures and densities to be efficient. Therefore the dominant chemical channel for H_2 formation in the ISM is as follows:



Unfortunately the rate at which H_2 is formed through associative detachment, equation 1.3, is proportional to the density of H^- . Given the low densities of the ISM this makes forming H_2 quite inefficient. An additional problem is that H^- can be easily photo detached or destroyed by reacting with positively charged ions or protons. This is why the formation of molecular hydrogen relies on the existence of dust in the ISM. Dust grains compose about $\sim 1\%$ of the mass in the ISM at solar metallicities (Tielens, 2005). Surface grain chemistry or grain catalysis is the process through which dust grains act as chemical catalysts. Given that dust grains are much larger than H atoms, they can “trap” H atoms on its surface allowing them to react and create H_2 (Taquet, Ceccarelli & Kahane, 2012). Naturally the efficiency at which dust grains catalyse H_2 formation is dependent on the grain surface area.

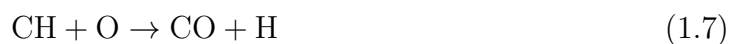
Unfortunately H_2 molecules can be easily destroyed by UV photons coming from the ISRF, this process is called photodissociation:



Photodissociation can effectively destroy most of the formed H_2 . Fortunately H_2 can self-shield once the densities are high enough, that is the H_2 molecules are effectively “shielded” from the ISRF since the medium becomes optically thick. H_2 can very efficiently self shield once column densities are larger than $N_{\text{H}_2} > 10^{20} \text{ cm}^{-2}$ (Klessen & Glover, 2016).

CO

Once number densities are high enough ($n \sim 0.01 \text{ cm}^{-3}$) CO can start to effectively form. The most common channel for CO formation is:



Equation 1.5 steadily produces CH_2^+ while equation 1.6 produces CH about a quarter of the time (Woodall et al., 2007). However to effectively produce CO the gas must be effectively shielded from UV photons in order to avoid photodissociation of CO



Note that the photodissociation processes described by equations 1.9,1.10 can result in other species, however, the importance here is concerning the destruction of CO and species which are important in its formation (Draine, 2011). More importantly the impact of photodissociation is reduced by the high H₂ abundances at these densities that shield the gas from UV photons. Eventually once CO abundance is high enough it can also start to self shield. Once the densities are high enough, CO is only efficiently destroyed by cosmic rays.



Chemical Modelling

Given the importance of chemical processes in the ISM, there has been a lot of effort dedicated to modelling these processes. However one of the biggest difficulties with chemical modelling is the complexity of such models, for example the UMIST Database for Astrochemistry contains over 2000 chemical reactions (Woodall et al., 2007). Chemical modelling usually involves solving a set of ordinary differential equations (ODE) and the computational cost is of N^3 where N is the number of species contained in the chemical network.

Great efforts have been made to create reliable chemical models of the ISM, which include highly complex chemical models. Work by (Bergin et al., 2004) or the more recent comprehensive review Röllig et al. (2007) studied different methods to accurately model chemical abundances within GMCs. Even though accurate the biggest drawback to these models is that their high complexity limits their applicability beyond 1D zone models.

An alternative approach has been the so called reduced chemical networks. By taking a choice of a set of limited chemical reactions this greatly reduces the computational cost without limiting the modelling power of the chemical network (Nelson &

Langer, 1999). The biggest advantage to this approach is that chemistry can be modelled within 3D hydrodynamical codes (Glover et al., 2010). Other work towards 3D chemistry modelling focus on following the chemical evolution and excitation states rather than dynamical evolution of the gas. Using this approach Bisbas et al. (2015) are able to model chemical evolutions while accounting for attenuation of the UV field from arbitrary sources as well as photodissociation and photoionization effects.

An important consideration when comparing different chemical models is their intended use. For example Glover & Clark (2012a) showed that the chemical approach by Keto & Caselli (2008) and Nelson & Langer (1997), and therefore the choice of chemical network, has a big impact when considering CO production since it overestimates the abundance of CO due to its simple treatment of carbon. At the same time these networks do an adequate job of modelling the temperature and density distributions of the gas when compared to more complex networks such as Nelson & Langer (1999) or Glover et al. (2010). Therefore the choice in network is highly dependent on its intended use which should be weighed against the computational efficiency.

1.4 GIANT MOLECULAR CLOUDS

GMCs can be considered as the final phase of the ISM and the first step towards the formation of stars. Following creation, evolution and destruction of molecular clouds is essential in understanding the star formation process. After all it is within GMCs that most of H_2 in the galaxy is contained, some of which will eventually be converted into stars. Therefore quantifying the total mass, most of it locked up in H_2 , as well as the dynamical state of GMCs is incredibly important as it sets an upper boundary to how many stars will eventually form. Additionally H_2 is a key chemical step in the formation of more complex molecules as seen above.

Ideally, as it is with many other phases of the ISM, we would like to directly observe and measure the total amount of H_2 within GMCs. Unfortunately due to the symmetric nature of molecular hydrogen, H_2 has no dipole moment and therefore no observable dipole rotational transitions. Moreover the very high excitation energies required to excite the quadrupole rotational transitions ($E/k \sim 510$ K for the first para transition) are well above the typical cold temperatures within GMCs. Therefore observers need to rely on emission from other molecules in order to estimate the total amount of H_2 in molecular clouds.

Fortunately the next most abundant molecule in the ISM is carbon monoxide (CO) and it is easily excitable within typical GMC conditions. The excitation energy

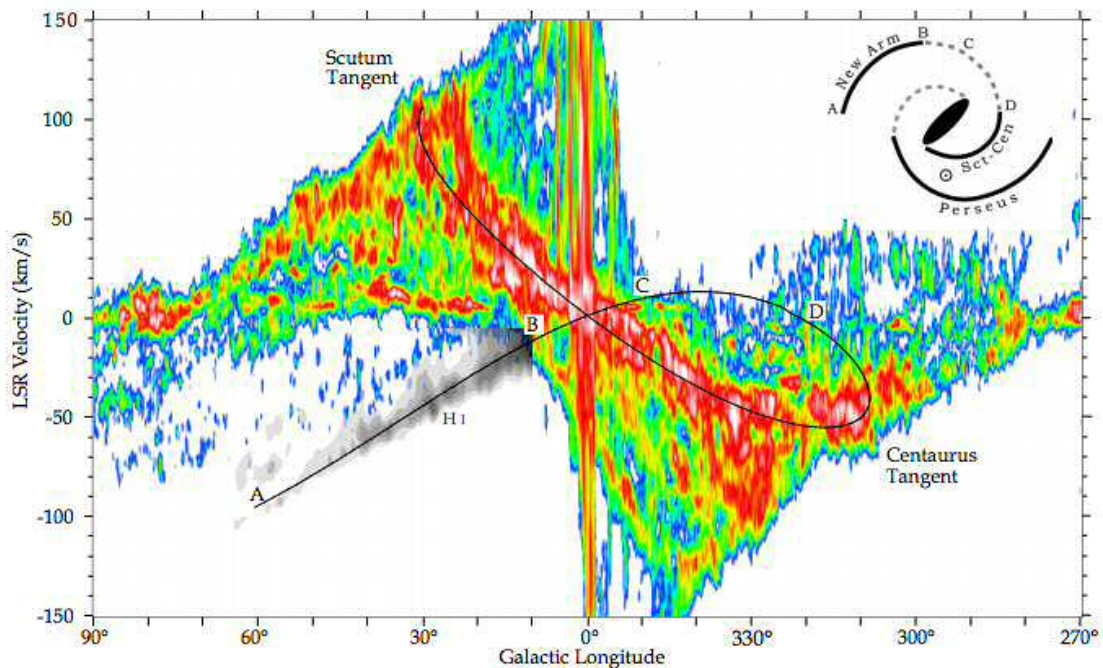


Figure 1.4. Image of the galactic plane as observed by CO. (Dame & Thaddeus, 2011; Dame, Hartmann & Thaddeus, 2001)

of the first rotational transition line ($J = 1 - 0$) is $E_{10} = 5.5$ K and has a critical density of $n_{\text{crit},1-0} \simeq 2000 \text{ cm}^{-3}$, both of which lie comfortably within typical GMC conditions. Moreover at a wavelength of $\lambda = 2.6$ mm the first rotational line can easily be observed from ground based telescopes. This makes CO the ideal tracer of molecular gas in the ISM.

For these reasons CO has become one of the most observed molecules in the ISM, not only in the Milky Way, but also in nearby Galaxies. A clear example of how much has been observed through CO emission lines is Figure 1.4, a position-velocity diagram of the galactic plane of the Milky Way. Figure 1.4 also highlights another important aspect of molecular line observation and that is the velocity information it contains. Having velocity information of a system is crucial in understanding the dynamical state it is in. In this case the velocity information is used to map the different spiral arms of the Milky Way.

1.4.1 DYNAMICAL STATE OF CLOUDS

Stars are formed in denser regions of GMCs that are collapsing under its own gravity i.e gravitationally bound. Whether a GMC is gravitationally bound depends on the interplay between gravity and turbulence. Early work by Larson (1981) used molecular tracers such as CO to study the dynamical state of clouds. What are now

called the Larson laws, describe the natural correlation between turbulence, gravity and size of GMCs that relate to its dynamical state. The three Larson relations are:

$$\sigma_v(\text{km s}^{-1}) = 1.10L^{0.38}(\text{pc}) \quad (1.13)$$

$$\sigma_v(\text{km s}^{-1}) = 0.42M^{0.2}(M_\odot) \quad (1.14)$$

$$n(\text{cm}^{-3}) = 3400L^{-1.1}(\text{pc}) \quad (1.15)$$

where σ_v is the velocity dispersion, L is the size of the cloud or surface of emission, M is the mass and n is the mean density. Equation 1.13 suggest the effect of turbulence on clouds has a power law relation with size. More importantly the exponent is very similar to that Kolmogorov's law, suggesting that structure is a consequence of the turbulent energy cascade. Equation 1.14 follows a positive correlation which is to be expected if clouds are roughly in virial equilibrium. This is confirmed by combining with equation 1.13 which yields $2GM/L\sigma^2 \sim 1$. Finally given the almost anti-linear relation of Equation 1.15 this implies that the surface density of molecular clouds is very similar.

From the Larson relationships it becomes evident that turbulence, gravity and size in GMCs are key in quantifying the dynamical state of clouds. A common way of doing this is through the virial parameter α_{vir} which relates the gravitational energy of the cloud to its kinetic energy describes. Bertoldi & McKee (1992) define an observationally derived virial parameter as

$$\alpha_{\text{vir}} = \frac{5R\sigma^2}{GM} \quad (1.16)$$

where R is the size of the cloud, σ its 1-D velocity dispersion and M its mass. In this case if $\alpha_{\text{vir}} > 2$ then the cloud is gravitationally unbound and being dispersed by turbulence, $\alpha_{\text{vir}} < 2$ the cloud is gravitationally bound, and if $\alpha_{\text{vir}} = 1$ the cloud is said to be in "virial equilibrium". Note that this is different from equipartition of gravitational and kinetic energy that happens when $\alpha_{\text{vir}} = 2$

Whether clouds are virialized, collapsing or dispersing is a topic of much debate (McKee & Ostriker, 2007). The majority of clouds analysed by Heyer et al. (2009) were found to be in virial equilibrium, while Roman-Duval et al. (2010) found that the median for the inner galaxy is $\alpha_{\text{vir}} \sim 0.5$. Alternatively, numerical studies found that GMCs within galactic simulations seem to be largely unbound (Dobbs, Burkert & Pringle, 2011).

1.4.2 CO-TO-H₂ CONVERSION FACTOR

Even though CO has been thoroughly observed within our galaxy, as well as in many extragalactic sources, CO emission is only a direct tracer of CO molecular gas. Since CO and H₂ formation are closely linked chemically, it follows that a simple relation could convert CO emission into H₂ column density. The empirical relation known as the “X-factor” is used to obtain the column density of H₂ by

$$N_{\text{H}_2} = X_{\text{CO}} W_{\text{CO}J=1-0}, \quad (1.17)$$

where $W_{\text{CO}J=1-0}$ is the integrated intensity of the first rotational emission line of CO, N_{H_2} is the column density of H₂ and X_{CO} is the empirically derived conversion factor and has an accepted value of $X_{\text{CO}} \approx 2 \times 10^{20} \text{ cm}^{-2}(\text{K km s}^{-1})^{-1}$ (Bolatto, Wolfire & Leroy, 2013). There are different methods through which the value for X_{CO} is derived empirically.

The first way is using the assumption that GMCs are in virial equilibrium, if this is the case then one can estimate the total virial mass by

$$M_{\text{vir}} = \frac{5\sigma^2 R}{G} \quad (1.18)$$

which follows from equation 1.16. This requires observations that are highly resolved, both in space and velocity, in order to accurately quantify the dynamical state of the cloud. Then by comparing the total CO luminosity (L_{CO}) with M_{vir} a strong correlation is found, this leads to the empirical relation $M_{\text{vir}} = \alpha_{\text{CO}} L_{\text{CO}}$ which is an alternative prescription of equation 1.17. The accepted value is $\alpha_{\text{CO}} = 4.6 M_{\odot} (\text{K km s}^{-1} \text{ pc}^{-2})^{-1}$ (Solomon et al., 1987; Scoville et al., 1987).

An alternative way of calculating the conversion factor is by using observations of other tracers. Using CO isotopologues (¹³CO, C¹⁸O), which given their lower abundance in the ISM, their emission is considered to be optically thin. This can then be used to obtain column density maps of that given isotopologue and then be converted into N_{CO} through abundance ratios between species. Effective extinction and assuming a dust-to-gas ratio can then be used to convert to N_{H_2} . Using this method Goldsmith et al. (2008) estimate the value to be $X_{\text{CO}} = 1.8 \times 10^{20} \text{ cm}^{-2}(\text{K km s}^{-1})^{-1}$.

Extinction in itself can also be used to estimate the conversion factor. This relies on how well extinction can be converted into column density which assumes linearity between extinction and column density. The biggest drawback being that it can only be used on nearby objects that are not obscured by any foreground contaminants. Pineda et al. (2010) estimate, using extinction mapping, that $X_{\text{CO}} = 1.8 \times 10^{20} \text{ cm}^{-2}(\text{K km s}^{-1})^{-1}$. On the other hand dust emission can also be used

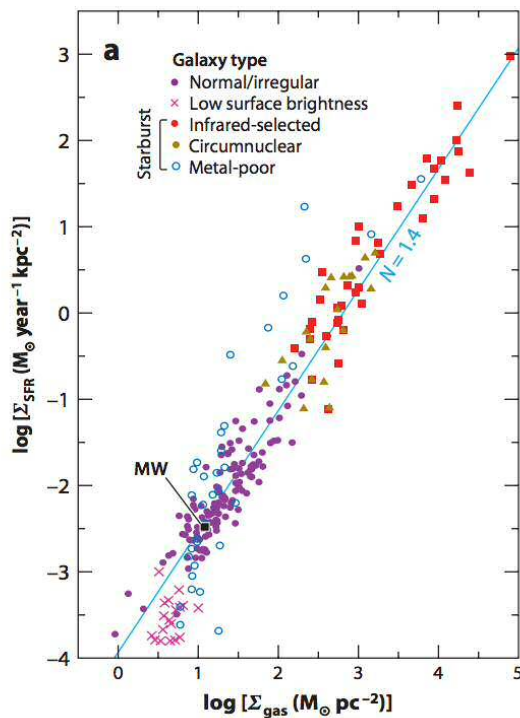


Figure 1.5. The Kennicutt-Schmidt relationship. (Kennicutt & Evans, 2012)

to obtain column densities at larger distances. The underlying assumption here is that the dust optical depth is a perfect tracer of column density if the dust-to-gas ratio is known. Using dust emission Dame, Hartmann & Thaddeus (2001) estimate $X_{\text{CO}} = 2.1 \times 10^{20} \text{ cm}^{-2} (\text{K km s}^{-1})^{-1}$. Needless to say, both these methods require a comparison with W_{CO} to obtain an estimate of the X-factor.

Even though X_{CO} is widely used it still remains subject of much study and debate as many have pointed out (Bolatto, Wolfire & Leroy, 2013; Sandstrom et al., 2013; Shetty et al., 2011; Clark & Glover, 2015).

1.4.3 STAR FORMATION RATE

Star formation is the process through which gas is converted into stars. In the paper by Schmidt (1959) and then followed by Kennicutt (1998) studied whether the surface density of star formation (Σ_{SFR}) is well correlated with the gas surface density (Σ_{gas}). Figure 1.5 shows the Kennicutt-Schmidt from a recent review paper (Kennicutt & Evans, 2012).

Even though there is some scatter the Kennicutt-Schmidt relationship shows super-linear correlation between Σ_{SFR} and Σ_{gas} . Moreover it shows that star formation is an inefficient process. Further detailed studies estimate the star formation efficiency

for individual clouds to be between 2% and 8% (Evans et al., 2009; Peterson et al., 2011).

However some recent results question the super-linearity of the Kennicutt-Schmidt relationship, suggesting that depending on the sample and method taken it can have a sub-linear relationship (Bigiel et al., 2008). Other studies suggest that the Kennicutt-Schmidt relation might not be universal after all, owing to observational biases such as CO gas being associated with non-star forming regions (Shetty, Kelly & Bigiel, 2013). Another source of confusion can be the already mentioned “X-factor” used to estimate the total molecular gas in Figure 1.5.

1.5 SYNTHETIC OBSERVATIONS OF CO

Numerical astrophysics has been a growing field in the last couple of decades. The constant increase in computational power has opened up the door to ever more complex and detailed numerical simulations that incorporate different types of physics. As such, they can help test our current understanding and provide key insights about the star formation process. Recently synthetic observations have become a new way of using numerical simulations to better compare theoretical results to observations.

Synthetic observations are defined “to be a prediction, based on theoretical models, of the manner in which a particular astrophysical source will appear to an observer” (Haworth et al., 2017). Synthetic observations can vary in level of complexity from simple analytic models to full radiative transfer calculations that include instrumentational effects. The level of complexity is naturally limited by computational capabilities. In the context of GMCs and the ISM, synthetic observations of CO can help understand the nature of the tracer, its biases and limitations, as well as improve on current methods and techniques. To do so requires a dynamical model of the GMC’s evolution that tracks the dynamics of the gas as well as the chemical abundances of different species. This is followed with post process radiative transfer that models the emission, absorption and optical effects of molecular species or dust. The resulting image or spectrum is considered to be an ideal synthetic observation that can then be further post processed to include instrumentational effects.

Early models of the dynamical evolution of clouds were analytical, in recent years there has been much work done using numerical simulations to recreate realistic GMCs. Given the importance turbulence plays in the ISM, much of the substructure in the ISM, such as filaments and cores, is thought to be a consequence of the log-normal distribution of turbulence (Padoan & Nordlund, 2002). However studies by Vázquez-Semadeni et al. (2008) suggest that the log-normal distribution is

complemented by a power law tail when considering the dynamics of cores forming within GMCs. An additional point of debate has been the nature of the turbulence field, whether it is driven by solenoidal or compressive modes. Federrath, Klessen & Schmidt (2008) studied the effect of different turbulent modes of the probability density distribution and found that compressive modes produce a larger deviation in the density distribution. With this in mind, early work by Ossenkopf (2002) post-processed turbulent clouds modelled by Klessen (2000). The main result of this work was showing that the opacity of molecular line emission of ^{13}CO can have a significant effect in detecting the formation of cores from turbulent modes.

One of the biggest caveats of this work was the lack of chemical modelling to follow the evolution of the chemical abundances of different species. This is why the efforts in improving chemical modelling as exposed above have been important for the development of synthetic observations. Building on this there has been a big effort in extending simple PDR codes into full radiative transfer codes that can post-process the self-consistently modelled GMCs. A review on dust radiative transfer methods can be found in Steinacker, Baes & Gordon (2013). Additionally there exist several codes that do line transfer as well as consider non-LTE solutions to the radiative transfer equation (Dullemond, 2012; Harries, 2011; Reissl, Wolf & Brauer, 2016).

A good example of the use of synthetic observations is a recent paper by Clark & Glover (2015) where they test the accuracy of X_{CO} as a conversion factor between CO emission and H_2 column density. By comparing the emission of the first rotational emission line of CO, as seen through synthetic observations, with the column density as calculated from the simulation they were able to estimate a value for X_{CO} . Their results show that X_{CO} is highly sensitive to the surrounding ISRF as well as the CRIR.

Other examples include work by Haworth et al. (2015a,b) that study the effect of viewing angles in massive star formation. Synthetic observations have the advantage that a same object can be viewed from different angles and therefore shed some light on projection effects. They produce CO synthetic emission by looking at cloud-cloud collisions modelled by Takahira, Tasker & Habe (2014). Their results show that a “broad bridge feature” appears when looking at position-velocity diagrams suggesting it could be a observational feature of clouds formed through collisions.

A more complete example of synthetic observations is the work done by Koepferl et al. (2017) where they consider the effect of background emission and considering observational contaminants. Hydrodynamical simulations by Dale et al. (2014), that include feedback from both photoionization and momentum-driven winds, are first post-processed to create continuum observations. In their results they caution how

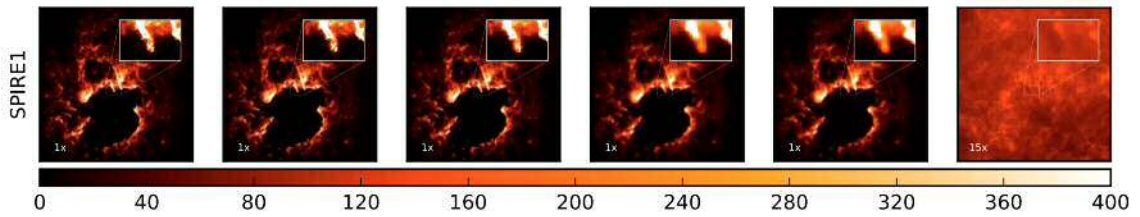


Figure 1.6. An example of how different systematic effects as well as background contaminants can impact ideal synthetic observations. (Koeferl et al., 2017)

interstellar reddening, PSF convolution or thermal noise can significantly change the results and therefore considering these effects is incredibly important when accounting for the predictive power of synthetic observations (See Figure 1.6).

From these few examples, it is abundantly clear that understanding the limitations of a fundamental tracer such as CO is key in the improvement of star formation theories. Moreover, given the ubiquitous use of CO, further understanding of the tracer can lead to previously unseen correlations that highlights key properties of GMCs. With this in mind, synthetic observations of CO are the ideal method to help improve our knowledge of the tracer, determine its validity and further explore new ways of developing scientific knowledge.

1.6 AIM OF THIS THESIS

In this thesis we make use of synthetic observations to mimic observations of numerically evolved GMCs. To model the evolution of a GMC we use an SPH code (GADGET-2) with time-dependent chemistry to accurately model the heating and cooling of the ISM. More importantly the H_2 and CO chemistry is vital to track the chemical abundances that are a key part in the production of synthetic observations. Then synthetic emission maps are created with the publicly available radiative transfer code (RADMC-3D) by post-processing the SPH snapshot.

The main aim of this thesis is to use synthetic observations of CO to answer the following questions:

- Do line ratios of CO emission lines help trace the physical properties of the gas within GMCs?
- Are line ratios sensitive to environmental and initial conditions of GMCs? If so how sensitive are they?
- Do the uncertainties, biases and limitations of CO as a tracer affect the interpretation of the dynamical state of clouds?

1.6.1 THESIS STRUCTURE

The structure of this thesis goes as follows. Chapter 2 briefly describes the different numerical codes needed to create synthetic observations. Mainly focusing on hydrodynamics (GADGET-2), chemistry and radiative transfer (RADMC-3D). Chapter 3 expands on some technical improvements made to RADMC-3D to make the post processing more efficient and reliable. Chapter 4 is mostly based on work published in Peñaloza et al. (2017) and examines how the ratio of the first two rotational transition lines can serve as a probe of physical conditions within GMCs. Chapter 5 is mostly based on work published in Peñaloza et al. (2018) and studies the impact of environment on CO. More specifically looking at how the ratios of the first rotational transition lines of CO vary as the initial conditions and surrounding environment of GMCs changes. Chapter 6 focuses on how numerical simulations and synthetic observations differ when studying the dynamical states of clouds, by studying how the virial parameter(α) changes depending on the assumptions and methods used. Finally Chapter 7 summarizes the main results of this thesis and future work.

CHAPTER 2

NUMERICAL CODES

This chapter briefly describes the numerical codes and numerical techniques used to produce the main results of this thesis.

2.1 HYDRODYNAMICS

The evolution of fluids, liquids and gases, can be described using the equations of hydrodynamics. The equations for ideal hydrodynamics are:

$$\frac{\partial \rho}{\partial t} + \nabla \cdot (\rho \mathbf{v}) = 0 \quad (2.1)$$

$$\rho \frac{\partial \mathbf{v}}{\partial t} + (\rho \mathbf{v} \cdot \nabla) \mathbf{v} + \nabla P + \rho \mathbf{g} = 0 \quad (2.2)$$

$$\frac{\partial \epsilon}{\partial t} + \mathbf{v} \cdot \nabla \epsilon + \frac{P}{\rho} \nabla \cdot \mathbf{v} = 0 \quad (2.3)$$

These set of equations model how an ideal fluid, i.e non-viscous and non-dissipating fluid, behaves. The continuity equation (2.1), momentum conservation equation (2.2) and energy conservation equation (2.3) describe how the density ρ , the velocity \mathbf{v} , the specific internal energy ϵ and the pressure P behave in a fluid. In order to solve these equations one needs an equation of state that relates P and ρ . For the ISM, and in general for astrophysics, the equation of choice is the so called polytropic equation

$$P = P_0 \left(\frac{\rho}{\rho_0} \right)^\gamma. \quad (2.4)$$

where γ is the polytropic index, usually taken to be 5/3 for a monoatomic gas. These set of equations can be solved analytically, albeit for a very specific set of conditions.

Therefore to describe the motions of a fluid in a non-linear system, such as the ISM, we need numerical models that solve the equations of hydrodynamics.

The two main numerical approaches for solving these equations are either Eulerian or Lagrangian. The Eulerian approach considers the changes in time of the fluid's physical variables with respect to a fixed frame of reference. Therefore at each fixed position in space each variable can be integrated in order to evolve the gas. Conversely the Lagrangian approach considers a comoving frame of reference. That is the physical variables are evolved with respect to the fluid element rather than a fixed position.

2.1.1 SMOOTH PARTICLE HYDRODYNAMICS

Smooth particle hydrodynamics (SPH) is a Lagrangian approach to solving the equations of hydrodynamics, where a continuous fluid is divided into an ensemble of particles that described a fluid element. The concept of SPH was first developed by Lucy (1977) and separately by Gingold & Monaghan (1977).

A given fluid element A, can be "smoothed" when convolved with a kernel function W such that:

$$\langle A(\mathbf{r}) \rangle = \int A(\mathbf{r}') W(\mathbf{r} - \mathbf{r}', h) d\mathbf{r}'. \quad (2.5)$$

where $W(\mathbf{r} - \mathbf{r}', h)$ is the kernel function with a length scale h centred at \mathbf{r} .

Kernel

The kernel function W can, in principle, have any form so long as it satisfies two conditions. It must approximate to a Dirac delta function as $h \rightarrow 0$ and it must be normalized to unity. In the original paper Lucy (1977) used a Gaussian kernel that is computationally expensive since it requires integrating over all particles for any given fluid element. Most SPH codes, as well as GADGET-2, use a cubic spline kernel defined as

$$W(r, h) = \frac{1}{\pi h^3} \begin{cases} 1 - \frac{3}{2}(\frac{r}{h})^2 + \frac{3}{4}(\frac{r}{h})^3 & \text{for } 0 < \frac{r}{h} < 1 \\ \frac{1}{4}(2 - \frac{r}{h})^3 & \text{for } 1 < \frac{r}{h} < 2 \\ 0 & \text{otherwise} \end{cases} \quad (2.6)$$

The kernel function is defined to be 0 when $r > 2h$, making the integration for a fluid element only over neighbouring particles. This means that Equation 2.5 can be approximated to

$$\langle A(\mathbf{r}_i) \rangle = \sum_j \frac{m_j}{\rho_j} A_j W(\mathbf{r}_i - \mathbf{r}_j, h) \quad (2.7)$$

where $d\mathbf{r}'$ can be approximated to $\sim \frac{m_j}{\rho_j}$ provided that there are enough neighbouring particles in order to properly sample the kernel.

Smoothing Length

How large the smoothing length h is will determine the number of neighbouring particles. Thus choosing an appropriate value for h is important in order to optimize noise vs accuracy. The smoothing length is normally defined by

$$h_i = \eta \left(\frac{m_i}{\rho_i} \right)^{1/3} \quad (2.8)$$

where η is used to determine the number of neighbouring particles. ρ_i is defined by

$$\rho_i = \sum_{j=1}^N m_j W(\mathbf{r}_i - \mathbf{r}_j, h_i). \quad (2.9)$$

In this way the interdependence between h and ρ is used to determine a fixed number of neighbours. According to Price & Monaghan (2004) for a value of $\eta = 1.2$ this results in ~ 58 neighbours.

2.1.2 GADGET-2

In this thesis we use GADGET-2 (Springel, 2005) to model and solve the hydrodynamic equations. In comparison with the standard SPH prescription GADGET-2 defines and uses the smoothing length and kernel differently. In GADGET-2 Equation 2.6 is defined such that $r > h$ instead of $2h$, this is for consistency with previous work from Springel, Yoshida & White (2001). Additionally the smoothing length h is defined such that the mass within a certain volume defined by h is constant and obey the following equation

$$\frac{4\pi}{3} h_i^3 \rho_i = N_{sph} \bar{m}, \quad (2.10)$$

where N_{sph} is the number of neighbours and \bar{m} the average particle mass. The reason behind this is that in GADGET-2 a fluid element is defined in terms of the entropy per unit mass rather than the thermal energy per unit mass.

Because GADGET-2 was initially designed as a cosmological simulations code, it lacks some of the important physics required to model the ISM. The two main

addition of importance for the work carried out in this thesis are chemistry and the attenuation of the ISRF.

The work carried out by Glover & Mac Low (2007a,b) is the main basis for the H₂ chemistry in GADGET-2. Using time-dependant chemistry means that the heating and cooling of the gas is self-consistently calculated and therefore there is no need to use an equation of state. Moreover, as seen previously H₂ formation is a key step in the formation of GMCs as well as more complex molecules. However, in order to accurately model the formation of H₂ it is important to account for its self-shielding, this requires a precise calculation of the column density. Clark, Glover & Klessen (2012) developed a computationally efficient technique to calculate column densities using the gravitational tree already incorporated in GADGET-2.

Given the main focus of this work is to study the diagnostic power of rotational line emission from CO, it is imperative that the chemical abundance of CO is reliable. Glover & Clark (2012a) studied different chemical networks that varied in complexity and concluded that the chemical network described in Nelson & Langer (1999) is computationally cheaper without much cost on precision. Therefore for all the results presented here we make use of this network.

2.2 RADIATIVE TRANSFER

In astrophysics and in the ISM radiation is the only way to diagnose and probe astrophysical systems. It is the main link between observations and theory. The main assumption in modelling radiation transport is that light, i.e. photons, can be approximated to ray of light that travel in straight lines, this assumption ignores the more complex behaviours of light as described by Maxwell's equations. However, this assumption holds because the scale of astrophysical systems is much larger than the wavelength (λ) of radiation, meaning we are considering a macroscopic propagation of light.

Modelling the propagation of straight rays, is in principle a simple task. Specially considering that the specific intensity of a source at a given frequency (I_ν) is constant along the ray or otherwise stated $dI_\nu/ds = 0$. However the complexity when modelling radiative transfer, and the reason it is computationally expensive and numerically challenging, arises when considering that radiation can change the state of matter (heating, cooling, ionization, etc) which in turn affects the energy of the system and therefore the radiation itself. To complicate things further scattering events can change the direction of the rays.

The radiative transfer equation describes the propagation of radiation through

a medium and is given by

$$\frac{dI_\nu}{ds} = j_\nu - \alpha_\nu I_\nu, \quad (2.11)$$

where I_ν is the specific intensity at a given frequency ν is determined by the emissivity coefficient j_ν and the absorption coefficient α_ν , which is commonly expressed in terms of the opacity (τ) such that

$$d\tau_\nu = \alpha_\nu ds. \quad (2.12)$$

Note that if $\tau > 1$ the medium is considered to be optically thick, that is a photon propagating over a distance s will most likely be absorbed by the medium. Conversely $\tau < 1$ is an optically thin medium through which a photon will pass through unaffected. Since τ is a dimensionless quantity, Equation 2.11 is sometimes rewritten as

$$\frac{dI_\nu}{d\tau} = -I_\nu + S_\nu, \quad (2.13)$$

where the source function is defined as $S_\nu \equiv j_\nu/\alpha_\nu$. Note that in local thermal equilibrium (LTE) the source function is the Planck function $B_\nu(T)$ i.e. blackbody radiation.

2.2.1 LINE TRANSFER

Line radiative transfer is also described by equation 2.11, however in this case emission and absorption are defined by level transitions which obey the rules of quantum mechanics. In simple terms, for two given energy levels E_i and E_j where $E_j > E_i$ it then follows that j_ν and α_ν are

$$j_\nu = \frac{h\nu}{4\pi} n_j A_{ji} \phi(\nu) \quad (2.14)$$

$$\alpha_\nu = \frac{h\nu}{4\pi} (n_i B_{ij} - n_j B_{ji}) \phi(\nu) \quad (2.15)$$

where n_i and n_j are the number densities of atoms or molecules occupying levels i and j , ϕ_{nu} is the line profile function that describes the broadening of the emission about a central frequency ν and A_{ji}, B_{ij}, B_{ji} are the Einstein coefficients. The Einstein coefficients each represent different forms in which level transitions can occur: A_{ji} is the spontaneous emission, B_{ij} is the absorption and B_{ji} is the stimulated emission. More importantly these coefficients obey the following relations

$$g_i B_{ij} = g_j B_{ji} \quad (2.16)$$

$$A_{ji} = \frac{2h\nu^3}{c^2} B_{ji}. \quad (2.17)$$

where h is the Planck constant and, g_i and g_j the statistical weights of each level. These relations greatly simplify the solving the radiative transfer equation given that only one need to be known to calculate the other two.

Given that the line transitions are strictly defined by quantum mechanics this means that the energy difference between levels determines the frequency at which a medium will absorb or emit i.e. $h\nu = E_j - E_i$. Therefore how populated each level is will determine how much energy is lost through emission and at what frequency. A simple example for calculating the level populations is when considering a system that is in LTE. Since in LTE the source function is equal to the Planck function, then the relative level populations are given by the Boltzmann equation such that

$$\frac{n_j}{n_i} = \frac{g_j}{g_i} \exp(-h\nu/kT) \quad (2.18)$$

where T is the temperature of the gas. The LTE assumption makes line radiative transfer relatively simple, provided the temperature and abundance of the molecule/atom in question are known. In addition, there are several databases that contain the values of the Einstein coefficients that have been calculated in laboratories. RADMC-3D uses the LAMDA database (Schöier et al., 2005).

2.2.2 NON-LTE LINE TRANSFER

Unfortunately in the ISM there are several cases where the LTE assumption breaks i.e. lines are sub-critically excited. In a non-LTE scenario we need to consider collisions between the molecule in question and the medium, which can directly affect the population levels. Therefore equation 2.18 does not hold for $T_{\text{gas}} \neq T_{\text{ex}}$, therefore to calculate the level populations one needs to solve the following statistical equilibrium equation

$$\begin{aligned}
& \sum_{j>i} \left(n_j A_{ji} + (n_j B_{ji} - n_i B_{ij}) J_{ji} \right) \\
& - \sum_{j<i} \left(n_i A_{ij} + (n_i B_{ij} - n_j B_{ji}) J_{ij} \right) \\
& + \sum_{j \neq i} \left(n_j C_{ji} - n_i C_{ij} \right) = 0
\end{aligned} \tag{2.19}$$

where C_{ij} and C_{ji} are the collisional coefficients and J_{ij} the integrated mean intensity given by

$$J_{ij} = (1 - \beta_{ij} S_{ij}) + \beta_{ij} J_{ij}^{\text{bg}} \tag{2.20}$$

where β_{ij} is the escape probability for a given line, S_{ij} is the source function and J_{ij}^{bg} is any background radiation that is present. Note the dependence of between levels, given that a transition from level i to level j will populate level j and depopulate level i , and vice-versa. This creates a set of N_{levels} coupled linear equations that need to be iterated given the interdependence between intensity and the level populations. Successfully and efficiently iterating these set of equations constitutes one of the main challenges of line radiative transfer modelling.

To fully solve equation 2.19 one requires to know the global properties of the gas. This can be computationally very expensive since iterating over every single cell element in order to update the level populations can be very slow. Code like TORUS (Harries, 2011) or LIME (Brinch & Hogerheijde, 2010) can perform full non-LTE radiative transfer. However, computationally cheaper alternatives exist where the problem is reduced to a local one by some approximation, in the ISM the most common approximation, given the turbulent nature of the ISM, is the Sobolev approximation.

The Sobolev Approximation

The Sobolev approximation, most commonly know as the Large Velocity Gradient (LVG) approximation, is widely used when calculating the level populations of a gas within GMCs. In the original paper, Sobolev (1957) studied the idea that emission coming from gas within a moving medium will be doppler shifted before it can be reabsorbed and therefore escapes. Whether a photon escapes or not is determined by the velocity gradient ($|\nabla \vec{v}|$), i.e. the larger $|\nabla \vec{v}|$ is the smaller the area where the

photon can be reabsorbed. RADMC-3D can perform the Sobolev approximation when calculating level populations, the detailed implementation can be found in Shetty et al. (2011).

Even though Ossenkopf (1997) showed that the Sobolev approximation is a robust approximation for GMCs, the method is still limited by the fact that it only considers changes in velocity. When using the Sobolev approximation the aim is to calculate the probability that a photon will escape a given area. The escape probability is given by:

$$\beta = \frac{1 - e^{-\tau_v}}{\tau_v} \quad (2.21)$$

where τ_v is the optical depth given a velocity gradient. τ_v can be calculated by

$$\tau_v = \frac{c^3}{8\pi\nu_{ij}^3} \frac{A_{ij}n}{1.064|\nabla\vec{v}|} \left(f_j \frac{g_i}{g_j} - f_i \right), \quad (2.22)$$

where ν_{ij} is the emission frequency of the transition, g_i and g_j are the statistical weights for each level, n the total number density and, f_i and f_j is the fractional population level (van der Tak et al., 2007).

2.2.3 RAY-TRACING

Once the local conditions for emission and absorption for the medium have been calculated we require a method to model the propagation of radiation through the medium. The most common method is ray-tracing where a ray models the change in intensity along a particular direction. To calculate the change in intensity one needs to integrate the radiative transfer equation (2.11) along the ray. The difficulty of ray-tracing arises when considering the different interactions the radiation can have with the medium, Figure 2.1 shows a schematic representation of this.

Correctly accounting for all these effects is very important in order to guarantee the accuracy of the final image or spectra of the modelled object. We consider only a few of the relevant ones for line radiative transfer below, but note that RADMC-3D can account for several more.

Doppler Catching

As mentioned above being in a turbulent medium, such as the ISM, means that lines can be easily doppler shifted, this can be a potential problem when performing the ray trace. Consider a scenario where we are examining the change in intensity for

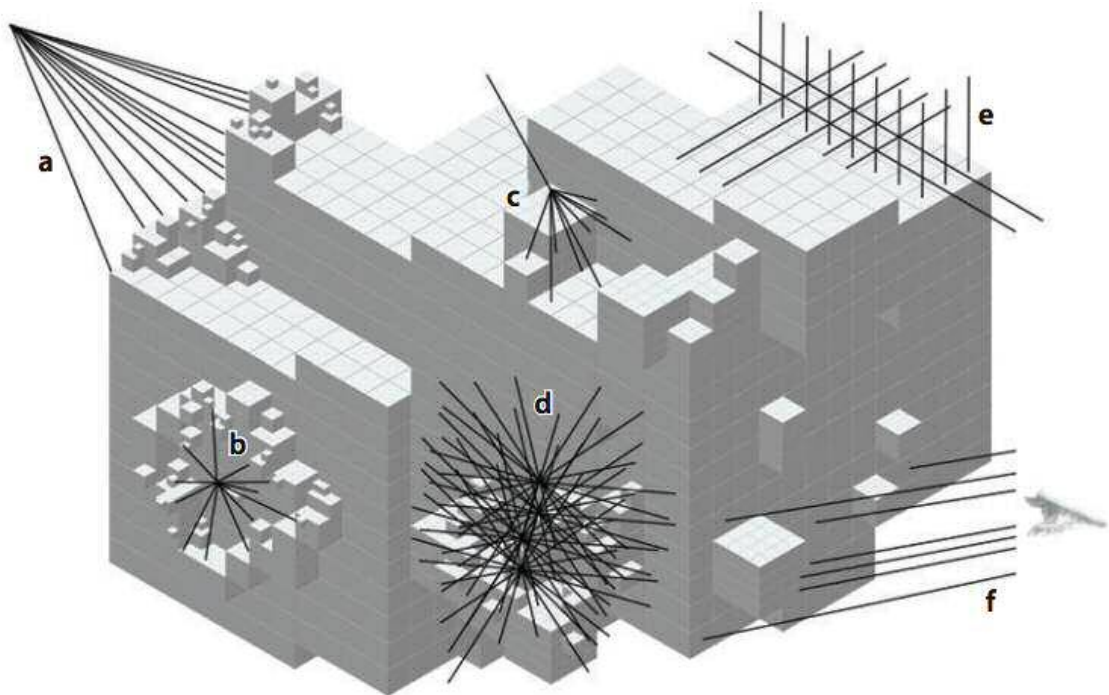


Figure 2.1. Schematic image that represents different ways in which a ray can interact with the medium when doing ray-tracing. a) an outer radiation source, b) an inner radiation source, c) a scattering event, d) a region with an optical depth near 1, e) a coarse regular outer grid, and f) rays to the observer Steinacker, Baes & Gordon (2013).

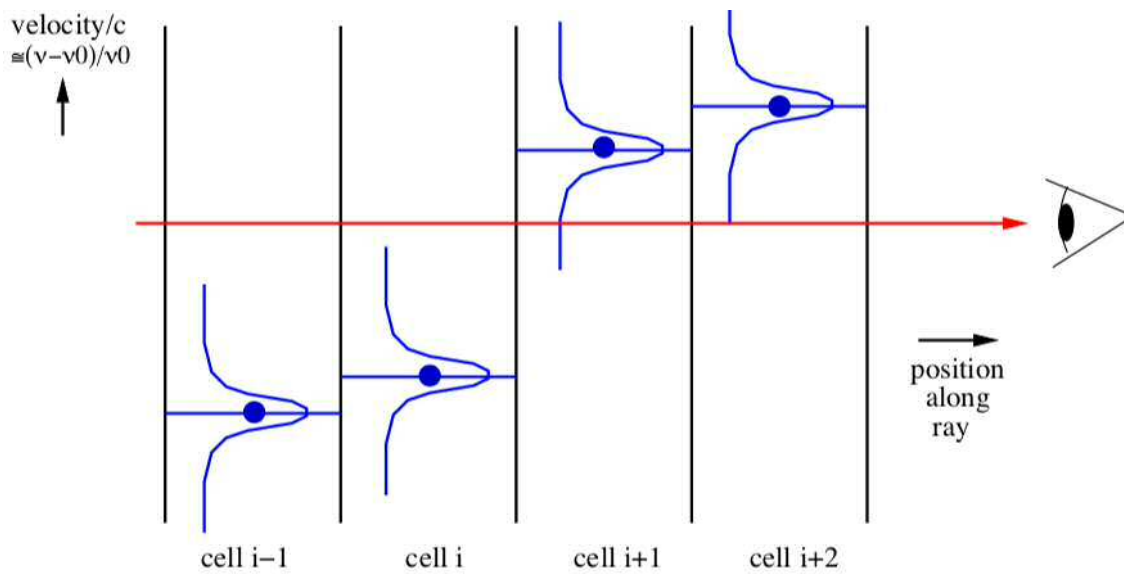


Figure 2.2. Image illustrating when a strong velocity gradient combined with a narrow linewidth profile results in a ray being unchanged by the medium.

a ray at a given frequency ν . Now due to the turbulent nature of our system two adjacent cells can have a strong velocity gradient between them that would lead to the line being heavily doppler shifted. If the intrinsic broadening of the line is very narrow, then a large shift in frequency would leave the ray unaffected as it propagates through the cell. Figure 2.2 shows such a scenario.

A simple brute force solution to this problem would be sample a larger frequency space where you have n number of rays that cover a range $\delta\nu$ and then average their contributions. However, this does not solve the issue given that for small n and very narrow profiles cells could still be under sampled. Increasing the value of n does potentially solve the problem though without any guarantee and at a very high computational cost.

The nature of the problem is the drastic velocity changes that arise due to the discrete nature of our integration from cell to cell. A more efficient solution relies on smoothing down these discontinuity-like velocity changes. To do so these changes need to first need to be identified at which point the method will automatically add sub-steps in the integration of equation 2.11 in order to guarantee that ray "sees" the cell. How many substeps are included is usually a free parameter but is normally taken to be the same as the assumed thermal broadening. This method is implemented within RADMC-3D and described in (Pontoppidan et al., 2009).

Recursive sub-pixeling

Unstructured grids can present an issue when doing ray tracing. This is specially the case when considering that the final synthetic image usually $n \times n$ pixels making the mapping the unstructured grid onto it not straightforward. Furthermore, the pixel resolution will not always match the cell resolution. Normally with 3-D Cartesian unstructured grids each cell is split into 8 new cells each half the length from the previous cell. There is, in principle, no limit to the amount of times a cell can be split further down.

The way to solve this relies on identifying any cell that is smaller than the pixel size. If this is the case then the ray passing through the center of the cell will be split into 4 equal rays each passing through the center of each of the smaller cells. This process will be repeated until each cell has one ray passing through its center. Afterwards all the intensities for each of the cells are calculated and averaged out depending on the cells size. This finally leads to all cells smaller than the pixel size effectively contributing to the pixel's intensity.

CHAPTER 3

NUMERICAL METHODS ^{*}

3.1 ACHIEVING CONVERGENCE

As we shall see in the following Chapters, to carry out radiative transfer simulations with RADMC-3D requires us to map the unstructured SPH particle distribution to a Cartesian grid. Interpolation onto a uniform grid is relatively straightforward, but such grids are not a good match for the highly non-uniform distribution of the SPH particles, with the result that high resolution is required to achieve convergence even for the CO 1-0 line (Glover et al., 2015; Szűcs, Glover & Klessen, 2016). Achieving convergence for the higher J transitions is even more difficult, owing to their higher critical densities, and requires an unfeasibly large uniform grid. To avoid this problem, we have implemented a module within RADMC-3D that allows snapshots from GADGET-2 to be readily interpolated onto a hierarchically-structured oct-tree grid. In the remainder of this section, we discuss how we construct this grid and carry out the interpolation onto it.

GRID CONSTRUCTION

We construct our grid iteratively, using a method similar to that used in adaptive mesh refinement (AMR) simulations of hydrodynamical flows. We begin with a uniform Cartesian base grid with a specified resolution. We then loop over the full set of SPH particles. For each SPH particle, we first identify the cell in our grid that contains the particle, and next apply a refinement criterion to determine whether or not the grid cell needs to be refined in order to properly represent the particle. If

^{*}The work presented in this Chapter is published in the Appendices of Peñaloza et al. (2017) and Peñaloza et al. (2018)

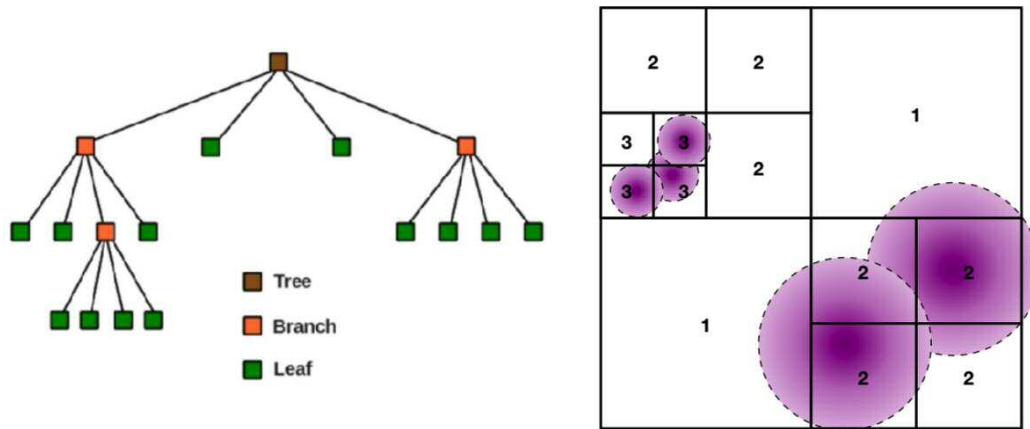


Figure 3.1. Left: A schematic diagram representing how the nested structure of the tree where brown represents the base grid or tree, orange the branches i.e. no interacting cells and green the leaves, cells where physical properties will be interpolated. The diagram structure is meant to reflect the structure of the cell depicted on the right. Right: a single cell from the base grid with an overlapped distribution of SPH particles. The refinement of each cell is done according to the distribution of cells. Note that this is a 2-D schematic, however the refinement algorithm does this in 3-D.

the cell needs to be refined, we split it into 8 sub-cells, each occupying $1/8^{\text{th}}$ of the volume of the parent cell. This process is then repeated for the same particle, using the refined grid, until the cell in which the particle is located satisfies the refinement criterion.

To determine whether or not a given cell needs to be refined, we compare a measure of its size, d , with the smoothing length of the particle, h . We define d using the equation

$$d = \sqrt{(\Delta x)^2 + (\Delta y)^2 + (\Delta z)^2}, \quad (3.1)$$

where Δx , Δy , Δz are the lengths of the side of the cell in the x , y , and z directions, respectively. Note that for a cubical base grid with the same initial resolution in each dimension, $\Delta x = \Delta y = \Delta z$ and this simplifies to $d = \sqrt{3}\Delta x$. We have examined a number of different refinement criteria and we find that the one which gives us the required resolution with the least computational overhead is the requirement that $d \leq h/2$. Figure 3.1 shows schematic diagram of a refined cell.

Once the grid satisfies the refinement criterion for the considered SPH particle, we then proceed to the next particle in the list and apply the same procedure. We continue in this way until we have looped over the full set of SPH particles. The structure of the resulting grid closely resembles the structure of the SPH particle distribution, as illustrated in Fig. 3.2. Finally, at the end of the refinement procedure,

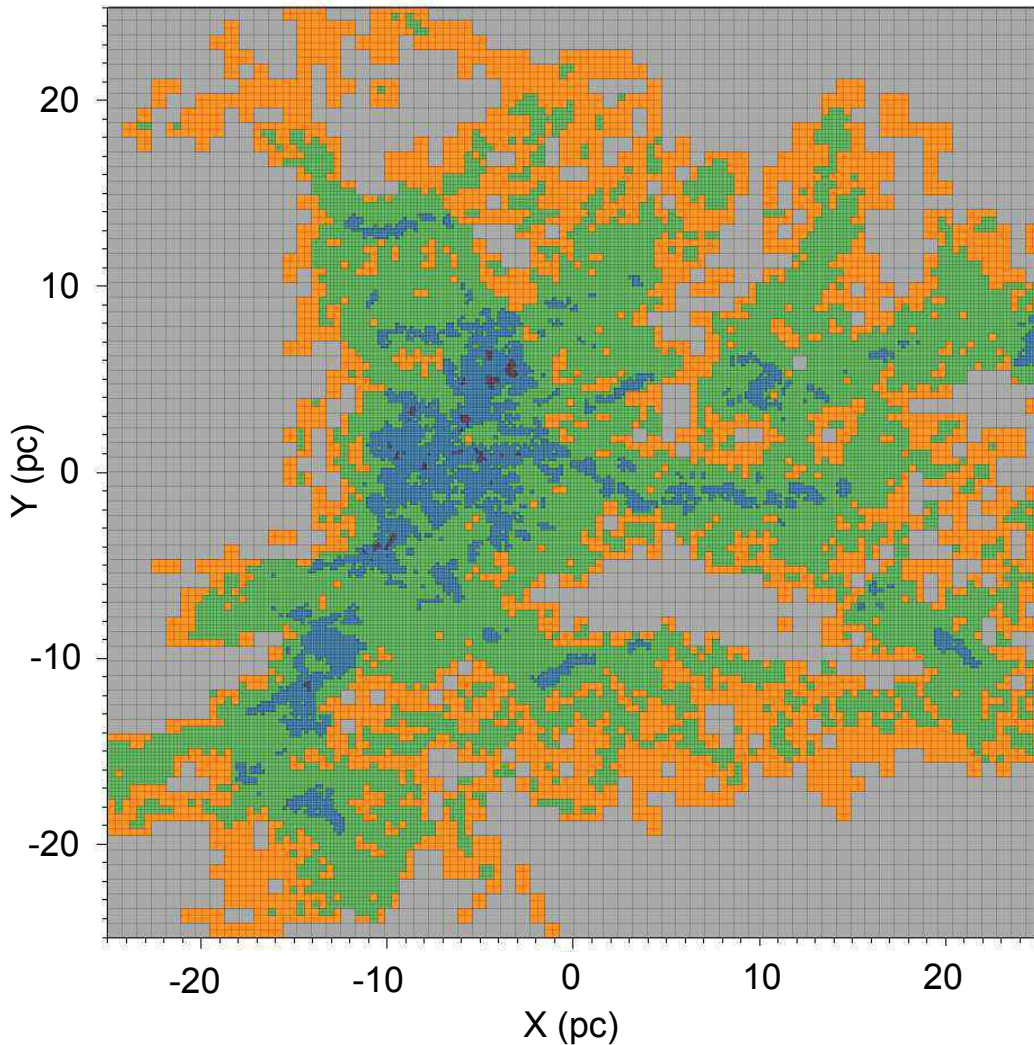


Figure 3.2. A slice through the unstructured AMR grid created with our refinement algorithm. Each colour corresponds to a different, more refined layer of the grid

we loop one further time over all particles, verifying that each particle is associated with a grid cell, and carrying out the interpolation from the particles to the grid, as described below.

When constructing the emission maps analysed in this thesis, we have used a base grid of 64^3 cells. After refinement, using the refinement criterion $d \leq h/2$, we find that the mostly highly-refined cells have been refined a total of six times, resulting in a local resolution equivalent to what one would achieve using a 4096^3 uniform grid. However, the total number of grid cells in the refined grid is only $\sim 145^3$. Our refinement procedure therefore allows us to reduce the memory requirements and computational cost by a factor of more than 2×10^4 .

INTERPOLATION

We use standard SPH kernel interpolation to interpolate the CO and H₂ number densities, the gas temperature etc. from our particle distribution onto the oct-tree grid. Briefly, if we have some scalar quantity A that is a function of position, then its value at position \mathbf{r} is given by the sum (Price, 2012):

$$A(\mathbf{r}) \simeq \sum_{b=1}^{N_n} m_b \frac{A_b}{\rho_b} W(\mathbf{r} - \mathbf{r}_b, h_b), \quad (3.2)$$

where m_b is the mass of SPH particle b , ρ_b and A_b are the values of the density and the scalar A carried by particle b , \mathbf{r}_b is that particle's position, W is the SPH smoothing kernel, h_b is the smoothing length of particle b , and we sum over all N_n particles for which $W > 0$. GADGET-2 uses a cubic spline kernel with

$$W(r, h) = \frac{8}{\pi h^3} \times \begin{cases} 1 - 6\left(\frac{r}{h}\right)^2 + 6\left(\frac{r}{h}\right)^3 & \text{if } 0 \leq \frac{r}{h} \leq 0.5 \\ 2\left(1 - \frac{r}{h}\right)^3 & \text{if } 0.5 \leq \frac{r}{h} \leq 1 \\ 0 & \text{if } \frac{r}{h} > 1, \end{cases} \quad (3.3)$$

and so for any given cell within the oct-tree grid, the only particles which contribute are those for which the smoothing length of the particle is larger than the distance from the particle to the centre of the cell. The refinement procedure described above ensures that for each SPH particle, there is at least one cell for which $r < h$, and so none of the information from the particles is lost. Note that part of the coding and testing required for creating this refinement routine was done prior to the work carried out for this thesis

ABUNDANCE CONSERVATION

As it can be seen in Figure 3.2 the interpolation and refinement scheme described above does a very good job when mapping the particles. Nonetheless, one has to be careful when performing the interpolation since the distinct nature between particles and cells can lead to numerical artefacts.

Figure 3.3 shows the abundance of CO for each cell or particle plotted against the x-axis. It can be seen that as the refinement criteria is increased i.e higher resolution then the higher the CO abundance. This is clearly a numerical artefact and specially problematic considering that it can directly effect the total emission. To fix this we use the fact that the total amount of carbon within the simulation is

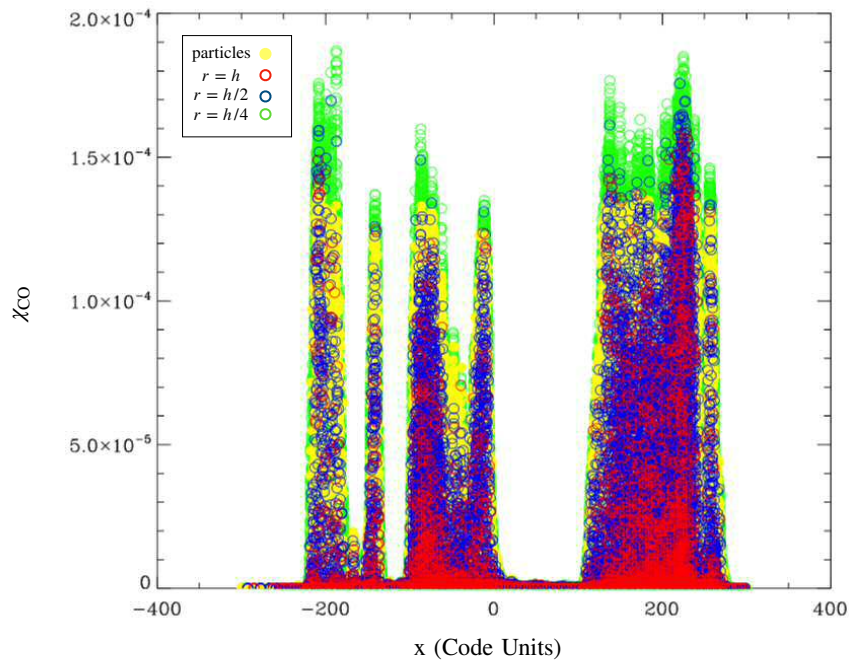


Figure 3.3. Checking interpolation

constant. Therefore after the interpolation has been done we rescale the abundance of carbon and other chemical species in order to correct for this.

REACHING CONVERGENCE

To test that our simulations are converged we ran a new set of simulations in which the only parameter varied was resolution. These results are plotted in Figs. 3.4 and 3.5.

Fig. 3.4 shows the cumulative CO emission in PPV space plotted against brightness temperature T_B . This is done for CO 1-0 and CO 2-1 for every resolution tested. Fig. 3.5 shows a similar plot for the cumulative CO emission in the integrated intensity map. A fixed resolution of 256^3 and an AMR grid with refinement criterion of $r = h$ do not reach convergence since the emission from low intensity regions is underestimated. On the other hand the cumulative emission curves for a fixed resolution of 512^3 and refinement criteria above $r = h/2$ are quite similar, which suggests that these are converged.

In this case a 512^3 resolution seems to be enough to resolve most of the particles in from the SPH snapshot and therefore provide convergence. However it is worth pointing out that this is only the case due to the nature of the studied cloud, i.e.

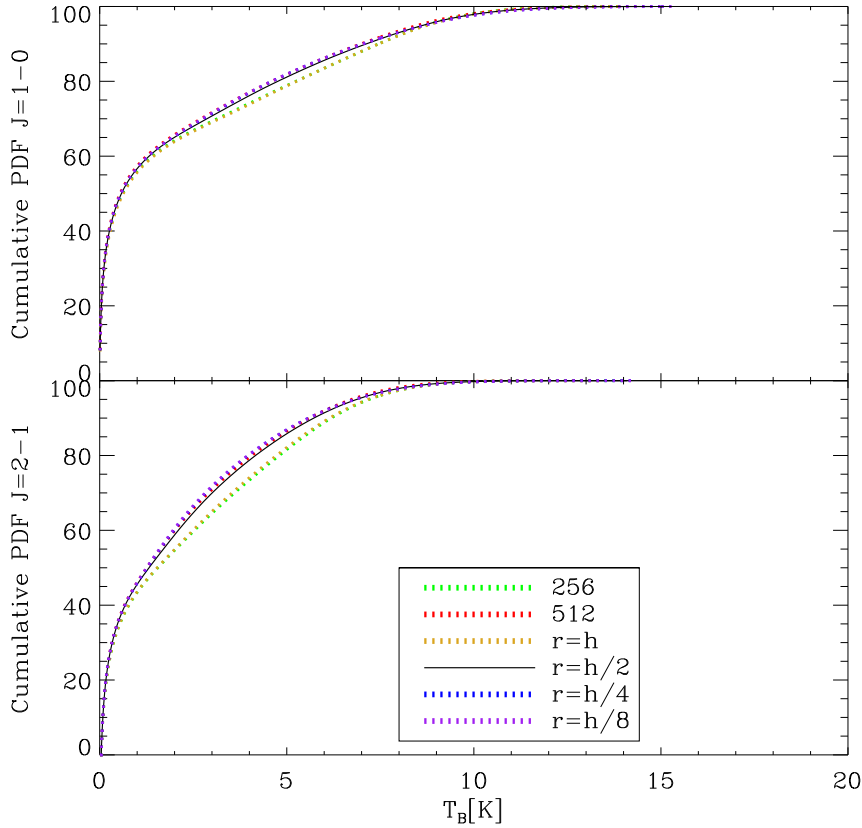


Figure 3.4. The cumulative luminosity from the PPV cube plotted against the brightness temperature of CO 1-0 (top panel) and CO 2-1 (bottom panel). The black solid line represents the resolution used for this study. The other lines correspond to different grid resolutions: the green dotted and red dotted lines correspond to fixed grids with resolutions of 256^3 and 512^3 respectively, while the remaining three lines correspond to different choices for the refinement criterion in the adaptive approach.

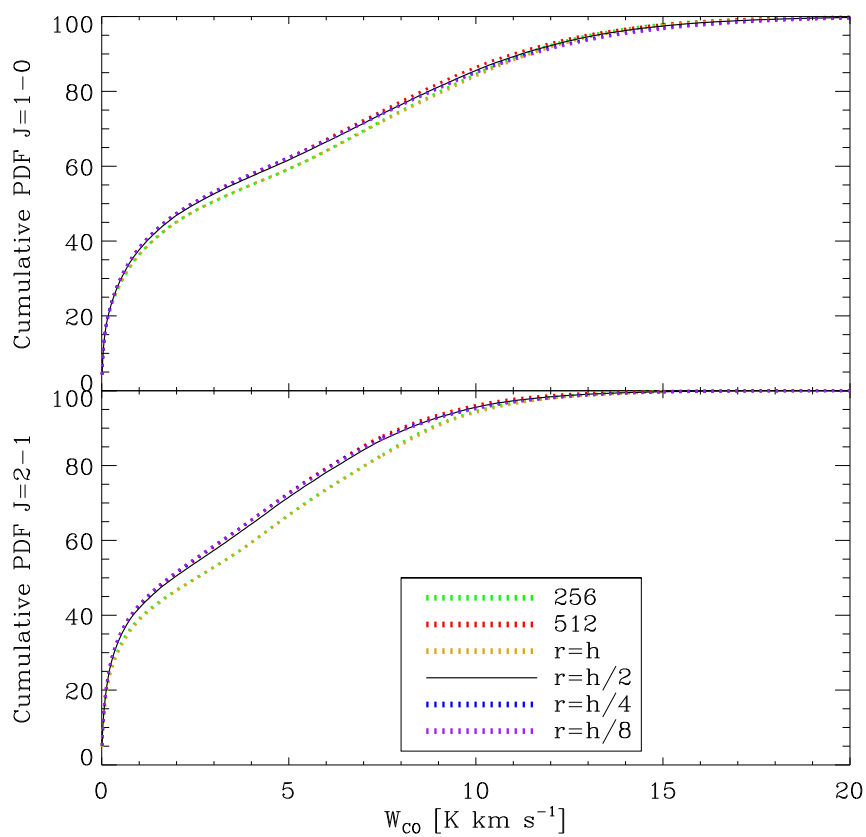


Figure 3.5. Similar plot to Fig. 3.4, however in this case the cumulative luminosity of the integrated intensity map is plotted against integrated intensity.

a small, low density cloud. Nonetheless at a fourth of the computational cost, our AMR refinement method with a refinement criterion of $r = h/2$ proves to be better.

3.2 SOBOLEV-GNEDIN APPROXIMATION

Recall in the in Section 2.2 the LVG method was explained, however, LVG has its limitations. Consider a scenario in which $|\nabla\vec{v}|$ is large but the change in density i.e. the density gradient ($|\nabla\rho|$) is small. According to equation 2.22 τ would be small and therefore the probability of a photon escaping would be high. However given that $|\nabla\rho|$ is small the escape probability of the photon should be lower, yet equation 2.22 does not consider $|\nabla\rho|$ and therefore the escape probability is unchanged. For the GMCs considered in this study we can foresee different cloud regions where such scenario is likely.

GNEDIN LENGTH

The Sobolev approximation is a local approximation given a certain length scale, where the length scale is calculated from the velocity gradient. Commonly this is called the Sobolev length and is defined by:

$$L_{Sob} = \frac{v_{th}}{|\nabla\vec{v}|} \quad (3.4)$$

where v_{th} is the thermal velocity. From this and equation 2.22 one can reconstruct a more general solution for the opacity where L need not be L_{sob} but any other length scale relevant to the problem at hand. One such length scale is the one presented by Gnedin, Tassis & Kravtsov (2009) where they define a length scale base on density gradients in order to determine column densities of H_2 . They define this length scale as

$$L_{Gn} = \frac{n_{H_2}}{|\nabla n_{H_2}|} \quad (3.5)$$

where n_{H_2} is the number density of H_2 , however for our purposes we may define this in terms of the number density of the molecule that is being modelled. With this in mind we can rewrite equation 2.22, to calculate an optical depth (τ_ρ) given a density gradient by

$$\tau_\rho = \frac{hc}{4\pi\sqrt{\pi}v_{th}} \frac{n^2}{|\nabla n|} \left(f_j \frac{g_i}{g_j} - f_i \right), \quad (3.6)$$

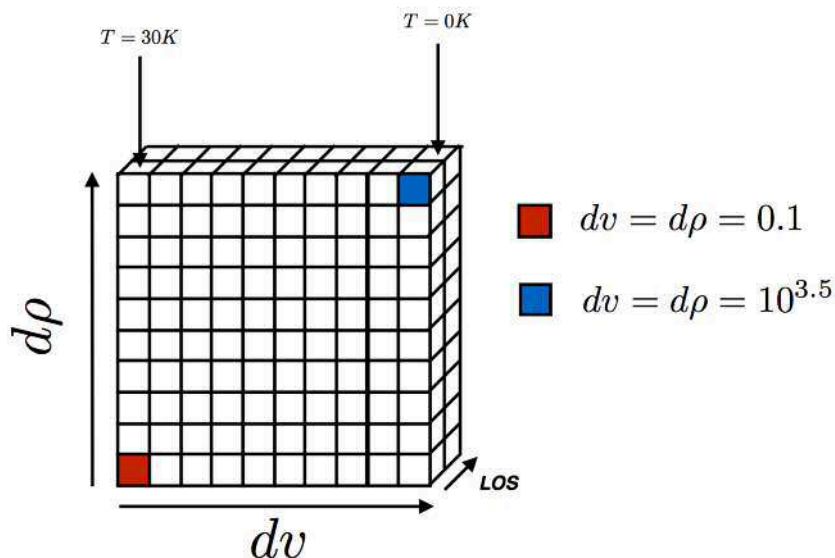


Figure 3.6. The setup of the grid used as an input for the radiative transfer. All the cells in the the front slice have the same density, temperature and velocity. The back slice has a temperature of 0 K. Densities and velocities take a value according to dv or $d\rho$, which are increased such that $dv = d\rho$ over the diagonal. dv is increase accordingly over the x -axis and $d\rho$ over the y -axis.

that has the same form as equation 2.22. At the same time equation 3.6 would fail to accurately calculate the escape probability given that τ_ρ does not consider the gradient in velocity, specially in highly turbulent systems such as GMCs.

At this point we have two adequate yet limited ways of calculating an optical depth. To obtain the best from each we follow the approach taken by Hartwig et al. (2015), where they take the harmonic mean between τ_v and τ_ρ , as follows

$$\tau = \frac{\tau_v \tau_\rho}{\tau_v + \tau_\rho}. \quad (3.7)$$

The resulting optical depth will then be used in equation 2.21 to calculate the escape probability.

IMPLEMENTATION AND TESTING

We have used the underlying framework of RADMC-3D and implemented the Gnedin approximation, as described above, as an improvement to the already present Sobolev approximation. In order to test this method we set up a test scenario that highlights the difference between LTE, LVG and LVG+ (Sobolev-Gnedin approximation).

We set up an input grid of 10 by 10 by 2, Figure 3.6 shows the position-position-position (PPP) cube that was used as an input into RADMC-3D. All the cells in the front slice have the same physical properties and will therefore have the same intrinsic emission in a scenario where $|\nabla\vec{v}|$ or $|\nabla\vec{\rho}|$ are not considered. The back slice serves to calculate the velocity and density gradients used to obtain the optical depth of each cell in the front slice. To keep the setup simple, we increase $|\nabla\vec{v}|$ only in the x -axis while keeping $|\nabla\vec{\rho}|$ constant. Conversely we increase $|\nabla\vec{\rho}|$ while keeping $|\nabla\vec{v}|$ constant on the y -axis. The increase in the gradient is taken with respect to the values of density and velocity in the front slice. These are such that $dv = d\rho$ will be the same whenever $x = y$. Additionally to avoid confusion we set the temperature of each cell in the back slice to be $T = 0$ K so that these cells have no emission.

Given the focus on CO in this thesis, we perform the radiative transfer for CO $J = 1 - 0$ but in principle the method works for any other molecule or line. Additionally we create 3 different cubes for 3 different densities of the front slice ($n = 50 \text{ cm}^{-3}, n = 100 \text{ cm}^{-3}$ and $n = 500 \text{ cm}^{-3}$). We run 3 radiative transfer simulations for each cube, each of these uses either LTE, LVG or LVG+. The resulting integrated intensities for each run for each cube are shown in Figure 3.7.

As expected changing the method for calculating the population levels makes a big difference in the final image. Since the density and temperature of each cell are the exactly the same assuming LTE results in the integrated intensity for each cell also being the same. This is because LTE uses no information of the gradient surrounding the cell to calculate the level populations. For the LVG scenario we can definitely see a change in intensity over the x -axis, which corresponds to an increase in $|\nabla\vec{v}|$. However not taking $|\nabla\vec{\rho}|$ into account results in the intensity being exactly the same on the y -axis. Finally when using the LVG+ method both changes on $|\nabla\vec{v}|$ and $|\nabla\vec{\rho}|$ are reflected on the final intensity of each cell.

One important note to keep in mind when looking at these results is why increasing the gradient results in an increase in intensity rather than a decrease. The reason is that the background radiation and the high temperature of the cell causes higher levels to be radiatively pumped. These will then quickly cascade down to the ground state i.e $J = 1 - 0$ causing it to be much brighter. The reason behind this is that for lower temperatures the difference between cells very small and hard to see. This should not be a problem since our interest is to test that the method works. In the next section we will show how using LVG+ changes the integrated intensities of one of our clouds.

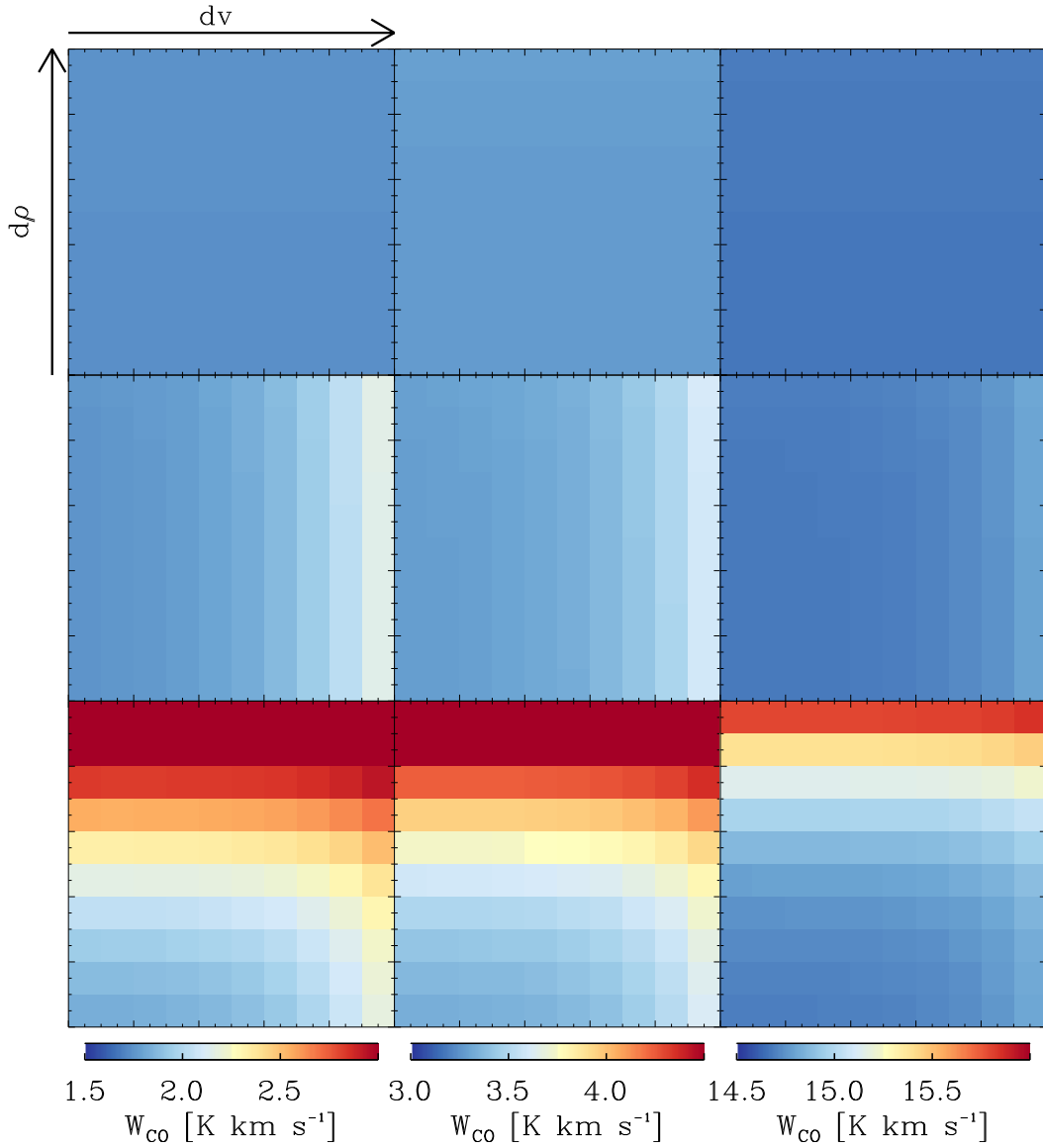


Figure 3.7. The integrated intensities of CO $J = 1 - 0$ for each run on each cube. Each row has a different method for calculating level populations: top = LTE, middle = LVG, bottom = LVG+. Similarly each column has a different number density for the front slice, left: $n = 50 \text{ cm}^{-3}$, middle: $n = 100 \text{ cm}^{-3}$, right: $n = 500 \text{ cm}^{-3}$. Note that even though the colours are similar the colourbar for each column is different

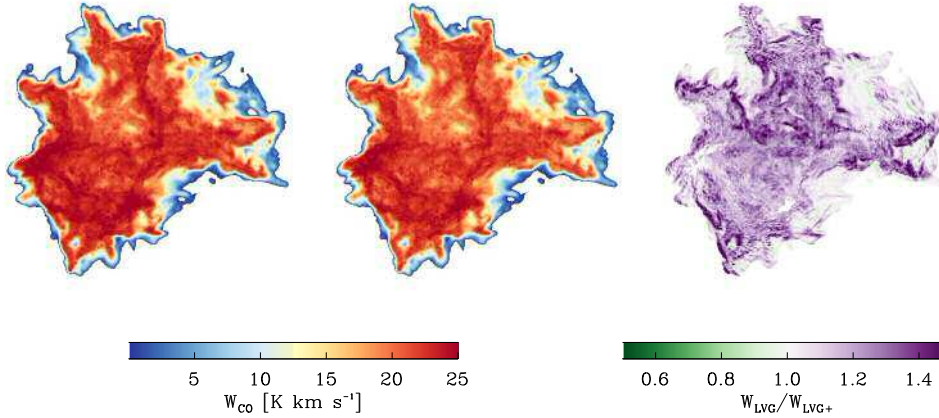


Figure 3.8. The image on the left shows the integrated intensity for CG15-M4-G1 with an LVG treatment while the middle image does so for LVG+. The image on the right is the ratio of LVG/LVG+ integrated intensities

RESULT COMPARISON

Even though we tested that LVG+ works, it is important to check whether this new method has any significant effect on a more realistic system such as our numerically simulated clouds. To check this we performed two radiative transfer simulations on CG15-M4-G1, one using LVG and another using LVG+. The integrated intensities of these two runs are shown in Figure 3.8.

At first glance it seems that the difference between LVG and LVG+ is negligible. However when taking the ratio between the both we can see that the brightness of the cloud definitely changes when using LVG+. For most regions of the cloud the brightness is reduced, nonetheless there are still regions that can either become brighter or remain the same. It then follows that considering changes in the local density does play an important role when calculating the level populations and total emission of a system. This illustrates how small changes in the physical conditions of the gas and the interplay with the surrounding environment can lead to changes in the total emission.

CHAPTER 4

USING CO LINE RATIOS TO TRACE THE PHYSICAL PROPERTIES OF MOLECULAR CLOUDS *

4.1 INTRODUCTION

The characterisation of giant molecular clouds (GMCs) – the sites of nearly all star formation activity in the local Universe – is an important step towards understanding how stars are born. Molecular hydrogen (H_2) is the most abundant molecule in the interstellar medium (ISM), but its rotational emission lines are not excitable at the temperatures found in most GMCs. However, the second most abundant molecule is carbon monoxide (CO), which has rotational transitions that are easily excitable within typical GMCs, making CO a good tracer of molecular gas. Additionally the lower levels of CO emit at a frequency that can be observed from the ground. Therefore, CO has become the favoured tracer for studying molecular gas in GMCs (Liszt & Lucas, 1998; Dame, Hartmann & Thaddeus, 2001; McKee & Ostriker, 2007; Goldsmith et al., 2008; Bolatto, Wolfire & Leroy, 2013; Klessen & Glover, 2016).

CO is not without problems as a tracer of molecular gas. Its emission is highly sensitive to environmental conditions (Liszt & Pety, 2012), and traces only a limited range of column densities. At low column densities, CO is rapidly photodissociated by the interstellar radiation field (ISRF) (van Dishoeck & Black, 1988), while at high column densities, its emission lines become optically thick. For the $J = 1 - 0$ line of ^{12}CO , this occurs at a CO column density of $N_{\text{CO}} \approx 10^{16} \text{cm}^{-2}$, corresponding to a visual extinction of only a few (Liszt & Lucas, 1998). Observations of this line

*The work presented in this Chapter is based on the published work in Peñaloza et al. (2017)

therefore do not directly probe the highest density regions of the cloud.

Despite this, CO emission still contains plenty of information about the cloud's conditions and structure. A study by Castets et al. (1990) illustrates this by investigating the emission ratio ($R_{2-1/1-0}$) for CO's lowest two rotation transitions, $J = 2-1$ and $J = 1-0$. This ratio is conventionally defined as

$$R_{2-1/1-0} = \frac{W_{2-1}}{W_{1-0}}, \quad (4.1)$$

where W_{1-0} and W_{2-1} are the velocity-integrated brightness temperatures of the $J = 1-0$ and $J = 2-1$ rotational transition lines of CO, expressed in units of K km s^{-1} . These two transitions have energy separations $E_{10}/k_B = 5.5 \text{ K}$ and $E_{21}/k_B = 11.04 \text{ K}$, respectively, where k_B is Boltzmann's constant. Their critical densities in fully molecular gas with a temperature $T = 10 \text{ K}$ are $n_{\text{crit},1-0} \simeq 2000 \text{ cm}^{-3}$ and $n_{\text{crit},2-1} \simeq 10000 \text{ cm}^{-3}$. As most of the gas in a molecular cloud has a density $n_{\text{H}_2} < n_{\text{crit},2-1}$, the value of $R_{2-1/1-0}$ is sensitive to both the density and the temperature structure of the gas, as well as the optical depth of the two lines.

The behaviour of $R_{2-1/1-0}$ on small scales within molecular clouds has been examined by Sakamoto et al. (1994) and more recently by Nishimura et al. (2015). They studied how the line ratio varies within the Orion GMC, finding that $R_{2-1/1-0} \sim 1$ towards the centre of the cloud, but that it declines towards the outskirts where $R_{2-1/1-0} \sim 0.5$. Sakamoto et al. (1994) argue that the observed variations can be understood as a consequence of the density variations within the cloud. This is a reasonable assumption if the CO-emitting gas is isothermal, but we know from numerical simulations of molecular clouds that this is only approximately true and that temperature variations of a factor of two or more within CO-rich gas are not uncommon (see e.g. Glover et al., 2010). Further complicating matters is the fact that the variations in density and temperature are not independent: the density structure depends sensitively on the temperature of the gas, while the temperature depends both on the density, and also on other factors such as the local extinction, the metallicity of the gas and the strength of the ISRF.

In order to better understand what the CO line ratio can tell us about the physics of the cloud, we make use of numerical models which satisfactorily reproduce the irregular structure of the gas. This has become practical within the last few years with the advent of 3D dynamical models of GMCs that account for the chemical and thermal evolution of the gas, the non-isotropic nature of the attenuated radiation field, and the complex morphology of the cloud whilst still being computationally reasonable (see e.g. Glover et al. 2010, Clark, Glover & Klessen 2012a, Bisbas et al.

2012, Offner et al. 2013).

We make use of these techniques to study the behaviour of $R_{2-1/1-0}$ within a turbulent molecular cloud. We perform a 3D hydrodynamical simulation of a representative cloud that self-consistently follow the thermal and chemical evolution of the gas. We then post-process the results of this simulation to generate synthetic ^{12}CO 1-0 and 2-1 emission maps.[†] The resulting maps allow us to study in detail the relationship between the line ratio and the physical conditions in the cloud.

The structure of this Chapter is as follows. In Section 4.2, we outline our method for modelling a molecular cloud and also describe how we post-process the simulations to generate synthetic emission maps. Section 4.3 presents the results from our simulations and the analysis of the emission lines and $R_{2-1/1-0}$. Section 4.4 discusses possible explanations for the physical processes driving the behaviour $R_{2-1/1-0}$ and how this is consistent with our findings. Finally we summarise all of our findings in Section 4.5.

4.2 METHOD

4.2.1 NUMERICAL SETUP

Initial conditions

Our initial setup uses a $10^4 M_\odot$ uniform sphere ($R \sim 8.84$ pc), with an initial volume density of $n = 100 \text{cm}^{-3}$ (n is given for a mean molecular weight of $\mu = 1.4$) and 2×10^6 SPH particles. We impose a turbulent velocity field with a power spectrum of $P(k) \propto k^{-4}$, in which the energy is partitioned into a natural mixture of solenoidal and compressive modes. The energy in the turbulent velocity field is set such that $E_{\text{pot}}/E_{\text{kin}} = \epsilon = 2$ (i.e. the cloud is gravitationally bound). This kinetic energy is allowed to decay freely via shock dissipation.

We adopt solar metallicity ($Z = Z_\odot$), and a standard dust-to-gas ratio of 0.01. For the ISRF, we use a spectral shape taken from Draine (1978) at ultraviolet wavelengths and Black (1994) at longer wavelengths. The strength of the ISRF is scaled such that $G_0 = 1.7$ in Habing (1968) units, where G_0 is the energy density in the range 6–13.6 eV. At the beginning of the simulation, hydrogen is assumed to be fully molecular, i.e. $f(\text{H}_2) = 1$, oxygen is in its atomic form, and carbon is assumed to be in the form of C^+ .

Clark et al. (2012b) demonstrated that the H_2 fraction rises sharply to near unity in the compression events that form molecular clouds. However, it has also

[†]From this point on, when we refer to CO, we mean ^{12}CO , unless otherwise noted.

been shown that the initial chemical state of the cloud has little effect on the global evolution (Glover & Clark, 2012a,b; Clark & Glover, 2015). In this study, we analysed our results for clouds which started both fully atomic and fully molecular, finding no significant difference. In the interest of clarity, we present only the results from the clouds with $f(\text{H}_2) = 1$ initially.

As we are interested in the properties of the gas, and not the star formation that takes place inside the cloud, we stop the simulation just as the collapse of the first pre-stellar core occurs. This takes place at about 1.91 Myr for our simulated cloud. At this point, we produce a snapshot containing the positions, velocities, temperatures, dust densities and molecular number densities for each SPH particle. This snapshot contains the necessary data to perform radiative transfer simulations and produce synthetic emission maps.

4.2.2 POST-PROCESSING

Radiative transfer simulations

To produce synthetic observations of the CO emission, we need to post-process our final simulation snapshot with a line radiative transfer code. In this study we use the publicly available radiative transfer code RADMC-3D (Dullemond, 2012). The high optical depth of CO means that the populations in the first and second energy levels are often close to those expected for molecules in local thermal equilibrium (LTE). However, this is not always the case, in particular in gas that has a low density or low optical depth. Therefore, we use the large velocity gradient (LVG) approximation (Sobolev, 1957) to account for the non-LTE level populations in these regions. A detailed description of the implementation of the LVG algorithm in RADMC-3D can be found in Shetty et al. (2011). Note that the Sobolev-Gnedin approximation as explained in Section 3.2 was not used here since it was developed after this study was carried on.

For the level population calculations, RADMC-3D requires the number density of CO, the number density of its dominant collision partner H_2 , the temperature and the velocity of the gas, all which come directly from our hydrodynamic simulation. Additionally the molecular properties for CO are taken from the Leiden Atomic and Molecular Database (Schöier et al., 2005). The collisional excitation rates that we adopt come originally from the study of Yang et al. (2010). Finally, we include a microturbulence velocity dispersion of $v = 0.2 \text{ km s}^{-1}$ to account for small-scale broadening of the spectral lines by unresolved velocity fluctuations. The magnitude of this microturbulent velocity is chosen to be consistent with the Larson (1981)

size-linewidth relation.

Grid interpolation

To post-process the SPH data in RADMC-3D, one first needs to map the unstructured SPH particle distribution onto a Cartesian grid. Interpolation onto a uniform cartesian grid (see e.g. Glover & Clark 2012c and Szűcs, Glover & Klessen 2014) is straightforward, but has the limitation that it is not well suited to account for the varying spatial resolution that exists in GADGET-2's particle distribution. In high density regions, the Lagrangian nature of SPH means that the particles are closely spaced, but this information can be lost if they are interpolated onto a grid with a cell size that is larger than the inter-particle spacing. The obvious solution to this problem is to require the cell size to be smaller than the smallest particle separation, but to achieve this with a uniform grid is computationally infeasible and would require a grid resolution of around 4096^3 for the simulation we present here.

In our present study, we therefore make use of an alternative solution. RADMC-3D is capable of constructing and utilising oct-tree grids (similar to those used in some adaptive mesh refinement codes, such as FLASH; see e.g. Fryxell et al. 2000), and this structure is a much more natural fit to the disordered SPH particle distribution. We therefore interpolate the data from the SPH particles onto a suitably-constructed oct-tree grid, ensuring that no data is lost during the interpolation process. Full details of this methodology where explained in Section 3.1.

4.3 THE CO 2-1 / CO 1-0 LINE RATIO

4.3.1 CO EMISSION MAPS

The column density map in the upper-left panel of Fig. 4.1 gives an overview of the gas distribution and density of the cloud at the end of the simulation. The column density shown is the total column density of H nuclei, $N_{\text{gas}} = N_{\text{H}} + N_{\text{H}^+} + 2N_{\text{H}_2}$. However, as the gas is predominantly molecular, we find that in practice, $N_{\text{gas}} \simeq 2N_{\text{H}_2}$. The column density map clearly shows the filamentary structure produced in the cloud by turbulence and self-gravity.

Maps of the velocity-integrated intensity of the CO 1-0 and 2-1 emission lines, W_{10} and W_{21} , are also shown in Fig. 4.1, in the upper-right and lower-right panels, respectively. Comparing the column density map and the integrated intensities for both lines, we see that the bulk of the gas in the cloud is well-traced by the emission. Many of the filamentary structures visible in the column density map are flattened

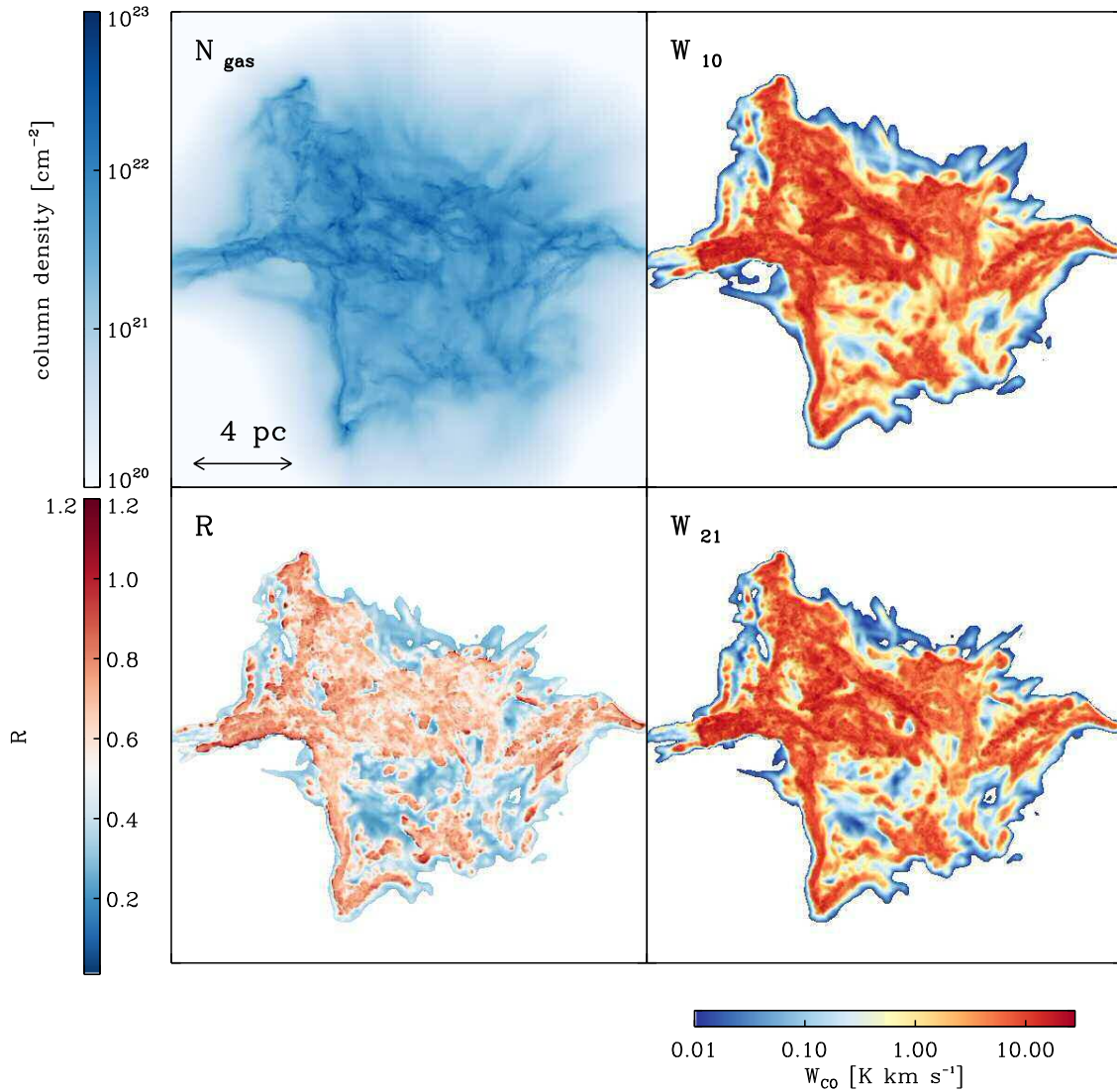


Figure 4.1. Top left: Column density of hydrogen nuclei, N_{gas} , at the end of the simulation. Since the gas in the cloud is primarily molecular, the H_2 column density is given approximately by $N_{\text{H}_2} \simeq N_{\text{gas}}/2$. Top right and bottom right: the velocity-integrated intensity of the cloud at the same time, for the $J=1-0$ and $J=2-1$ emission lines, respectively. Bottom left: the emission line ratio $R_{2-1/1-0}$, as defined in Equation 4.1.

out due to line saturation. However, their locations are still visible in the maps of W_{10} and W_{21} . Towards the denser regions of the filaments, the emission is much brighter and more structure can be observed. Note, however, that the change in the column density as we move from one of the filaments to the surrounding gas is much smaller than the corresponding change in the CO integrated intensity; much of the CO in the lower density gas is photodissociated by the ISRF.

Comparing W_{10} and W_{21} , we see that both maps show similar structure, with the most obvious difference being that in general W_{10} is slightly brighter than W_{21} . This is particularly apparent towards the centre of the filaments, or at the outskirts of the cloud, where the gas is most diffuse. Nevertheless, the overall integrated intensity of both lines is very similar.

4.3.2 THE VALUE OF $R_{2-1/1-0}$

The images in Fig. 4.1 discussed above show that the emission from both the CO 1-0 and CO 2-1 lines is very similar. In order to highlight the differences that do exist, we compute the ratio $R_{2-1/1-0}$, as defined in Equation 4.1, for each pixel in the synthetic image. The resulting distribution of intensity ratios is shown in the bottom left panel of Fig. 4.1. This figure suggests that the distribution of $R_{2-1/1-0}$ could be bimodal.

To better quantify the variations in the line ratio, we construct a probability density function (PDF) for $R_{2-1/1-0}$, which is shown in panel (i) of Fig. 4.2. This PDF is constructed using area weighting, meaning that each pixel in the synthetic images is weighted equally. The figure confirms the bimodal behaviour of $R_{2-1/1-0}$: there are two distinct peaks, one centred at $R_{2-1/1-0} \sim 0.7$ and the other at $R_{2-1/1-0} \sim 0.3$. If we consider the cumulative PDF, as shown in Panel (ii) of Fig. 4.2, then we see that the high ratio peak represents around 60% of the total cloud area, and the low ratio peak represents the remaining 40%.

Observationally, measurements of $R_{2-1/1-0}$ for real molecular clouds or collections of molecular clouds typically recover values similar to those that we find for the high ratio peak. For example, Sakamoto et al. (1994) report mean values of $R_{2-1/1-0}$ of 0.77 for the Orion A molecular cloud and 0.66 for the Orion B cloud. On larger scales, Koda et al. (2012) report values of around 0.7–0.9 for clouds in the spiral arms of M51, although for the inter-arm clouds they find somewhat lower values of 0.4–0.6. It is also worth noting that a common value adopted in the literature for converting from W_{21} to W_{10} is $R_{2-1/1-0} \sim 0.7$ (Eckart et al., 1990; Casoli et al., 1991; Brand & Wouterloot, 1995; Sakamoto et al., 1997; Hasegawa, 1997; Sawada et al., 2001; Bigiel

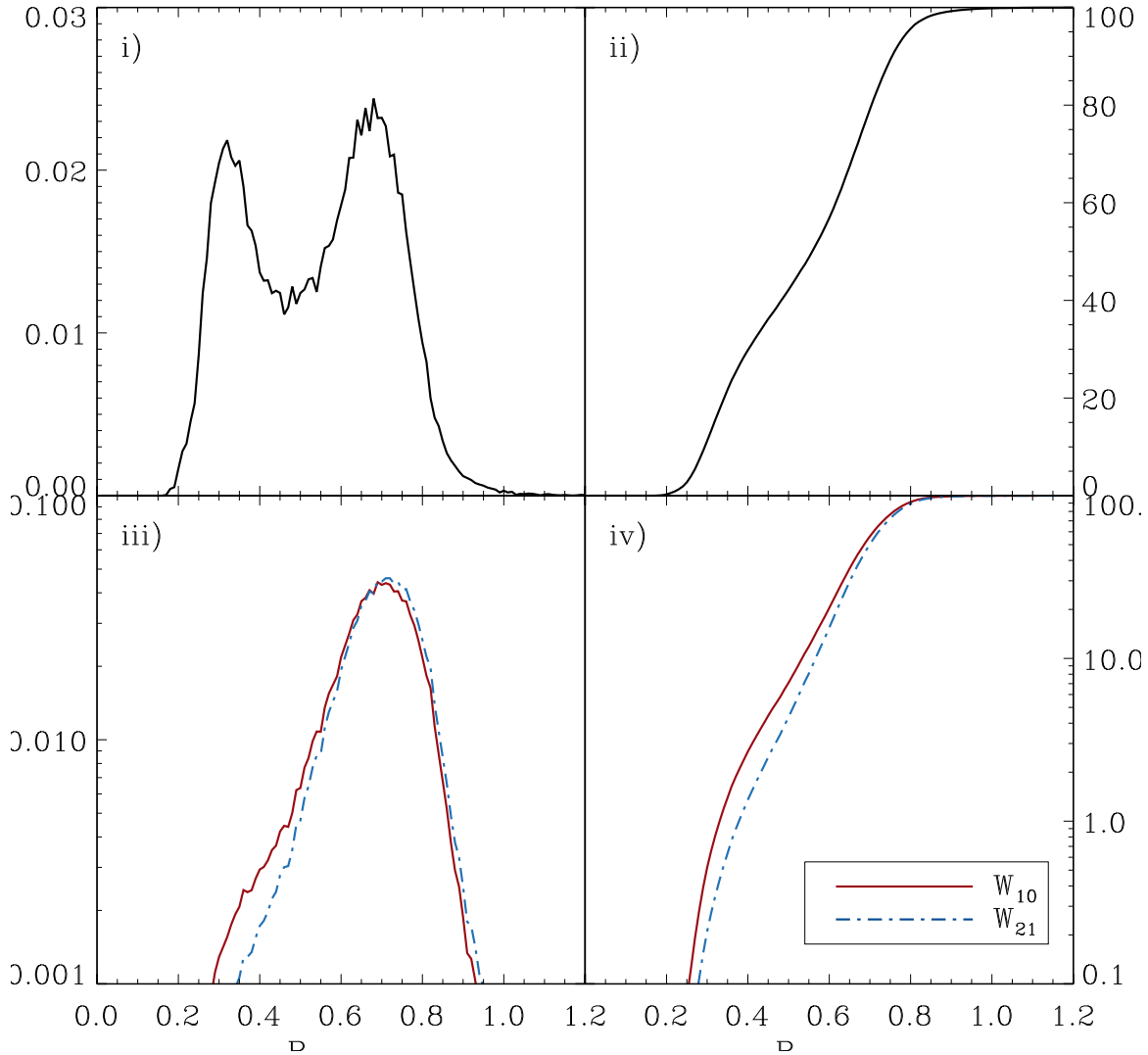


Figure 4.2. (i) Probability density function (PDF) of $R_{2-1/1-0}$, illustrating its bimodal behaviour. (ii) Cumulative PDF of $R_{2-1/1-0}$. (iii) PDF of $R_{2-1/1-0}$, weighted by the integrated brightness temperature W_{CO} of the 1-0 line (red solid) or the 2-1 line (blue dashed-dotted). (iv) Cumulative version of (iii).

et al., 2008; Leroy et al., 2009; Barriault, Joncas & Plume, 2011).

The reason why these previous studies have not detected or discussed the lower ratio peak becomes clear when we examine the emission-weighted PDF of $R_{2-1/1-0}$, shown in panel (iii) of Fig. 4.2. It is evident from this plot that although both peaks in the area-weighted PDF correspond to similar areas, they correspond to very different total intensities. The high ratio peak corresponds to regions of the cloud that are bright in CO, and hence shows up clearly in the emission-weighted PDF. The low ratio peak, however, is produced by emission from regions with very low CO brightness, and hence essentially disappears in the emission-weighted PDF, remaining visible only as a small wing on the left-hand side of the main peak. We see also that we recover the same behaviour regardless of whether we weight the PDF using the integrated intensity of the (1-0) transition (the red curve in panel (iii) of Fig. 4.2) or the (2-1) transition (the blue curve in the same Figure).

To get a feel for the sensitivity that would be required to observe $R_{2-1/1-0}$, in Fig. 4.3 we show how $R_{2-1/1-0}$ varies as a function of the integrated intensity of the 1-0 line. This plot again demonstrates that lines-of-sight with low values of $R_{2-1/1-0}$ have low integrated intensities. For example, essentially all of the lines-of-sight that have $R_{2-1/1-0} \sim 0.3$ have CO 1-0 integrated intensities that are less than 1 K km s^{-1} . Observations with sensitivities of $> 1 \text{ K km s}^{-1}$ will therefore simply not detect the emission from these regions.

To put these values into context, note that the CO (1-0) map used in the Sakamoto et al. (1994) study of Orion A and B (taken originally from Maddalena et al. 1986) has a brightness temperature sensitivity of around 0.8 K , while the CO (2-1) map made by Sakamoto et al. (1994) themselves has roughly a factor of two better sensitivity. If we assume a cloud velocity width of a few km s^{-1} , this corresponds to a minimum integrated intensity of a few K km s^{-1} for both lines. It is therefore unsurprising that they recover only high values for $R_{2-1/1-0}$. Interestingly, the more recent study of Orion A and B by Nishimura et al. (2015), which had a 3σ sensitivity of 0.24 K km s^{-1} , recovers values of $R_{2-1/1-0} \sim 0.4$ or lower in some regions of the cloud (particularly towards the left side of the ridge, away from the OB association), consistent with our argument above that high sensitivity is required in order to observe regions with low $R_{2-1/1-0}$.

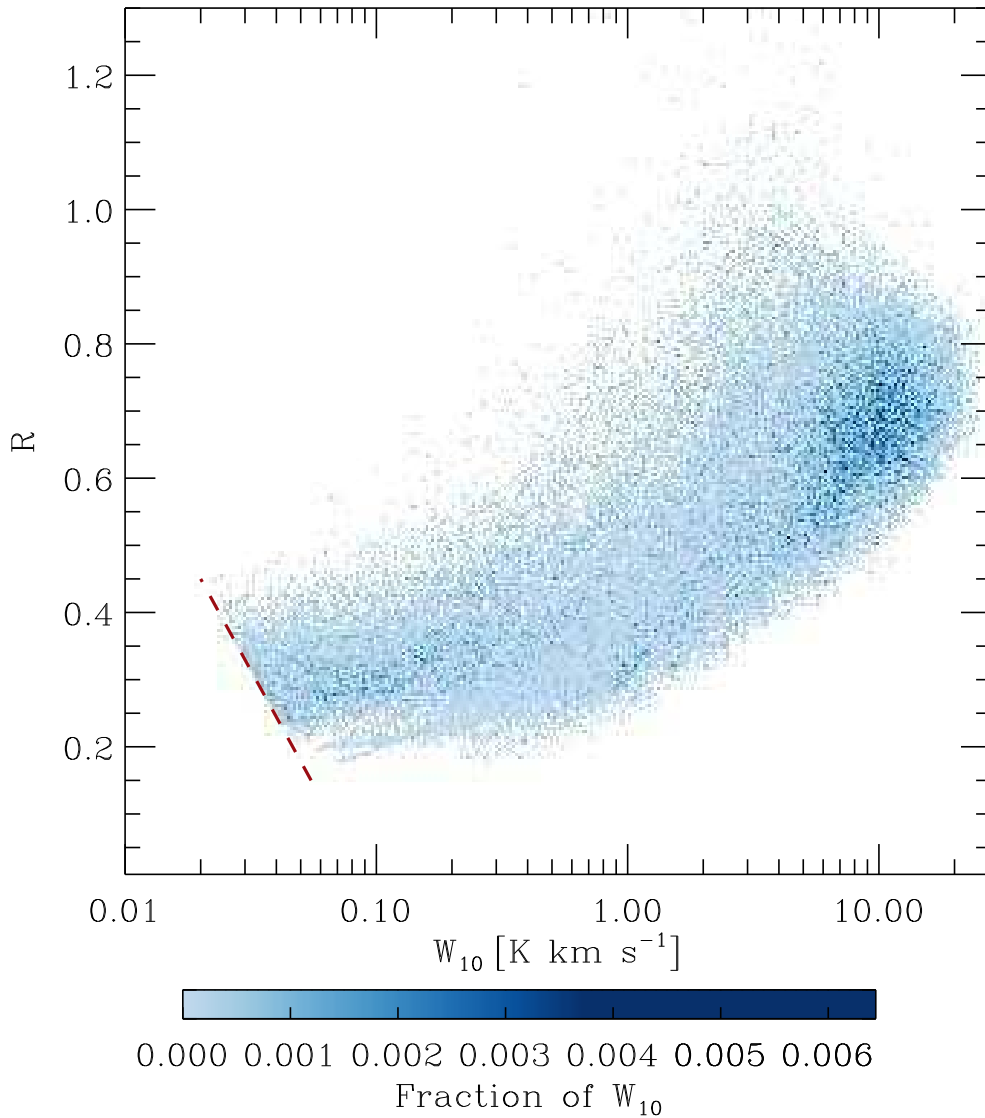


Figure 4.3. $R_{2-1/1-0}$, plotted as a function of the integrated intensity of the CO 1-0 line, W_{10} . Values are plotted for all pixels in the synthetic emission maps that have $W_{10} > 0.01 \text{ K kms}^{-1}$ and $W_{21} > 0.01 \text{ K kms}^{-1}$. The diagonal red dashed line indicate this selection criterion. Note that in practice, $R < 0.4$ when $W_{10} < 0.1 \text{ K kms}^{-1}$, so a number of points are removed that have $W_{21} < 0.01 \text{ K kms}^{-1}$ but $W_{10} > 0.01 \text{ K kms}^{-1}$.

4.3.3 THE DEPENDENCE OF $R_{2-1/1-0}$ ON DENSITY AND TEMPERATURE

Considering the distribution of $R_{2-1/1-0}$ in our maps in Fig. 4.1, it is worth exploring how it relates to physical quantities within the cloud such as temperature or density. The bimodal behaviour we see in the area-weighted PDF suggests that the local conditions of the cloud are changing such that emission from one or both lines is affected, creating two peaks in $R_{2-1/1-0}$. We investigate how $R_{2-1/1-0}$ varies as a function of a number of different quantities computed for each line of sight: the mass weighted mean temperature $\langle T \rangle = \sum_i T_i m_i$, the mean number density $\langle n \rangle$, or the H_2 and CO column densities (N_{H_2} and N_{CO}). We also examine how these quantities correlate with each other. The results are shown in Fig. 4.4. Note that the colour map used in these plots to indicate $R_{2-1/1-0}$ is the same as that of Fig. 4.1.

Panel (i) in Fig. 4.4 shows N_{CO} plotted against $\langle T \rangle$. Although there is a clear inverse correlation between these two quantities, there is also significant scatter in the mean temperature associated with any given CO column density. This is a consequence of the fact that other than at the very highest CO column densities, warm, CO-poor gas makes a significant contribution to $\langle T \rangle$ but has little influence on N_{CO} . This is not surprising since this follows from the heating and cooling processes of the gas (Field, Goldsmith & Habing, 1969; Glover & Clark, 2012a). Therefore two sight-lines that probe similar amounts of CO but differing amounts of warm gas, can have quite different mean temperatures associated with the same CO column density. Consequently, $\langle T \rangle$ is only a good measure of the temperature of the CO-emitting gas when the CO column density is large. We also see that $R_{2-1/1-0}$ has a strong dependence on N_{CO} : there is a clear rapid shift at $N_{\text{CO}} \sim 10^{15} \text{cm}^{-2}$ separating gas with low $R_{2-1/1-0}$ from gas with high $R_{2-1/1-0}$. On the other hand, $R_{2-1/1-0}$ depends only weakly on $\langle T \rangle$, largely because $\langle T \rangle$ in general is not a good measure of the temperature of the CO-emitting gas.

Panel (ii) in Fig. 4.4 depicts N_{H_2} plotted against $\langle T \rangle$. Again, there is a clear inverse correlation, reflecting the fact that lines-of-sight with high H_2 column densities preferentially sample dense gas that is well-shielded from the ISRF and that hence is cold. Looking at the behaviour of $R_{2-1/1-0}$ in this plot, we see that although it is low when N_{H_2} is small ($N_{\text{H}_2} \sim 10^{21} \text{cm}^{-2}$) and high when N_{H_2} is large ($N_{\text{H}_2} > 10^{22} \text{cm}^{-2}$), at intermediate column densities there is no clear correlation between $R_{2-1/1-0}$ and N_{H_2} .

In panel (iii) of Fig. 4.4, we illustrate the relationship between $\langle n \rangle$ and $\langle T \rangle$. In this case, there is a relatively tight inverse correlation, showing that lines-of-sight

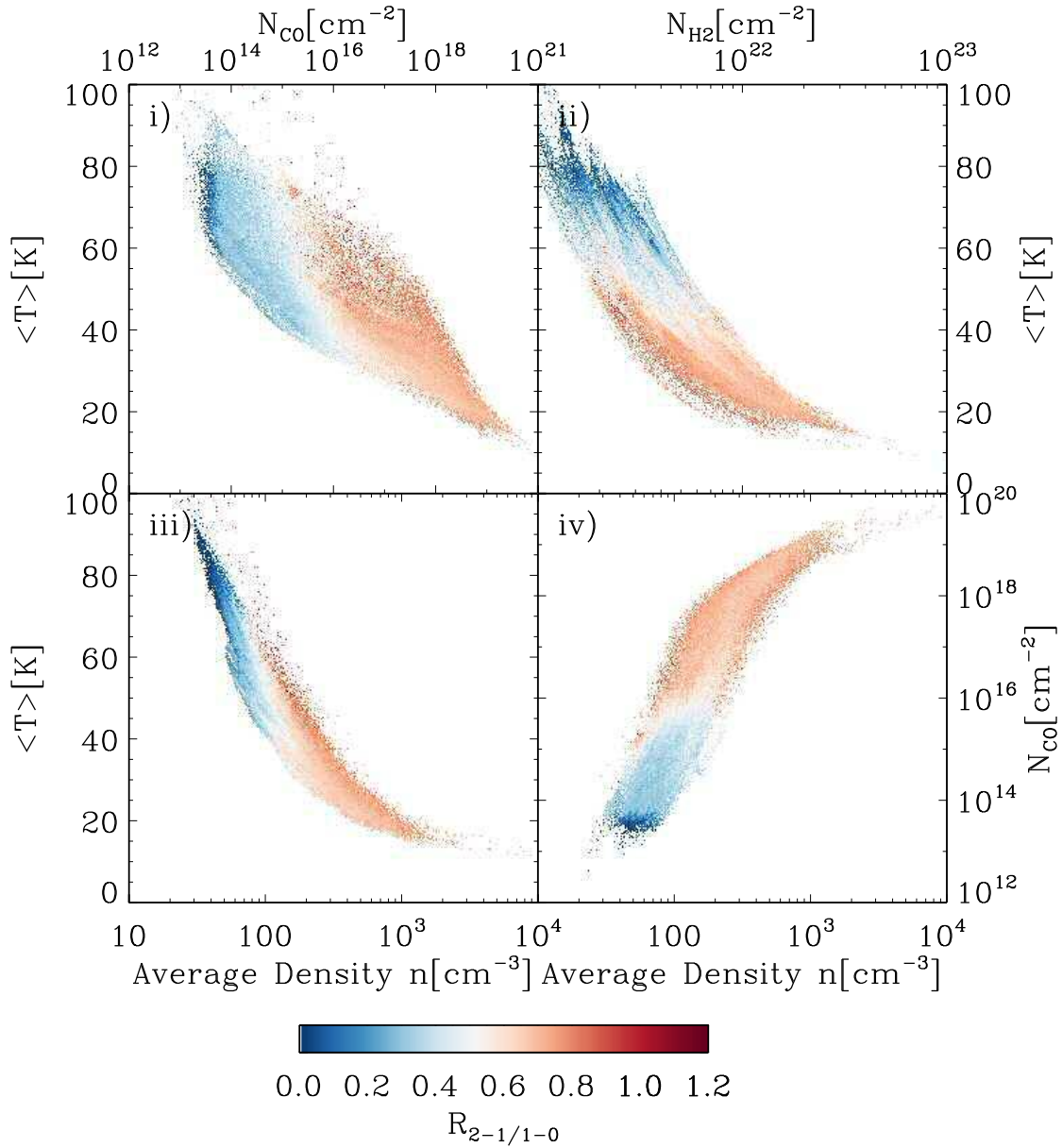


Figure 4.4. Different physical quantities are plotted and colour coded with $R_{2-1/1-0}$: (i) N_{CO} vs $\langle T \rangle$; (ii) N_{H_2} vs $\langle T \rangle$; (iii) $\langle n \rangle$ vs $\langle T \rangle$; (iv) $\langle n \rangle$ vs N_{CO} .

with low mean density probe primarily warm gas, while lines-of-sight with high mean density probe cold gas. Once again, there is a clear bimodality in the behaviour of $R_{2-1/1-0}$: low values correlate well with low mean densities and high mean temperatures, while high values correlate with high mean densities and low mean temperatures.

Finally, in panel (iv) of Fig. 4.4, we present $\langle n \rangle$ against N_{CO} . We see from this plot that although there is a clear correlation between the mean density along a sight-line and the CO column density of that sight-line, there is a substantial scatter in this relationship for values of $\langle n \rangle$ around $\langle n \rangle \sim 100 \text{ cm}^{-3}$. As $R_{2-1/1-0}$ correlates more strongly with N_{CO} than with $\langle n \rangle$, the result is that there is only a weak relationship between the mean density and the value of $R_{2-1/1-0}$ for mean densities close to 100 cm^{-3} . However, it is also clear that $R_{2-1/1-0}$ is always large when $n \gg 100 \text{ cm}^{-3}$, and always small if $n \ll 100 \text{ cm}^{-3}$.

Putting this all together, we see that there are clear links between the bimodal structure visible in the distribution of $R_{2-1/1-0}$ and the mean values of the physical conditions (density, temperature, etc.) within the cloud. Lines-of-sight with high $R_{2-1/1-0}$ preferentially probe regions with high CO column densities, high mean densities and low temperatures. Conversely, lines-of-sight with low $R_{2-1/1-0}$ probe regions with low CO column densities, low mean densities and high mean temperatures. However, these relationships do not explain why the transition from low $R_{2-1/1-0}$ to high $R_{2-1/1-0}$ occurs so suddenly, or why it is the CO column density in particular that best predicts when this transition will occur. To understand why this happens, we need to look at how the CO line opacities vary within the cloud.

4.3.4 OPTICAL DEPTH EFFECTS

To investigate the influence that line opacity has on the value of $R_{2-1/1-0}$, we have computed the optical depths of both CO lines using RADMC-3D. For each line of sight, we first compute the optical depth individually for each velocity channel. We then average these values to produce a single representative value of τ . To construct this average, we weight the contribution of each velocity channel by the contribution it makes to the velocity-integrated brightness temperature of the line, i.e.

$$\tau_{\text{W}} = \frac{\sum T_{\text{b},i} \times \tau_i \times dv}{W_{\text{CO}}} \quad (4.2)$$

where $T_{\text{b},i}$ is the brightness temperature in velocity channel i , τ_i is the corresponding optical depth, and dv is the width of the channel. It is worth noting that the way τ_i is computed is analogous to how an image is computed in RADMC-3D (Dullemond,

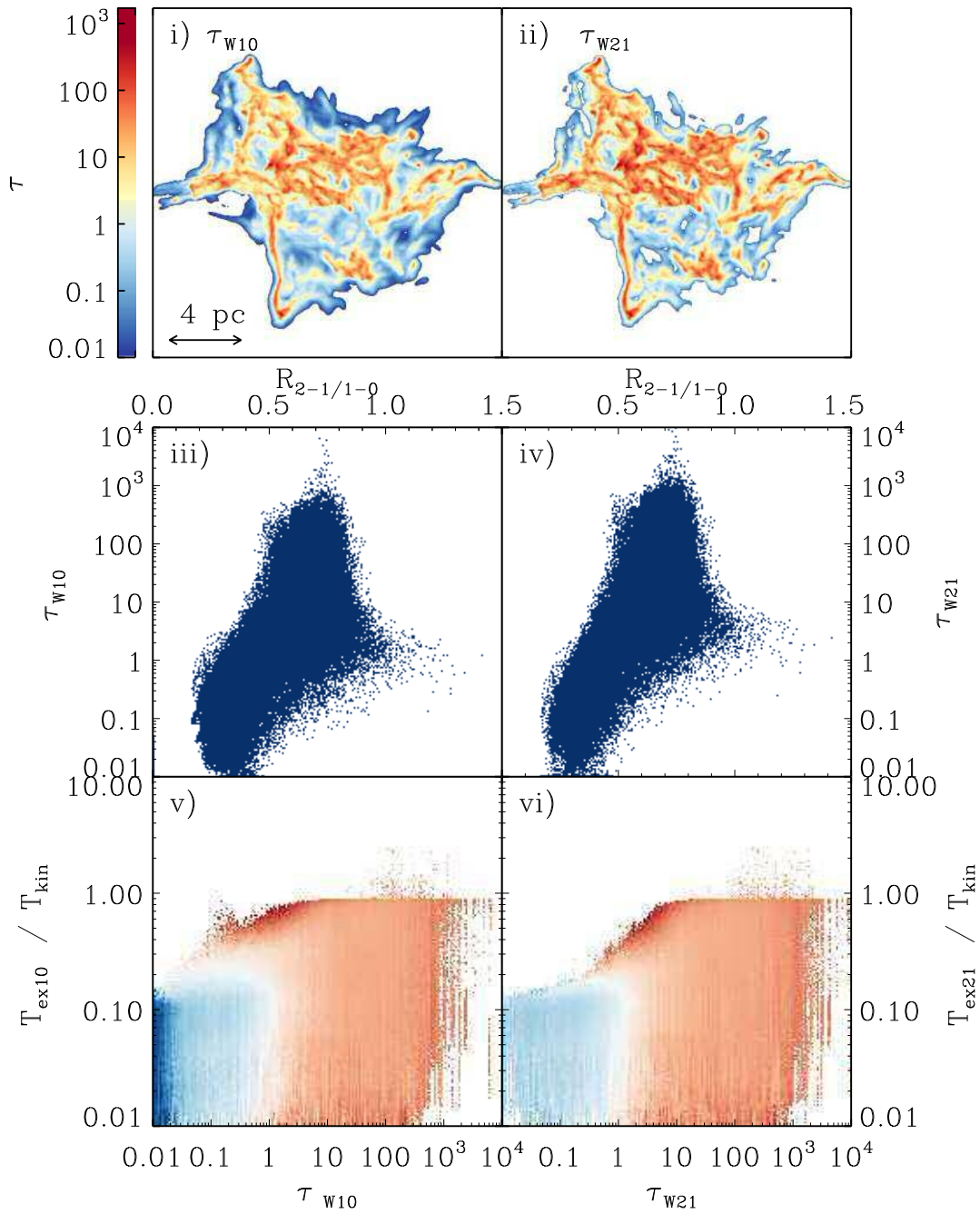


Figure 4.5. Panels i) and ii) show Integrated opacity image weighted by integrated intensity for both lines (τ_{W10} and τ_{W21} respectively). Panels iii) and iv) show τ_W , plotted as a function of $R_{2-1/1-0}$ for both lines illustrating how the ratio and opacity are correlated. Panels v) and vi) show $T_{\text{ex}}/T_{\text{kin}}$ plotted as a function of τ_W for each line and colour coded with $R_{2-1/1-0}$ the same colour scale as Fig. 4.4

2012). Therefore τ_i is not the mean opacity seen by a single cell along the line of sight, but rather the total integrated opacity along the line of sight for each velocity channel. As such the resulting image is dependent on the 3D velocity field, in the same way our integrated intensity maps are, given that we use the LVG approximation to account for non-LTE effects.

In Fig. 4.5, panels (i) and (ii) show how τ_W varies as a function of position for the CO 1-0 and 2-1 lines, respectively. A quick comparison with Fig. 4.1 suggests a correlation between optically thick lines of sight ($\tau > 1$) and $R_{2-1/1-0} \sim 0.7$. Additionally, along these lines of sight, τ_{W21} seems to both be larger and to increase faster than τ_{W10} .

The correlation between τ and $R_{2-1/1-0}$ becomes more evident in panels (iii) and (iv) of Fig. 4.5. Values of $R_{2-1/1-0} \sim 0.7$ can be mostly attributed to emission coming from optically thick lines of sight, whereas values of $R_{2-1/1-0} \sim 0.3$ originate from optically thin lines of sight. The influence of τ on the level populations is further emphasised in panels (v) and (vi), where we plot the ratio of the CO excitation temperature T_{ex} and the kinetic temperature T_{kin} as a function of τ_W . Panel (v) shows the results for the 1-0 line and panel (vi) shows the results for the 2-1 line. We see that along most lines of sight with $\tau < 1$, both transitions are strongly sub-thermal, with excitation temperatures that are much less than the kinetic temperature. This is to be expected: we have already seen that most of this emission comes from gas with a density $n < 100 \text{ cm}^{-3}$, far below the critical density of even the 1-0 line, and since $\tau < 1$, even if a small amount of radiative trapping occurs, it is insufficient to change this conclusion.

Along lines of sight with $\tau > 1$, the behaviour is more complex. On physical grounds, we expect that $T_{\text{ex}} \rightarrow T$ as $\tau \rightarrow \infty$, where T is the kinetic temperature of the gas. From Fig. 4.5, we see that we do indeed recover this behaviour for some of the gas along the sight-lines with high optical depth. However, we also see that there are other regions along each high τ sight-line where the emission is sub-thermal. The key to understanding this behaviour is the fact that the quantity directly responsible for influencing the level populations is not the same quantity that we are dealing with when we compute and plot τ_W . Although there is a correlation between the mean optical depth along a sight-line and the angle-averaged optical depths probed by that sight-line, the highly inhomogeneous structure of the cloud causes this correlation to be fairly weak (see e.g. Clark & Glover, 2014). Therefore, the emission that we see along the $\tau > 1$ sight-lines comes from a mix of sub-thermal and thermalised gas, explaining why we do not simply recover a value of 1 for $R_{2-1/1-0}$.

4.4 DISCUSSION

Our synthetic images recover the expected peak in the CO 2-1/1-0 line ratio at $R_{2-1/1-0} \sim 0.7$, but also indicate the existence of a second peak in the line ratio distribution at $R_{2-1/1-0} \sim 0.3$. The first peak is produced by emission from CO in cold, dense regions of the cloud and our analysis in the previous section shows that much of this CO is optically thick. On the other hand, the second peak is produced by emission from optically thin, sub-thermally excited CO in warm, diffuse regions of the cloud.

Our analysis therefore suggests that the value of $R_{2-1/1-0}$ can potentially be used as a probe of the physical conditions within a molecular cloud. By detecting both CO lines and determining whether $R_{2-1/1-0}$ is found in the high peak or the low peak, we can place constraints on the density, temperature and optical depth of the CO-emitting gas. Validating the existence of the low ratio peak with observational studies will therefore be important to establish $R_{2-1/1-0}$ as a potential observational tool for confidently distinguishing the different regions within a GMC. However, we caution that it remains to be seen whether the $R_{2-1/1-0}$ distribution that we see in this particular cloud is universal or is a result of our choice of initial conditions and/or ISRF. However, what is clear is that for this particular cloud – i.e. the physical properties, and environmental conditions – $R_{2-1/1-0}$ has a well-defined bimodal structure that corresponds to the physical state of the gas, such as its temperature, density and resulting level populations.

4.5 CONCLUSIONS

We have used a numerical simulation of a turbulent molecular cloud to investigate the behaviour of the ratio of the velocity-integrated brightness temperatures of the first two emission lines of CO, defined as $R_{2-1/1-0} = W_{21}/W_{10}$. Our simulated cloud has properties similar to those found in nearby star-forming clouds. We have used SPH to model the chemical, thermal and dynamical evolution of the cloud, and then post-processed the simulation output using a radiative transfer code to generate synthetic CO emission maps. Our main findings can be summarised as follows:

1. The area-weighted PDF of $R_{2-1/1-0}$ has a bimodal distribution with two main peaks, at ~ 0.7 and ~ 0.3 . This clear bimodal structure correlates well with the optical depths of the CO lines. Along optically thin lines of sight, the CO excitation is strongly sub-thermal and the resulting value of $R_{2-1/1-0}$ is small. On the other hand, along optically thick lines of sight, we probe a mix

of sub-thermal and thermal emission, resulting in a much higher value of the line ratio.

2. The high ratio peak primarily traces the cold ($T \leq 40$ K) and dense ($n \geq 10^3 \text{ cm}^{-3}$) molecular gas within the molecular cloud. This value is similar to the “canonical” value of $R_{2-1/1-0}$ often quoted in the literature, and also to the values measured in local molecular clouds. (Sakamoto et al., 1994; Nishimura et al., 2015)
3. The low ratio peak traces more diffuse ($n \leq 10^3 \text{ cm}^{-3}$) and warmer ($T \geq 40$ K) molecular gas within the cloud. This gas contains much less CO and so the emission from these regions is much fainter, requiring high sensitivity to detect. We note that Nishimura et al. (2015) reported values of $R_{2-1/1-0} \sim 0.4 - 0.5$ towards the outskirts of Orion, consistent with the range of values we find for their limiting sensitivity.

As such the value of $R_{2-1/1-0}$ can be indicative of the physical conditions in a particular region of a cloud. Further study, exploring a wide range of environmental conditions, is required to see whether the result we present here is universal. We explore this on the following Chapter.

CHAPTER 5

CO LINE RATIOS IN MOLECULAR CLOUDS: THE IMPACT OF ENVIRONMENT*

5.1 INTRODUCTION

The evolution, structure and physical properties of giant molecular clouds (GMCs) are highly dependant on the surrounding environmental conditions (Klessen & Glover, 2016). The changes in the surrounding environment of GMCs can have a direct impact on the formation of stars, since it is within these complicated cloud complexes that most of the molecular gas, which eventually will be transformed into stars, is contained. The bulk mass of the molecular gas is stored in molecular hydrogen (H_2) that unfortunately due to the low temperatures of GMCs cannot be directly observed. Therefore empirically derived relations help estimate the total molecular content by making use of other molecular tracers.

Carbon monoxide's (CO) easily excited rotational lines make it one of the most well known tracers of the interstellar medium (ISM), as such we rely on CO emission to estimate the total molecular content of a GMC. The X-factor (X_{CO}) allows us to estimate the total molecular gas of a GMC from the integrated intensity of the $J = 1 - 0$ emission line of CO by

$$N_{\text{H}_2} = X_{\text{CO}}W_{10}, \quad (5.1)$$

where N_{H_2} is the column density of H_2 , W_{10} the integrated intensity of the

*The work presented in this Chapter is based on the published work in Peñaloza et al. (2018)

$J = 1 - 0$ transition of CO and X_{CO} the empirically derived conversion factor. Several studies have already explored the accuracy of X_{CO} and its dependance on environmental conditions (Bolatto, Wolfire & Leroy, 2013; Papadopoulos et al., 2012a; Sandstrom et al., 2013; Clark & Glover, 2015; Offner et al., 2014)

As distances become larger, it becomes harder to resolve far away clouds in nearby galaxies. Extragalactic studies therefore rely on higher order rotational transitions with smaller wavelengths since they provide a higher resolution at no observational cost. Most commonly used are the $J = 2 - 1$ and $J = 3 - 1$ rotational transition lines since they are considerably bright and easily observed. The drawback however is that X_{CO} is an empirical relation that is only calibrated for the $J = 1 - 0$ emission line. Observers rely in another relation, the integrated intensity of $J = 2 - 1$ emission line (W_{21}) is converted to W_{10} by using the empirically derived ratio R_{21} . Similarly R_{31} is used to convert from W_{32} to W_{10} .

These ratios are key tools when deriving physical quantities from observations and to establish star formation relations. Typically, extragalactic studies adopt a value of $R_{21} = 0.7$ (Eckart et al., 1990; Casoli et al., 1991; Brand & Wouterloot, 1995; Sakamoto et al., 1997; Hasegawa, 1997; Sawada et al., 2001; Bigiel et al., 2008; Leroy et al., 2009; Barriault, Joncas & Plume, 2011) to convert from W_{21} to W_{10} . However, this could be inaccurate given the results shown in Peñaloza et al. (2017), which suggest R_{21} has a bimodal distribution that is dependant on the physical conditions surrounding the emitting gas. Another example of a widely-used ratio is R_{31} , which is mostly used to study star formation in high redshift galaxies (Aravena et al., 2010; Bauermeister et al., 2013; Aravena et al., 2014; Daddi et al., 2015). In most of these cases the $J = 3 - 2$ emission line is observed and then converted using the standard value $R_{31} \sim 0.5$ (Aravena et al., 2014), before deriving any physical properties of the system.

Considering how heavily we rely on line ratios as conversion factors, their behaviour is not well understood and their value is dependent on the observed objects (Vlahakis et al., 2013; Papadopoulos et al., 2012b). This makes understanding their behaviour very difficult given how degenerate the dependance of CO line ratios is on environment. Fortunately numerical simulations provide a way through which these ratios can be studied and their behaviour and dependancies on environment properly quantified.

We numerically follow the evolution of GMCs that are post-processed to produce synthetic observations. The aim is to gain a better understanding of the ratios of CO's rotational emission lines and how they are influenced by changes in mass, density, size, metallicity, the Interstellar Radiation Field (ISRF) and the cosmic ray

ionization rate (CRIR). Therefore we simulate a set of clouds in which the initial conditions are systematically changed in order to cover a wide range of realistic environmental conditions.

The structure of this Chapter is as follows. In section 5.2 we describe the numerical setup and the initial conditions used to model the evolution and synthetic observations of these GMCs. In section 5.3 we present our results. We look at how the cloud's morphology changes depending on environment as well as the impact this has on the value and distribution of R_{21} . In section 5.4 we examine how variations in environment impact the observation of unresolved GMCs and the consequences this has on different line ratios. In section 5.5 we discuss how variations on R_{21} and R_{31} affect calculated column densities of H_2 as well as whether R_{21} can trace changes in CO abundances. Finally we summarise our findings in section 5.6.

5.2 METHOD

5.2.1 INITIAL CONDITIONS

We produce a set of numerical simulations with different initial conditions to study the impact of environment on the evolution of GMCs and the impact this has on CO emission lines. The initial setup of all the clouds is a uniform sphere where a turbulent velocity field with a power spectrum of $P(k) \propto k^{-4}$ is imposed and left to decay as the cloud evolves. Since the aim of this study is to look at the structure and evolution of GMCs prior to the onset of star formation, we therefore stop each run just before the first sink particle i.e. star is formed. It is important to note that since the initial conditions affect the evolution of each cloud, the time when the first sink forms will be different for each run. We make use of the clouds simulated in previous papers by Clark & Glover (2015) and Glover & Clark (2016) since they already cover part of the parameter space we intend to study. Below we cover what the variations in initial conditions are but refer the reader to those papers for a full details.

First we summarise the initial conditions of the simulations by Clark & Glover (2015). They cover a range of different ISRFs intensities that are scaled proportional to G_0 , where $G_0 = 1.7$ in Habing (1968) units and a range of CRIRs that are scaled proportional to $\zeta_{\text{H}} = 3 \times 10^{-17} \text{ s}^{-1}$. These clouds have a mass of either $10^4 M_{\odot}$ or $10^5 M_{\odot}$. Additionally the initial density is varied to be either $n = 100 \text{ cm}^{-3}$ or $n = 10000 \text{ cm}^{-3}$. Lastly since the initial state of the gas can delay the formation of CO and therefore its total emission, the initial molecular fraction is changed to be either $f(\text{H}_2) = 1$ or $f(\text{H}_2) = 0$, i.e. fully molecular or fully atomic. All of these runs

were performed with a turbulent velocity field generated from a 'natural' mix.

The simulations by Glover & Clark (2016) have all an initial mass of $10^4 M_\odot$, initial density of $n = 276 \text{ cm}^{-3}$, have an initial molecular fraction of $f(\text{H}_2) = 0$ and have turbulent velocity field that is generated from purely solenoidal modes. In addition the ISRF and CRIR are scaled in the same way as Clark & Glover (2015), however the CRIR is scaled proportional to $\zeta_{\text{H}} = 1 \times 10^{-17} \text{ s}^{-1}$. Finally the initial metal fraction is varied with respect to solar metallicity (Z_\odot), the initial metallicities used are $Z = Z_\odot$, $Z = 0.5 Z_\odot$ and $Z = 0.2 Z_\odot$.

Due to the fact that these set of clouds were initially performed for other studies it is understandable that they cover a slightly different parameter space. We perform an additional set of simulations in order to bridge the gap between these two sets of clouds and disentangle the effect of varying certain parameters. Both Clark & Glover (2015) and Glover & Clark (2016) scale the ISRF and CRIR together making it hard to disentangle the effect of either, therefore we run 4 clouds that vary either the ISRF or the CRIR. Additionally the small mass clouds in Clark & Glover (2015) and all of the clouds in Glover & Clark (2016) have a slightly different initially density, different turbulent velocity field, a different α_{vir} and slightly different ζ_{H} . As such we do 4 extra simulations where only one of these parameters is varied.

We summarise the set of simulations used in this study and their initial conditions in Table 5.1. Note that the IDs given in this table will be used throughout this Chapter.

5.2.2 POST-PROCESSING

Once the hydrodynamical simulation is finished we post process the snapshot with RADMC-3D (Dullemond, 2012) and create synthetic images. Given that we have clouds of different sizes and densities, we used the refining method developed in Peñaloza et al. (2017) to account for all particles in the GADGET-2 snapshot. This assures that no information is lost when interpolating particles to the grid and therefore guarantees convergence of the intensity maps which is important when comparing line ratios of different size clouds. Additionally, we have implemented an extension to the Sobolev approximation in RADMC-3D (Shetty et al., 2011), that accounts for both the velocity and density variations within the cloud. By making use of density gradients within the cloud we can better calculate the local optical depth and therefore the total emission for the cloud. A more detailed description is given in Section 3.2. Since radiative transfer simulations of clouds in Clark & Glover (2015) and Glover & Clark (2016) were performed without these additional methods, we

ID	$n(\text{cm}^{-3})$	M_{\odot}	α_{vir}	G_0	CRIR	$f(\text{H}_2)$	Z_{\odot}	Turbulence	Notes
Clark & Glover (2015)									
CG15-M4-G1	100	10^4	0.5	1	1	1	1	Natural	
CG15-M4-G10	100	10^4	0.5	10	10	1	1	Natural	
CG15-M4-G100	100	10^4	0.5	100	100	1	1	Natural	
CG15-M5-G1	100	10^5	0.5	1	1	1	1	Natural	
CG15-M5-G10	100	10^5	0.5	10	10	1	1	Natural	
CG15-M5-G100	100	10^5	0.5	100	100	1	1	Natural	
CG15-M5-G1/A	100	10^5	0.5	1	1	0	1	Natural	
CG15-M5-G100/A	100	10^5	0.5	100	100	0	1	Natural	
CG15-CMZ1	10000	10^5	0.5	100	100	1	1	Natural	
CG15-CMZ2	10000	10^5	2	100	100	1	1	Natural	
Glover & Clark (2016)									
GC16-Z1-G1	276	10^4	1	1	1	0	1	Solenoidal	$\zeta_{\text{H}} = 1 \times 10^{-17} \text{s}^{-1}$
GC16-Z1-G10	276	10^4	1	10	10	0	1	Solenoidal	$\zeta_{\text{H}} = 1 \times 10^{-17} \text{s}^{-1}$
GC16-Z1-G100	276	10^4	1	100	100	0	1	Solenoidal	$\zeta_{\text{H}} = 1 \times 10^{-17} \text{s}^{-1}$
GC16-Z05-G1	276	10^4	1	1	1	0	0.5	Solenoidal	$\zeta_{\text{H}} = 1 \times 10^{-17} \text{s}^{-1}$
GC16-Z05-G10	276	10^4	1	10	10	0	0.5	Solenoidal	$\zeta_{\text{H}} = 1 \times 10^{-17} \text{s}^{-1}$
GC16-Z05-G100	276	10^4	1	100	100	0	0.5	Solenoidal	$\zeta_{\text{H}} = 1 \times 10^{-17} \text{s}^{-1}$
GC16-Z02-G1	276	10^4	1	1	1	0	0.2	Solenoidal	$\zeta_{\text{H}} = 1 \times 10^{-17} \text{s}^{-1}$
GC16-Z02-G10	276	10^4	1	10	10	0	0.2	Solenoidal	$\zeta_{\text{H}} = 1 \times 10^{-17} \text{s}^{-1}$
GC16-Z02-G100	276	10^4	1	100	100	0	0.2	Solenoidal	$\zeta_{\text{H}} = 1 \times 10^{-17} \text{s}^{-1}$
Additional Runs									
M4-G1-CR10	100	10^4	0.5	1	10	1	1	Natural	
M4-G1-CR100	100	10^4	0.5	1	100	1	1	Natural	
M4-G10-CR1	100	10^4	0.5	10	1	1	1	Natural	
M4-G100-CR1	100	10^4	0.5	100	1	1	1	Natural	
M4-G1-CR0.3	100	10^4	0.5	1	0.3	1	1	Natural	
M4- α 1	100	10^4	1	1	1	1	1	Natural	
M4-N300	300	10^4	0.5	1	1	1	1	Natural	
M4-SOL	100	10^4	0.5	1	1	1	1	Solenoidal	

Table 5.1. In this table we summarise the initial conditions for each cloud. The virial conditions of the clouds are given by $\alpha_{vir} = E_{\text{kin}}/E_{\text{pot}}$. G_0 is given in Habing (1968) units and cosmic rays have a base ionization rate of $\zeta_{\text{H}} = 3 \times 10^{-17} \text{s}^{-1}$ unless otherwise specified. $f(\text{H}_2)$ denotes the initial molecular fraction of the gas and Z_{\odot} its metallicity.

re-do the radiative transfer for these clouds.

For each cloud we create synthetic observations for the first three rotational lines of ^{12}CO ($J = 1 - 0$, $J = 2 - 1$, $J = 3 - 2$). Integrating along the z-axis i.e. velocity in PPV space, we then create zeroth moment maps for each line. All the final maps have an imposed cut at emissions lower than 0.01 K km s^{-1} , this is motivated by our previous study (Peñaloza et al., 2017). All these maps are 'ideal' synthetic observations since they do not include any noise or telescope effects.

Finally it is worth noting that we only study the first three rotational lines of CO since higher Js require additional physics in our numerical simulations. Higher CO transitions are normally excited by high velocity shocks within the clouds (Pellegrini et al., 2013; Pon et al., 2016); these shocks are not well resolved by 3D numerical simulations, and so the microphysics of such regions are not properly traced by our models.

5.3 RESULTS

5.3.1 CLOUD MORPHOLOGY AND APPEARANCE

To qualitatively illustrate how the cloud morphology changes, Figure 5.1 contains the following simulations CG15-M4-G1, CG15-M5-G1, CG15-M5-G100 and GC16-Z1-G1. In the upper panels of Figure 5.1 we present the column densities at the time where the synthetic observations are created. The same seed clearly leaves an imprint on the cloud's structure and this is evident when comparing the column densities of the CG15 clouds with the GC16 cloud. Middle panels show the synthetic observations for the second rotational line of ^{12}CO ($J = 2 - 1$). The synthetic observations are able to recover the general structure of the cloud, however the filamentary structures seen in the column density maps are not as easily identified in the emission maps, due to the quick saturation of CO emission lines.

Comparing the first two columns of Figure 5.1 reveals the impact a change in mass plays in the evolution of the clouds. By increasing the mass but maintaining the initial density the size of the cloud is effectively doubled. This results in a Mach number roughly 4 times larger than for CG15-M4-G1 and leads the gas to be more shocked. As a consequence the cloud has a more intricate web-like structure with a larger number of turbulence driven filaments as well as increasing the column densities of already existing ones. This can be seen in the column density map of CG16-M5-G1. This is reflected in the synthetic images since high density regions correlate with high intensity regions and viceversa, and as we shall see this is an important factor in the

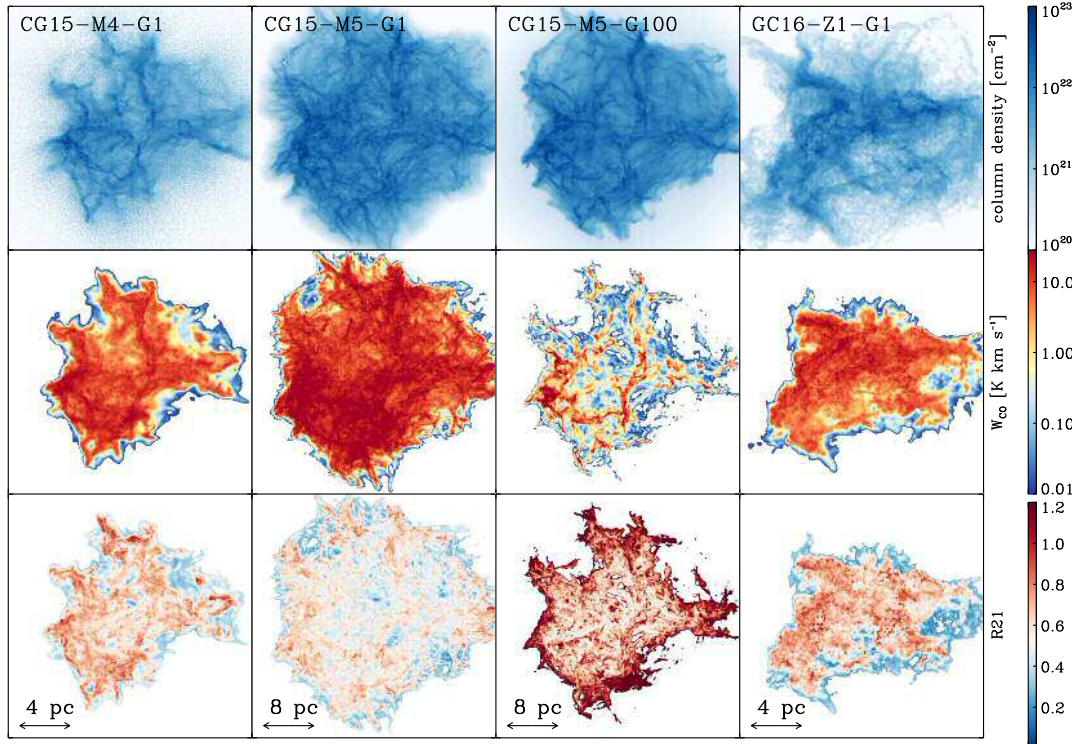


Figure 5.1. Top row: Column density maps for simulations CG15-M4-G1, CG15-M5-G1, CG15-M5-G100 and GC16-Z1-G1. Middle row: The integrated intensity of the second rotational transition line of CO for each simulation. Bottom row: The ratio, R_{21} , of the integrated intensity of the first two rotational transition lines of CO for each simulation.

distribution of R_{21} .

The middle two columns show the effect of varying the ISFR and the CRIR. In the high ISRF/CRIR scenario most of low density, poorly shielded CO has been dissociated and therefore the thin, low density filaments have completely disappeared. More evident in the synthetic observations is how the apparent size of the cloud has been reduced by removing the low intensity regions that were previously enveloping the entire cloud.

Finally the bottom panels of Figure 5.1 contain the R_{21} maps. As shown by Peñaloza et al. (2017) R_{21} has a bimodal distribution with peaks centred at $R_{21} \sim 0.3$ and $R_{21} \sim 0.7$. In the first two columns, it is clear that the ratio map is mostly dominated by values of $R_{21} \sim 0.7$, nonetheless lower values of R_{21} are present in regions where $W_{21} < \text{few K km s}^{-1}$. A very different picture is seen in the R_{21} map for CG15-M5-G100, towards the centre of the cloud $R_{21} \sim 0.5-0.7$ but at the outskirts of the cloud $R_{21} > 1$. The high ISRF results in very high temperatures ($T > 40\text{K}$) at the edge of very dense ($n > 10^3\text{cm}^{-3}$) regions of the cloud. Additionally if the $\tau = 1$ surface for $J = 1 - 0$ is behind the $\tau = 1$ surface for $J = 2 - 1$ then W_{21} will be larger than W_{10} . In these conditions $R_{21} > 1$, as shown by 1-D models (Sakamoto et al., 1994). It is worth noting that R_{21} can also be larger than 1 when the source of radiation is embedded within the cloud (See Figure 11 from Nishimura et al. (2015)). Finally when comparing R_{21} between CG15-M4-G1 and GC16-Z1-G1 it is clear that the turbulent seed and therefore the morphology of the cloud have an impact on the final value of R_{21} .

Qualitatively the ISRF and the CRIR have the biggest impact on R_{21} 's value and distribution. Their combined effects can hinder the accuracy of adopting a constant value of $R_{21} \sim 0.7$ and therefore over or underestimate the value of W_{10} .

5.3.2 SYSTEMATIC VARIATIONS OF R_{21}

The morphology of the cloud gives a qualitative picture of the impact initial mass, turbulence and the ISRF/CRIR have on CO emission and its line ratios. These different effects on the ratio can be quantified by plotting the cumulative PDF of R_{21} weighted by integrated intensity (Figure 5.2) which illustrates the variable nature of R_{21} . The separation between the curves for each cloud shows how changes in environmental conditions impact the distribution and average value of R_{21} . This relies on the knowledge that low values of the ratio ($R_{21} \sim 0.2 - 0.4$) are associated with warm and diffuse gas, while high values of the ratio ($R_{21} \sim 0.6 - 0.8$) are associated with cold and dense gas (Peñaloza et al., 2017). Below we examine this in

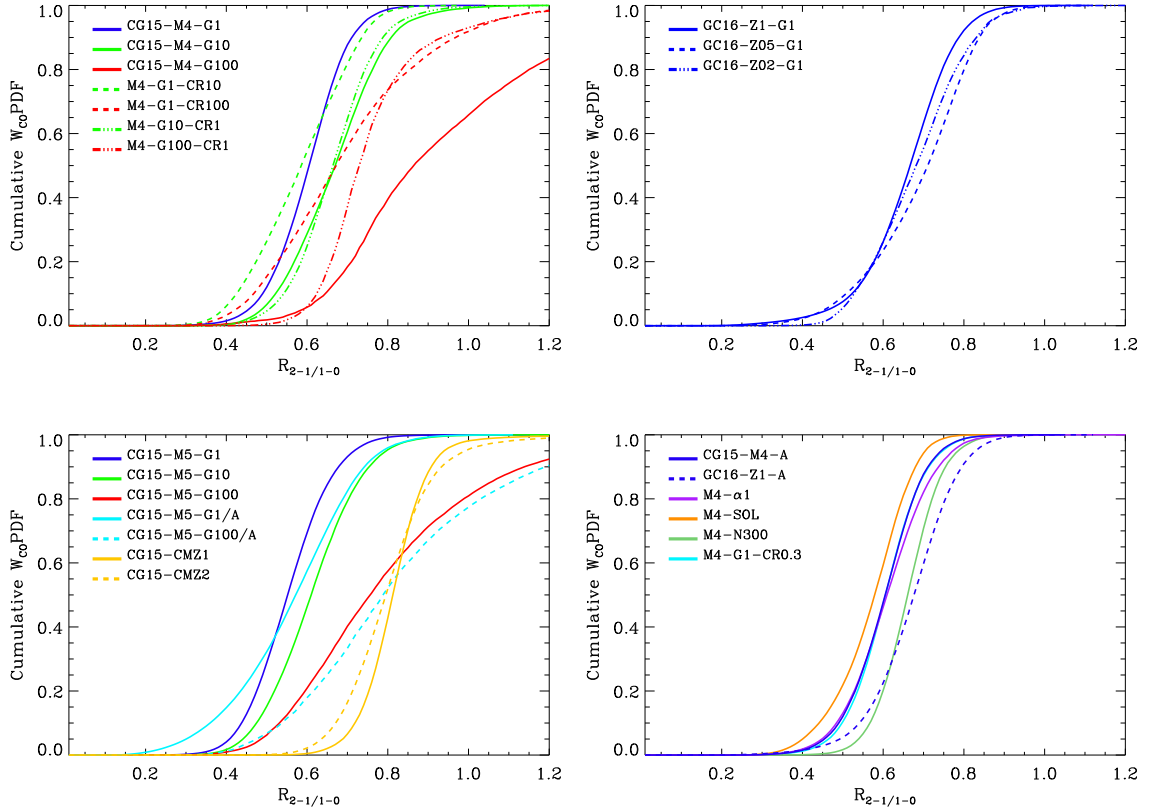


Figure 5.2. The cumulative PDF of R_{21} weighted by W_{CO} for different sets of clouds grouped by variations in their physical parameters. Top left: Small clouds ($10^4 M_{\odot}$), at solar metallicities and with varying ISRF, CRIR or both. Top right panel: Small clouds ($10^4 M_{\odot}$), with a solenoidal turbulent seed and varying metallicities. Bottom left panel: Large clouds ($10^5 M_{\odot}$) with variations in both ISFR and CRIR. Cyan lines are clouds that start atomic and yellow lines clouds with initial $n = 10000 \text{ cm}^{-3}$. Bottom right panel: Small clouds ($10^4 M_{\odot}$) with changes to α_{vir} , initial density or the turbulent seed

more detail.

R_{21} 's dependence on the ISFR and the CRIR

The top left panel of Figure 5.2 plots the cumulative PDF for a set of the low mass clouds at solar metallicities. As the ISFR and the CRIR increase (solid lines), a larger fraction of the overall emission is associated with larger values of R_{21} . In this case almost half of the emission is associated with line ratio values of $R_{21} > 1$. As the ISFR increases the unshielded molecular gas is fully dissociated, destroying most of the CO in the already diffuse gas and therefore resulting in no emission of CO from these regions of the cloud. This is consistent with the fact that lower values of the

ratio ($R_{21} \sim 0.3$) are associated with diffuse areas of the cloud (Sakamoto et al., 1994; Peñaloza et al., 2017). Similar to CG15-M5-G100 (see bottom left panel and Figure 5.1), values of $R_{21} > 1$ are correlated with CO emission originating from dense and hot gas at the edge of the cloud.

The dashed-dotted lines represent the runs where only the ISRF field was increased while the CRIR was left unchanged. For these clouds a large fraction of the emission is also associated with higher line ratios. However a larger fraction (about 80 %) of the overall emission is associated with line ratios of $R_{21} \sim 0.6 - 0.8$. A smaller CRIR means the dense gas within the shielded regions of the cloud is not being heated and therefore results in a more compact cloud. As such most of the emission is originating from dense and cold gas, which explains why a larger fraction of the emission is correlated with $R_{21} \sim 0.7$.

On the other hand the dashed lines represent the clouds where the ISRF was left constant while the CRIR were increased. In this case about 50 % of the overall emission is correlated with lower line ratios ($R_{21} \sim 0.3 - 0.6$). As shown by Glover & Clark (2016) an increase in ζ_H can lead to a decrease in CO abundance. Even though the total abundance of CO has been reduced it is still well shielded from the UV rays, resulting in emission originating from low density gas and therefore associated with lower line ratio values. The effect of ζ_H on CO abundance will be more thoroughly discussed in Section 6.5.

Finally by looking at the bottom left panel we can see that the compound effect of the ISRF and the CRIR is still the same even if mass of the cloud is higher. As discussed in the previous section changing the mass of the cloud increases the number of turbulence driven filaments. These will quickly be eroded by the high ISRF and any low density gas, and increasing the overall value of R_{21} in the same way as it would be for a lower mass cloud.

R_{21} 's dependence on the metallicity

The top right panel of Figure 5.2 plots the cumulative PDF of small clouds ($10^4 M_\odot$), with a solenoidal turbulent seed and varying metallicities. Reducing the metallicity slightly reduces the fraction of the overall emission correlated with lower line ratios. Since at lower metallicities the conditions to form CO are only triggered within dense cores (Glover & Clark, 2016), this results in less CO emission from diffuse regions of the cloud in low metallicity environments. This effectively reduces the percentage of the low values of R_{21} that are associated with low density gas.

On the other hand low metallicities also mean the gas is more inefficient at

forming molecular gas, which will reduce the density in previously dense regions of the cloud. This slightly increases the average value of R_{21} since the $J = 2 - 1$ emission line has a slightly higher critical density and therefore will be harder to excite. However given that the high densities ($n > n_{\text{crit}}$) required to excite CO are easily reached, the overall impact of changing the metallicity on R_{21} is very small.

R_{21} 's dependence on mass and molecular fraction

The bottom left panel of Figure 5.2 contains all the clouds with total mass of $10^5 M_{\odot}$. The first thing to notice is, by comparing the blue lines in the top and bottom left panels, that increasing the total mass of the cloud leaves the overall value and distribution of R_{21} relatively unchanged.

As it can be observed the effect of changing the initial molecular fraction is on the fraction of the overall gas associated with lower line ratios, where about 40 % of the emission has values of $R_{21} < 0.5$ for clouds that start fully atomics. This tail at low values of R_{21} is correlated with a larger fraction of the emission coming from low density/high temperature regions. This is consistent with the idea that less molecular material at the beginning will delay the formation of CO (Glover & Clark, 2012b), resulting in lower column densities of CO. Given that impact of ISRF and CRIR is much stronger, as discussed above, the effect of initial $f(H_2)$ can be more easily observed at low ISRF.

Finally the two CMZ-like runs have an initial density of $n = 10000 \text{ cm}^{-3}$ have a larger average value of R_{21} , where most of the overall emission is associated with $R_{21} \sim 0.8$. This is due to the fact that the initial density is well above the critical density of the first two rotational transition lines of CO ($n_{\text{crit},1-0} \approx 2000 \text{ cm}^{-3}$, $n_{\text{crit},2-1} \approx 10^4 \text{ cm}^{-3}$). As a result the gas is well shielded from the ISRF and CO is easily excited. Since most of the emission is originating from high density gas, this means that R_{21} will be centred near ~ 0.7 .

R_{21} 's dependence on Turbulence, α_{vir} and initial density

As mentioned before we have used clouds from Clark & Glover (2015) and Glover & Clark (2016), however as it can be seen in Table 5.1 these have slightly different initial conditions. The bottom right panel of Figure 5.2 shows the clouds that explore variations in only these initial conditions. First we must note that even though CG15-M4-G1(blue solid line) and GC16-Z1-G1(blue dashed line) have very similar initial conditions, the changes in turbulence, α_{vir} and initial density still considerably change R_{21} 's distribution.

Using a solenoidal turbulent velocity field increases the fraction of overall emission associated with lower line ratios, effectively decreasing the average value of R_{21} . Given that a solenoidal turbulent field has no compressive motions ($\nabla \cdot \mathbf{u} = 0$) this results in a more flocculent cloud (i.e. diffuse), as mentioned in the previous section. This results in a larger fraction of the emission originating from more diffuse gas, which is correlated with lower values of the ratio, and explains the decrease in R_{21} .

Increasing the value of α_{vir} slightly increases the average value of R_{21} . A larger kinetic energy will make the gas within certain regions of the cloud to be compressed due to the higher velocities and quickly reach high densities. Sink particles will then quickly form before the rest of the cloud has had enough time to collapse, leading to the overall cloud looking more compact. As such a slightly larger fraction of the cloud will be association with larger values of R_{21} .

The green line shows, to a lesser extent, what was observed for CMZ-like clouds; increasing the initial density reduces the amount of diffuse gas and effectively increases the fraction of the gas associated with higher values of R_{21} . The slightly different ζ_{H} between CG15-M4-G1 and GC16-Z1-G1 has very little effect, this can be seen by the cyan line where $\zeta_{\text{H}} = 1 \times 10^{-17} \text{s}^{-1}$. Given that the variation in ζ_{H} is small the change in R_{21} is not substantial. However reducing the CRIR does slightly reduce the amount of emission associated with low line ratios. Finally we note that the combined effect of turbulence, α_{vir} , initial density and slightly different ζ_{H} explain the different average value and distribution of R_{21} between CG15-M4-G1 and GC16-Z1-G1.

5.4 R_{21} FROM OBSERVATIONALLY UNRESOLVED CLOUDS

The previous section explained how variations in the initial conditions and of the surrounding environment have an impact on R_{21} 's value and distribution. Moreover the value of the line ratio can be associated with different regions of the cloud and is correlated with local physical properties of the gas. However when comparing to observations in an extragalactic context, where R_{21} is used as a conversion factor, details about the varying value of R_{21} within molecular clouds are not important. In this context one of our clouds will most likely be smaller than the size of the beam of nearby galaxy surveys (Bigiel et al., 2016; Schinnerer et al., 2013) and therefore the total intensity of a GMC will be averaged within this beam. Therefore to study R_{21} in the context of observationally unresolved clouds, we first take the area-weighted intensity average of each cloud for each rotational transition line and then take the ratio of the two averaged intensities.

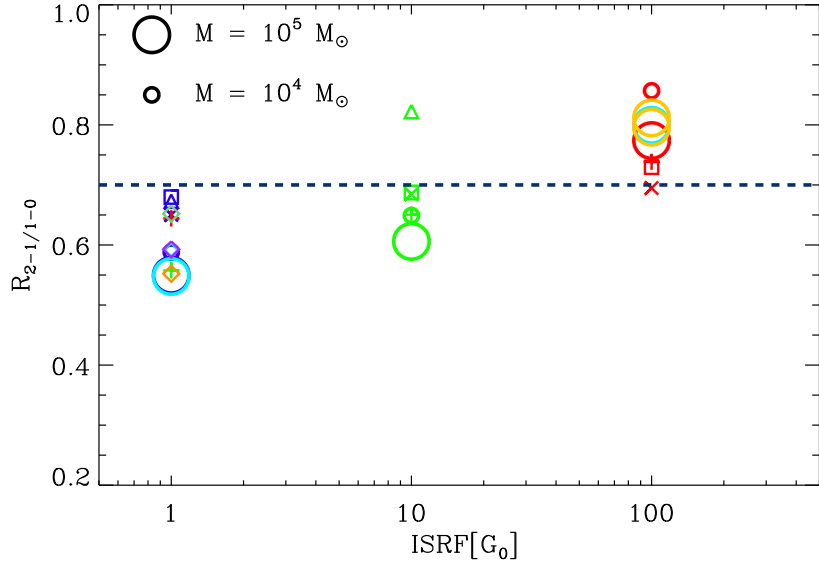


Figure 5.3. The averaged value of R_{21} for each cloud as a function of their respective ISRF (G_0). Large circles represent clouds that have a mass of $M = 10^5 M_\odot$ and small shapes represent clouds with a mass of $M = 10^4 M_\odot$. Blue, green and red shapes represent an increase of the ISRF and/or CRIR by 1, 10 or 100 respectively. Xs, squares and triangles represent metallicities of Z_\odot , $0.5Z_\odot$ and $0.2Z_\odot$ respectively. Large cyan circles denote an initial hydrogen fraction of $f(H_2) = 0$. Yellow circles are the two runs with an initial number density of $n = 10000 \text{ cm}^{-3}$. Plus signs are clouds where the ISRF and the CRIR have been varied independently. Diamonds are the additional runs plotted in the bottom right panel of Figure 5.2 and have the same colours. Finally the dashed line represents the standard value used for converting W_{21} to W_{10} . Note: we have not included GC16-Z02-G100 since the gas is not able to form enough molecular gas and therefore there's little to none CO emission

5.4.1 AVERAGED R_{21} FOR THE WHOLE CLOUD

In the previous section it was suggested that the biggest impact environment has on R_{21} is in the form of UV rays from the ISRF. We therefore plot the averaged value of R_{21} against the ISRF for all the clouds, our results are shown in Figure 5.3.

First thing to note is that the averaged value of R_{21} covers a range of values between 0.5 – 0.9, this confirms that changes in the cloud's environmental conditions do influence the overall value of R_{21} . Moreover, as seen in the previous section, an increasing ISRF is directly correlated with an increase in the average value of R_{21} . Additionally within each ISRF bin there is appreciable scatter, which can be attributed to the different changes in environmental conditions discussed in the previous section. However since the plot shows an averaged value for R_{21} , the specific changes in the distribution of R_{21} are reduced making it harder to distinguish between different environmental effects.

Extragalactic observations use R_{21} as a conversion factor rather than a diagnosing tool of GMC structure. In that context the averaged dashed line in Figure 5.3 represents the observationally derived and most commonly used value of R_{21} (Eckart et al., 1990; Casoli et al., 1991; Brand & Wouterloot, 1995; Sakamoto et al., 1997; Hasegawa, 1997; Sawada et al., 2001; Bigiel et al., 2008; Leroy et al., 2009; Barriault, Joncas & Plume, 2011). This line lies in the middle of the scatter of R_{21} values of our clouds, suggesting that $R_{21} \sim 0.7$ is a good first approximation for converting W_{21} into W_{10} . Nonetheless it questions the reliability and robustness of the conversion factor, as well as the potential errors in derived quantities such as the total molecular gas. We discuss the consequences and possible solutions in section 5.5.

It is important to note that the agreement between our simulations and the accepted value of R_{21} improves when considering higher sensitivity cuts to our detection limits. Our synthetic observations have an already low emission cut of 0.01 K km s^{-1} , as we increase the minimum detection limit the scatter is significantly reduced. When we impose a detection limit of 5 K km s^{-1} the scatter is almost completely gone. Considering that the emission from diffuse gas associated with lower line ratios is always very faint, it follows that $R_{21} \sim 0.7$ as sensitivity is reduced. This is a consequence of R_{21} being derived in a galactic context where clouds are well resolved and therefore sensitivity plays an important role.

5.4.2 CO EMISSION AS A PROBE OF PHYSICAL CONDITIONS

Naturally CO emission is directly correlated to the temperature of CO molecular gas within the cloud, however this is not necessarily the case for the temperature of H_2 gas where the bulk mass of the cloud is held. We explore whether CO emission, and more explicitly R_{21} , can accurately trace the gas temperature within GMCs. In order to compare to the averaged value of R_{21} calculated before, we define the average temperature as

$$\langle T \rangle = \frac{\sum_{i=1}^n m_i T_i \chi_i}{\sum_{i=1}^n m_i \chi_i} \quad (5.2)$$

where the sum is over all the SPH particles, m is the particle mass, T is the particle temperature and χ is the abundance of the molecule of interest. In this case we calculate the average temperature of H_2 (T_{H_2}) and of CO (T_{CO}). It is important to note that the T is the kinetic temperature of the gas obtained from the original SPH data that was the input for the radiative transfer.

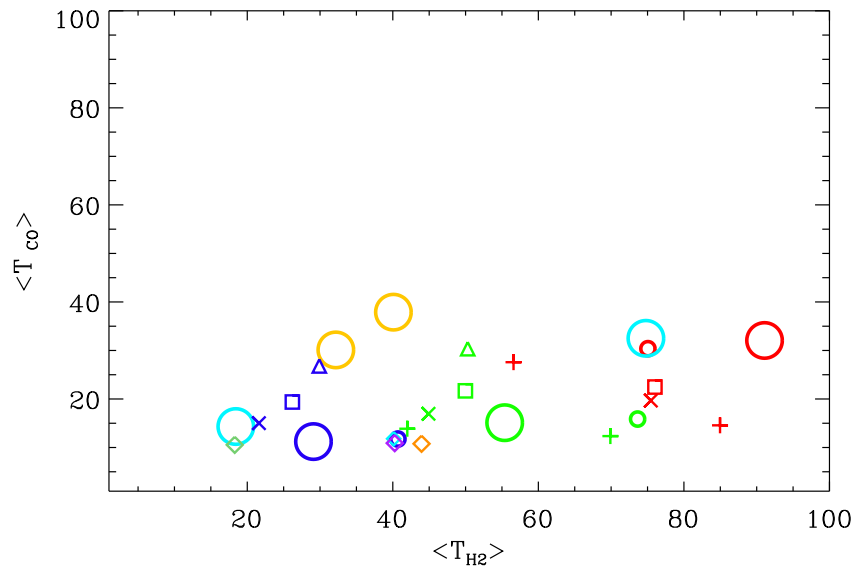


Figure 5.4. The average temperature of H_2 as calculated by equation 5.2 plotted against the average temperature of CO. Each point represents a cloud and have the same colour and shapes as in Figure 5.3

In Figure 5.4 we plot $\langle T_{H_2} \rangle$ vs $\langle T_{CO} \rangle$ where every point represents a cloud and have the same shape and colour as in Figure 5.3. First thing to note is that as the temperature of cloud increases as we increase the ISRF/CRIR, which is to be expected. However this increase in temperature is only reflected in $\langle T_{H_2} \rangle$ while CO gas never reaches temperatures above $T \sim 40$ K. As such the CO emission from the cloud is only tracing the temperature variations in CO gas while leaving the variations in the H_2 molecular gas untraced. This is easily understood since the bulk of the CO gas is within well-shielded regions where temperature of the gas is low and the densities are above n_{crit} . This is not the case for H_2 that is present in diffuser regions and at higher temperatures.

One notable exception is when considering the two CMZ clouds (yellow circles), in this case the T_{CO} and T_{H_2} are very similar. Since the initial density of these clouds is much higher, this results in most of the gas being well shielded and therefore at similar temperatures. Since the densities are high enough to excite CO then the CO emission is well correlated with the overall temperature of the gas. As it was mentioned in the previous section this is also reflected in the small variations of R_{21} .

5.4.3 ALTERNATIVE LINE RATIOS

Having created synthetic observations for the bottom three emission lines of CO's rotational ladder, it is a simple task to consider other ratios between these lines

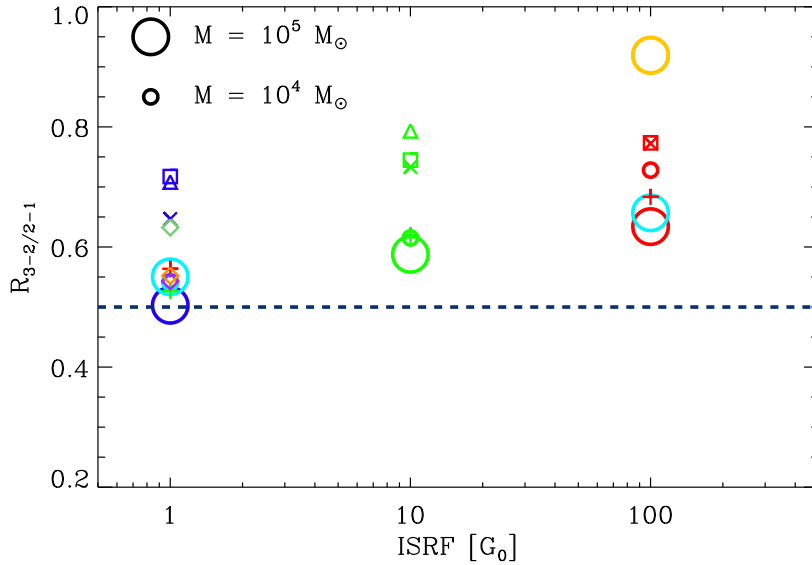


Figure 5.5. Similar to Figure 5.3 but for $J = 3 - 2$ and $J = 2 - 1$ rotational transition lines. Colour coding is the same as in Figure 5.3. The dashed line is the commonly used value for R_{32} (Vlahakis et al., 2013)

as possible conversion factors.

R_{32}

We first consider R_{32} , that is the ratio between the third ($J = 3 - 2$) and second ($J = 2 - 1$) rotational levels of CO. In order to judge how R_{32} varies we plot a similar figure to Figure 5.3, where we take the average intensities of each line for each cloud and then calculate the ratio. This is shown in Figure 5.5.

In this case the overall scatter is considerably larger than it was for R_{21} and our results are all above the accepted value of $R_{32} = 0.5$ (Vlahakis et al., 2013). At the same time R_{32} is also highly dependent on the changes in the ISRF as demonstrated by the increase in the averaged value of R_{32} with increasing ISRF. When looking at each of the clouds within each ISRF bin the spread seems to be correlated with the initial density of the simulations. Considering that the critical densities of $J = 2 - 1$ and $J = 3 - 2$ are of the same order of magnitude ($n_{\text{crit}} \sim 10^4$) then a larger fraction of R_{32} 's distribution will be originating from regions that are sub-critically excited i.e. $n < 10^4$ with lower initial densities. This explains why the value of R_{32} is larger for most of the GC16 clouds that have a slightly larger initial density.

Finally the CMZ-like clouds have a larger value of $R_{32} \sim 0.9$. Since the cloud starts with an initial density of $n = 10^4 \text{cm}^{-3}$, which is of the order of magnitude of the critical densities for both lines, this results in comparable emission from both

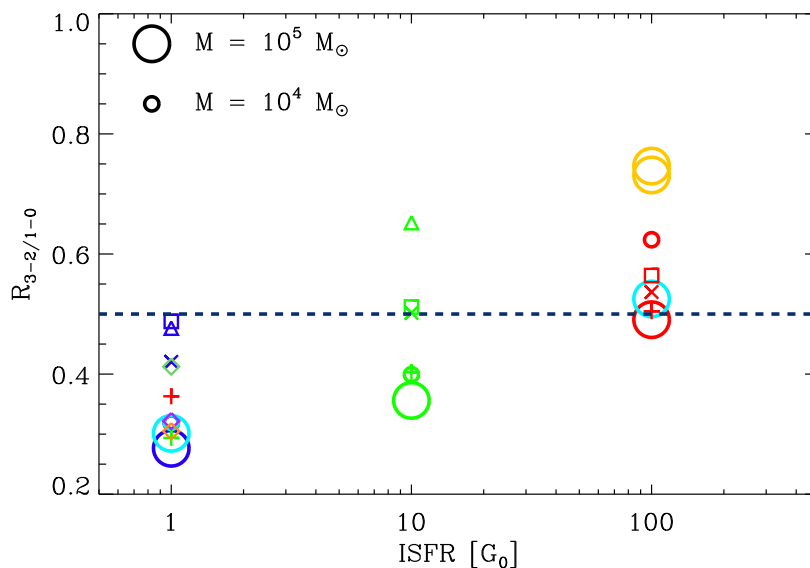


Figure 5.6. Similar to the top panel of Figure 5.3 but for $J = 3 - 2$ and $J = 1 - 0$ rotational transition lines. The dashed line represents the commonly used conversion factor for R_{31} (Aravena et al., 2014)

lines and therefore a ratio closer to unity.

R_{31}

In Figure 5.6 we look at the variations of the R_{31} , that is the ratio between CO's third ($J = 3 - 2$) and first ($J = 1 - 0$) rotational emission lines. The scatter for R_{31} is similar to R_{32} and we also see an increase in the average value with increasing ISRF. However the value of R_{31} is more evenly spread in each ISRF bin, suggesting that R_{31} is slightly more susceptible to changes of environment and initial conditions of GMCs.

The reason R_{31} has a higher variability is due to the considerable difference in excitation conditions for both lines. The critical density of the $J = 3 - 2$ emission line is $n_{\text{crit}} = 3.6 \times 10^4 \text{cm}^{-3}$ that is over an order of magnitude higher than the $J = 1 - 0$ line. Furthermore the difference in energy required to excite both lines is $\sim 27.7K$, which is quite significant when considering the low temperature environments of dense regions within GMCs. This explains why at lower ISRF R_{31} is much lower, since a significant amount of emission is arising from diffuse regions where the $J = 1 - 0$ line is easily excited but $J = 3 - 2$ is not. On the other hand at high ISRF both lines will be excited and emitting from dense regions, since most of the diffuse gas has been dissociated this eliminates the excess emission from $J = 1 - 0$ therefore increasing the value of R_{31} .

R_{31} is usually taken to be $R_{31} = 0.5 \pm 0.2$. Our results show that the scatter of the average value for different clouds is just over the expected error for R_{31} . However the results shown in Figure 5.6 also suggest that using $R_{31} = 0.5$ can considerably underestimate or overestimate the amount of emission associated with W_{10} and therefore any derived quantities or properties of the studied source. At the same time this suggests that if the value of the ISRF is known a better constrained conversion factor with a smaller error can be used. We shall explore this in the following section.

5.5 DISCUSSION

5.5.1 X_{CO} ON UNRESOLVED CLOUDS

The results presented in Section 5.3 show the dependence different line ratios have from the environment surrounding the cloud. At a galactic level where clouds can be highly resolved, line ratios can serve as a probe of the physical conditions of the cloud. When looking at unresolved clouds, these variations are still present and question the accuracy and robustness of such conversion factors. We therefore explore whether these small variations to R_{21} and R_{31} can have an impact when trying to derive physical properties.

We rely on conversion factors such as R_{21} and X_{CO} to estimate the total molecular gas within GMCs or indeed entire galaxies. The total column density of H_2 is often calculated by

$$N_{\text{H}_2} = \frac{X_{\text{CO}} W_{21}}{R_{21}}. \quad (5.3)$$

We therefore want to compare N_{obs} as calculated by Equation 5.3 with N_{real} , where we take N_{real} to be the column density of H_2 directly from the GADGET-2 snapshot.

Before doing so we reproduce Figure 4 from Clark & Glover (2015) where they plotted the value of X_{CO} for each cloud against the the 'star formation rate', which is a proxy for changes in the ISRF and CRIR. In this case we plot against the ISRF as well as include additional clouds that where not studied in Clark & Glover (2015)(See Figure 5.7). Additionally we have only included clouds with $Z = Z_{\odot}$, since X_{CO} is empirically derived from observations within the Milky Way and therefore intrinsically assumes a solar-like metallicity. It is important to note that this plot may look slightly different from Figure 4 of Clark & Glover (2015). This is because in the radiative transfer in this study includes the refinement routine and the Sobolev-Gnedin approximation described in Chapter 3. When compared, the results presented

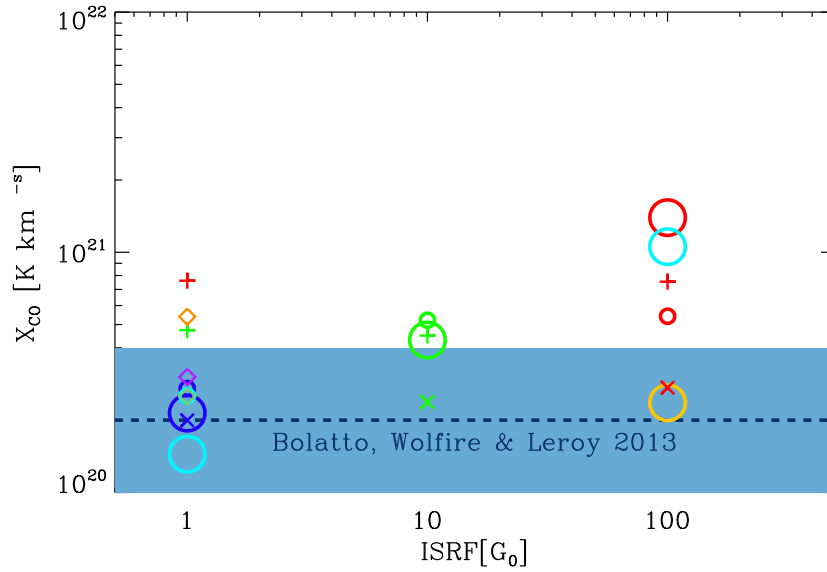


Figure 5.7. X_{CO} plotted against ISRF for all the clouds using the same labels as in Figure 5.3. The line represents the typical value for X_{CO} and the shaded region the scatter as given by Bolatto, Wolfire & Leroy (2013). Note that clouds with metallicities of $Z \neq Z_{\odot}$ are not included

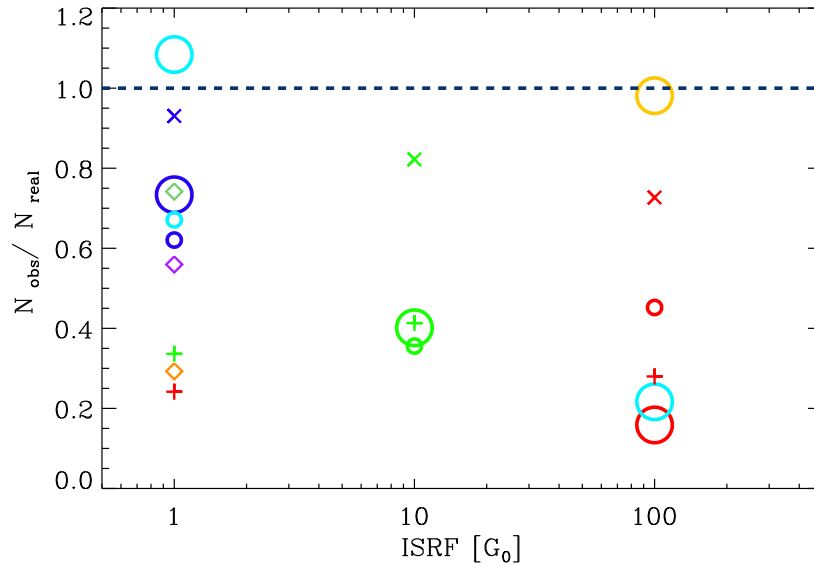


Figure 5.8. Shows the ratio of $N_{\text{obs}}/N_{\text{real}}$ against ISRF for all the clouds using the same labels as in Figure 5.3, where N_{obs} is calculated using R_{21} . Note that clouds with metallicities of $Z \neq Z_{\odot}$ are not included

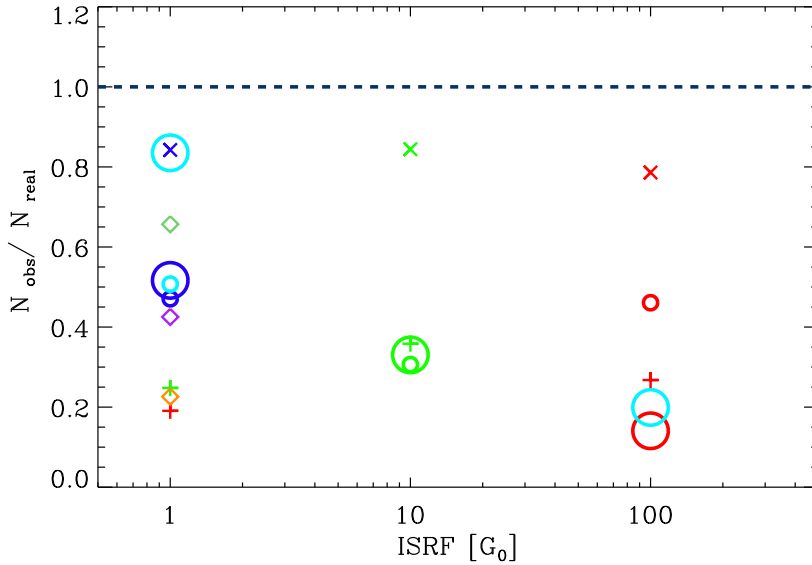


Figure 5.9. Similar to Figure 5.8 but using R_{31} instead of R_{21}

here systematically lower the value of X_{CO} making these results closer to the typically used value.

In Figure 5.8 the ratio of $N_{\text{obs}}/N_{\text{real}}$ against the ISRF is plotted. When calculating N_{obs} we have used the $X_{\text{CO}} = 2 \times 10^{20} \text{ cm}^{-2} \text{ K km s}^{-1}$ as given by Bolatto, Wolfire & Leroy (2013) and $R_{21} = 0.7$. From this figure it becomes evident that the amount of molecular gas estimated from W_{21} can be easily underestimated. This can be understood when comparing with Figure 5.7 where at high ISRF the standard value of X_{CO} will underestimate the total column of H_2 . On the other hand Figure 5.3 shows that using an average value of $R_{21} = 0.7$ will overestimate the amount of W_{10} at high ISRF. Effectively this compensates the existing biases of both conversion factors to some extent, however this is not enough to avoid underestimating the amount of H_2 due to the high errors in X_{CO} . This is also the case for the green and red plus signs at $\text{ISRF} = 1$, they correspond to the high CRIR runs, where X_{CO} is also underestimated.

At lower ISRF the discrepancies between N_{obs} and N_{real} arise from R_{21} , since at lower ISRF X_{CO} is well within the accepted value. From Figure 5.3 we can see that using $R_{21} = 0.7$ effectively underestimates the amount of W_{10} and therefore the total column density of H_2 . This effect is even stronger when using R_{31} instead of R_{21} , which is seen in Figure 5.9 where we use $R_{31} = 0.5$ to calculate N_{obs} .

What is important to note is that variations in the line ratios, even small ones, can have a direct impact on the derived physical properties of the system, specially at low radiation fields. Moreover these variations need to be properly quantified and

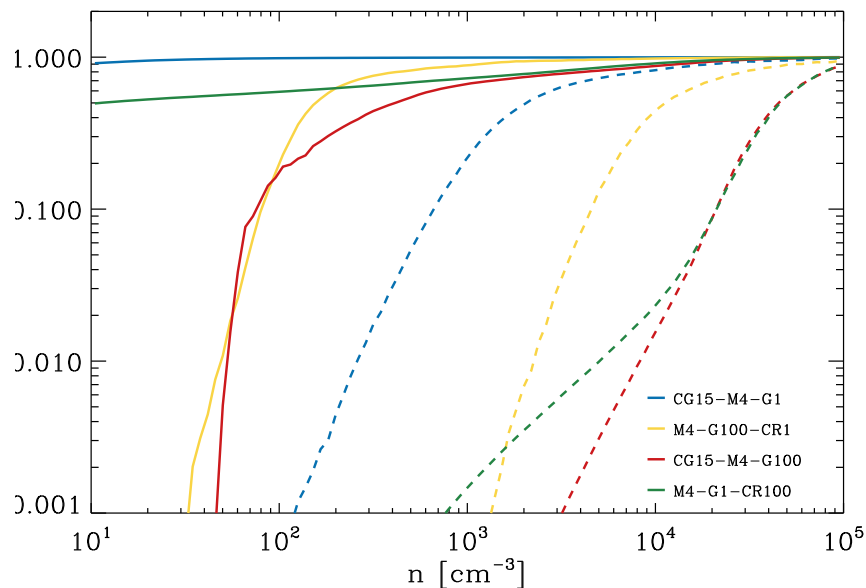


Figure 5.10. Each coloured line represent a different simulation. Solid lines track the H_2 fractional abundance as a function of the number density of the gas. Dashed lines track the same behaviour but for CO

taken into account as intrinsic uncertainties, leading to a more accurate results and therefore a better understanding of star formation in unresolved systems.

5.5.2 R_{21} AS A PROBE OF CO ABUNDANCE

As discussed in Section 6.4, variations in the strength of the ISRF and the CRIR affect R_{21} in different ways. In this section we further explore why this is and more importantly whether this change in R_{21} is probing changes in the abundance of molecular gas.

Since we are interested in quantifying the effect of the ISRF and the CRIR on the state and abundance of molecular gas we will focus on the following 4 clouds CG15-M4-G1, M4-G1-CR100, M4-G100-CR1 and CG15-M4-G100. We then plot the fractional abundance of CO and H_2 as a function of the average number density of the gas for each cloud. This is shown in Figure 5.10, where the solid lines represent the H_2 abundance fraction and the dashed line CO abundance fraction.

First thing to note is that the H_2 abundance fraction only changes when the ISRF changes, while changes to the CRIR make a very small impact. Given the chemical model included in these simulations, we know that UV rays are needed to effectively dissociate H_2 . Even though cosmic rays can dissociate some H_2 , when considering other chemical reactions the net effect leaves the total abundance of H_2

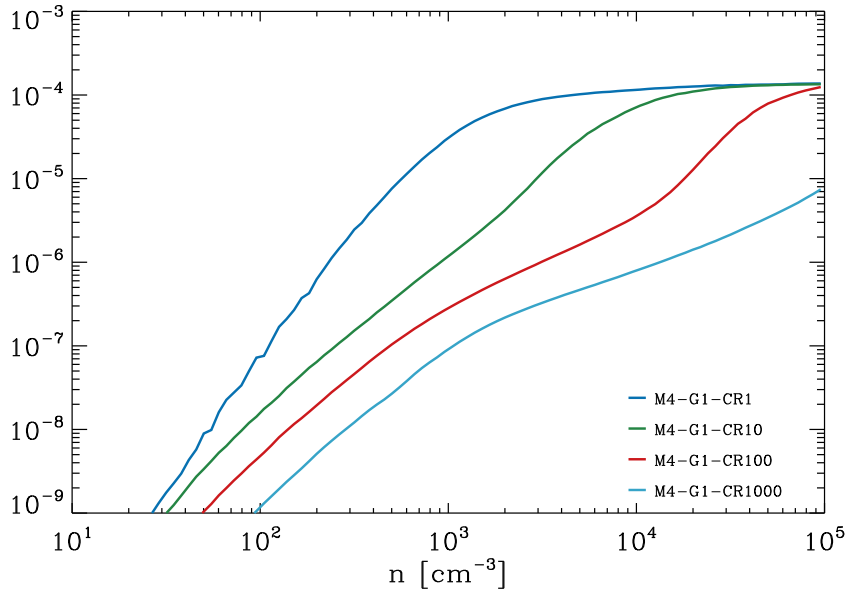
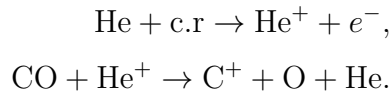


Figure 5.11. Illustrates how CO/H₂ abundance ratio changes with average number density.

unchanged (Glover & Clark, 2012a). On the other hand cosmic rays can be very effective at reducing the total fraction of CO and can be seen when comparing the CO abundance of M4-G1-CR100 and M4-G100-CR1. The reason for this becomes evident when looking at the following chemical reactions



When looking at the cloud with high ISRF the fraction of CO abundance (dashed yellow line) increases quickly, this is because once the CO is well shielded the production of CO is very quick. As a result the emission coming from these high density regions will be bright and well correlated with high values of R_{21} . On the other hand when looking at the high CRIR cloud the fraction of CO abundance (dashed green line) starts increasing at similar number densities ($\sim 10^3 \text{ cm}^{-3}$) however at a much slower rate. This is because the CO production is being constantly hampered by the cosmic rays which are not attenuated. As such the emission from these regions will be faint due to the low abundance of CO, more importantly R_{21} will have values around ~ 0.3 .

A recent paper by Bisbas et al. (2017) studied how increasing the CRIR can be important in destroying CO. In Figure 11 of this paper they compare the CO/H₂

fraction as a function of number density, for varying CRIR. We reproduce this figure with our own set of simulations for which the CRIR is increased in the same way (Note to better compare to their results we ran an additional simulation with $\zeta_{\text{H}} = 3 \times 10^{-14} \text{ s}^{-1}$ that was not included in our initial setup). Our results show a similar trend where the CO/H₂ abundance ratio decreases with increasing CRIR.

The effect of CRIR on the abundance of CO will have a direct impact on the CO emission and therefore how much molecular gas can be traced within GMCs. Even though the total CO emission is reduced, our synthetic observations show that the changes in abundances seen above can be traced to some extent when looking at the resolved integrated intensities and R_{21} of these clouds (See Figure 5.2). One caveat to keep in mind when considering these results, is that our models have a constant CRIR throughout the whole cloud. Meaning cosmic rays are in no way attenuated and therefore able to reach the densest regions of the cloud. Whether this is an accurate approximation is beyond the scope of this study and therefore the reader should keep this in mind when looking at these results.

5.6 CONCLUSIONS

We have studied a range of numerically modelled molecular clouds where the initial parameters were systematically varied. Then we take the snapshot just before the first cores form and performed radiative transfer simulations to create synthetic CO line emissions for all clouds. We use these synthetic observations to study the impact of environment on CO line emission and CO line ratios. Our main findings can be summarised as follows:

1. The value of R_{21} and its correlation with dense/cold and warm/diffuse gas is key when understanding the state of the gas within GMCs. Because of this correlation, changes in the initial and environmental conditions directly relate to variations in R_{21} and can be traced back to changes in the properties of the gas within GMCs. From all the environmental changes studied, variations in the ISRF and the CRIR have the largest impact on the average value and the cumulative PDF of R_{21} .
2. The dependance of different line ratios (R_{21} , R_{32} and R_{31}) on environment can still be observed when looking at unresolved clouds where the total emission is averaged. Our results suggest that the accepted values for R_{21} and R_{31} are a good first approximation. At the same time the scatter around the accepted

value ($\sim \pm 0.2$) suggests that careful consideration should be had when using them as conversion factors, specially given the high dependence on the ISRF.

3. When calculating the column density of H₂ molecular gas of GMCs it is important to consider the biases of X_{CO} and line ratios R_{21} and R_{31} . At a high ISRF ($G_0 = 100$) X_{CO} will underestimate the N_{H_2} . This is only slightly compensated by the bias line ratios have at high ISRF. On the other hand since at low ISRF ($G_0 = 1$) X_{CO} is well constrained, the errors in N_{H_2} come from line ratios underestimating the total amount of emission from the $J = 1 - 0$ transition line.
4. Cosmic rays can help regulate the total CO abundance within GMCs. When $\zeta_{\text{H}} = 3 \times 10^{-17} \text{ s}^{-1}$ the CO to H₂ abundance ratio is $\sim 10^{-4}$ at densities of $\sim 10^3 \text{ cm}^{-3}$. As ζ_{H} is increased the CO to H₂ fraction is considerably reduced reaching values of only $\sim 10^{-5}$ at densities of $\sim 10^5 \text{ cm}^{-3}$ for $\zeta_{\text{H}} = 3 \times 10^{-17} \text{ s}^{-1}$. This has a direct impact on the CO emission and on the average value and distribution of R_{21}

CHAPTER 6

CAN THE VIRIAL PARAMETER RELIABLY TRACE THE DYNAMICAL STATE OF MOLECULAR CLOUDS?

6.1 INTRODUCTION

One of the underlying assumptions in star formation is that stars form in long lived, bound gas entities called giant molecular clouds (GMCs). This paradigm is rooted in the fact that most of the molecular gas contained within GMCs will eventually collapse into stars (Klessen & Glover, 2016). Moreover there has been observational evidence that supports the idea that, for the most part, GMCs are gravitationally bound (Zuckerman & Evans, 1974; Solomon et al., 1987). This evidence is based on the study of the virial parameter (α), that is the ratio of the gravitational energy and the turbulent kinetic energy of the cloud. α is normally defined as,

$$\alpha_{\text{vir}} = \frac{5\sigma^2 R}{GM}, \quad (6.1)$$

where σ is the one-dimensional velocity dispersion, R is the radius and M is the mass of the observed cloud (Bertoldi & McKee, 1992). Even though this is a one-dimensional, observationally motivated approximation of a more general theorem, it can nonetheless help to simply and effectively assess the dynamical state of clouds. However, it is still very much an open question whether these observationally derived values of α are in fact representative of the true dynamical state of the cloud.

Consequently there has been considerable research, both observationally and

numerically, on the topic of the virial parameter and whether the nature of GMCs is a bound or unbound one (Hartmann, Ballesteros-Paredes & Bergin, 2001; Elmegreen, 2007; Ballesteros-Paredes et al., 2007; Ballesteros-Paredes, 2006; Dib et al., 2007; Shetty et al., 2010; Dobbs, Burkert & Pringle, 2011). Nonetheless, there is still a very real disconnect between observations and simulations, making comparisons between results difficult and not always accurate. It is only recently, with the growing interest in synthetic observations that we can start bridging this gap. A way of doing so is by testing the accuracy, uncertainties and biases of the observational methods, in this case of Equation 6.1.

Bearing this in mind, we intend to study, through the use of synthetic observations of ^{12}CO , how accurate the observationally derived virial parameter is at gauging the ‘true’* dynamical state of the cloud. Since Equation 6.1 is dependant on σ , R and M , we also study how definitions and therefore estimates of these values change from a numerical to an observational perspective as well as how they impact the overall value of the virial parameter. To do so we use smooth particle hydrodynamics (SPH) simulations with time-dependent chemistry to follow the evolution of clouds, in which metallicity is systematically varied, and can then be post-processed into synthetic observations. Varying metallicities have been shown to delay the formation of molecular hydrogen (H_2) and carbon monoxide (CO) (Glover & Clark, 2016). This can be important for the study of α in GMCs due to the fact that we rely on molecular line emission to trace the mass and size of the cloud. Moreover there has been recent evidence that CO linewidths decrease with metallicity (Private correspondence with Jonathan Braine) and therefore the velocity dispersion of the cloud.

The structure of this Chapter goes as follows. In Section 6.2 we describe the setup of the numerical simulations and the modelling of synthetic observations. In Section 6.3 We highlight the different methods used to calculate the different values for σ , M , R and α , both for numerical simulations and synthetic observations. In Section 6.4 we examine how the accurate different methods are and highlight possible biases and uncertainties. We also studying the impact these variations have on the virial parameter and its assessment of the cloud’s dynamical state. In Section 6.5 we discuss some possible caveats and limitations of our results. Finally in Section 6.6 we summarize our findings.

*From this point on, unless stated otherwise, we refer to ‘true’ as the ideal value for comparison that is calculated from the numerical simulations and compared with our synthetic observations

6.2 METHOD

With the aim of testing how the observed velocity dispersion varies with metallicity we model three different clouds at solar, large magellanic cloud (LMC) and small magellanic cloud (SMC) metallicities. We make use of previously modelled clouds and refer the reader to Glover & Clark (2016) for a detailed description of the initial conditions. The synthetic observations are produced using RADMC-3D. We make use of the refinement routine described in Peñaloza et al. (2017) and the Sobolev-Gnedin approximation described in Peñaloza et al. (2018).

6.3 NUMERICAL AND OBSERVATIONAL TECHNIQUES

It is important to clarify and clearly state what the different analysis techniques are in order to avoid confusion. Doing so, will be helpful to properly understand what the different biases, limitations and uncertainties in these methods are and where do they come from. In this Section we focus on describing these techniques.

6.3.1 VELOCITY DISPERSION

The velocity dispersion acts as a proxy of the kinetic energy of the cloud. The higher the velocity dispersion the more turbulent the cloud and likely it is to be easily dispersed. The one dimensional velocity dispersion for any given orientation is given by

$$\sigma_j^2 = \frac{\sum_i^N \mu_i (v_{ij} - \langle v_j \rangle)^2}{\sum_i^N \mu_i}, \quad (6.2)$$

where $j = x, y$ or z are the spatial orientations, μ_i is an arbitrary weight, v_{ij} the velocity of each element, $\langle v_j \rangle$ the average weighted centre of velocity and the sum is over all pixels when considering observations and all particles when considering simulations. Note that v_{ij} is dependent on the choice of μ_i .

Simulation

Numerical simulations contain a wealth of information that is not normally available to observers. As such the velocity dispersion can be calculated in several different ways.

First we can consider the full 3D velocity dispersion i.e. $\sigma_{\text{Gas}} = \sqrt{\sigma_x^2 + \sigma_y^2 + \sigma_z^2}$, where we have used $\mu_i = m_i$. This will be the most accurate description of the velocity field of the cloud since we consider perturbations in every orientation. Keeping in mind that the metallicity of these clouds is changing, this will result in the dynamics of the atomic gas becoming more important at lower metallicities. Conversely observers only have access to the dynamics as traced by the molecular gas. Therefore the velocity dispersion of σ_{CO} or σ_{H_2} , where we use $\mu_i = m_i \chi_{\text{CO}}$ and $\mu_i = m_i \chi_{\text{H}_2}$ respectively, could either be considered as the ‘true’ σ and a better comparison with observations.

Alternatively, observers only have access to the velocity dispersion along the line of site. In this case that is the z -axis. Therefore we can also take $\sigma_{z\text{Gas}}$, $\sigma_{z\text{CO}}$ or $\sigma_{z\text{H}_2}$.

Observation

Unfortunately from an observational perspective all the velocity information is encoded within the line-width of the spectra and therefore only contains velocity information of one spatial component. Moreover the velocity dispersion obtained from the line-width has both a thermal and a non-thermal component. Keeping this in mind we use Equation 6.2 to calculate σ_{obs} , using $\mu_i = T_{\text{B},i}$ where $T_{\text{B},i}$ is the brightness temperature in each velocity channel.

6.3.2 RADIUS

The asymmetrical nature of GMCs and its varied shapes, sometimes due to projection effects, means the radius to size relationship is not always straightforward. More importantly, as we shall see, the virial parameter can be affected by slight variations in the radius. Analogous to the velocity dispersion we can compute the characteristic radius of the cloud by

$$R_j = \sqrt{\frac{\sum_i^N \mu_i (R_{ij} - \langle R_j \rangle)^2}{\sum_i^N \mu_i}}, \quad (6.3)$$

where $j = x$ or y since we consider a projected image.

Simulation

The mass weighted radius can be calculated from the total column density of the gas (N_{gas}) where $R_{\text{Gas}} = \sqrt{R_x^2 + R_y^2}$ and we use $\mu_i = N_{\text{Gas},i}$. Similarly to σ , we can consider the radius from just the molecular gas. We then compute R_{CO} and R_{H_2} from N_{CO} and N_{H_2} respectively.

Observation

For the synthetic observations we calculated the characteristic radius weighted by intensity ($R_{T_B,i}$) from Equation 6.3. Alternatively, an equivalent radius can be calculated from the total area given by

$$A = \sum_i N_i dx dy, \quad (6.4)$$

where N_i are the number of pixels above $> 1\text{K}$, dx and dy are the height and width of each pixel. Then assuming that A corresponds to the area of a circle it then follows that

$$R_A = \sqrt{\frac{A}{\pi}}. \quad (6.5)$$

Naturally the more spherically symmetric the source is the better this assumption would do at estimating the radius of the cloud.

6.3.3 MASS

Simulation

Since mass is a conservative property then the total mass is set by the initial conditions of the simulation in itself. Nonetheless, in the same manner as above we can calculate the total mass of a certain molecule, in our case CO and H₂. Calculating this Mass is a straight-forward sum over all the particles multiplied times the abundant fraction of that given molecule.

Observation

Observationally mass cannot be detected only derived. In this case we will assume that mass is derived from CO emission only, however we note that this is not the only nor necessarily the most accurate way of doing so. Traditionally mass is given by

$$M = L_{\text{CO}} X_{\text{aCO}} \quad (6.6)$$

where L_{CO} is the surface integrated intensity of the source given in $[\text{K km pc}^2 \text{ s}^{-1}]$ and α_{CO} is the conversion factor from CO to total molecular gas (Bolatto, Wolfire & Leroy, 2013). Note that $L_{\text{CO}} = W_{\text{CO}}/A$, where A is the area of the image or beam.

To convert from CO to H_2 gas the conversion factor is taken to be $X_{\alpha\text{CO}} = 4.35 [M_{\odot} \text{ pc}^{-2} (\text{K km s}^{-1})^{-1}]$. However this value has been derived for Milky-Way-like environments and metallicities. Revised values for $X_{\alpha\text{CO}}$ as a function of metallicity are given by Bolatto, Wolfire & Leroy (2013). Consequently we could derive different masses depending on what value we adopt a single value for $X_{\alpha\text{CO}}$ or a revised one accounting for changes in metallicity. Note that in Bolatto, Wolfire & Leroy (2013) and other papers, the conversion factor is traditionally labelled as α_{CO} but we have renamed it here to avoid confusion in our analysis with the virial parameter α .

6.3.4 VIRIAL PARAMETER

The virial parameter (α_{vir}) describes the dynamical state of a cloud by comparing the gravitational energy with the kinetic (turbulent) energy. As mentioned previously this makes it one of the most used quantities to describe and compare astrophysical systems.

Simulation

From the GADGET-2 snapshot we can access all the details regarding position, velocity and mass of the SPH particles that make up the cloud. After finding the centre of mass we can calculate the gravitational energy by

$$E_g = \sum_i \frac{5GM_{\text{enc},i}m_i}{3R_{\text{COM},i}} \quad (6.7)$$

where $R_{\text{COM},i}$ is the radius to the centre of mass, m_i is the mass of the particle and $M_{\text{enc},i}$ is the enclosed mass at that radius. The kinetic energy can be trivially calculated by $E_k = \sum_i m_i v_i^2 / 2$, where the sum is over all SPH particles.

Then the virial parameter will be given by $\alpha_{\text{Gas}} = 2E_{\text{kin}}/E_{\text{pot}}$. In addition we can calculate the virial parameter for only CO, by calculating E_g and E_k with mass is given by $m_i \chi_{\text{CO}}$. Similarly we can do the same for H_2 .

Observation

Since there is no way of directly measuring the gravitational or kinetic energy, the virial parameter is observationally defined by Equation 6.1. As we have described

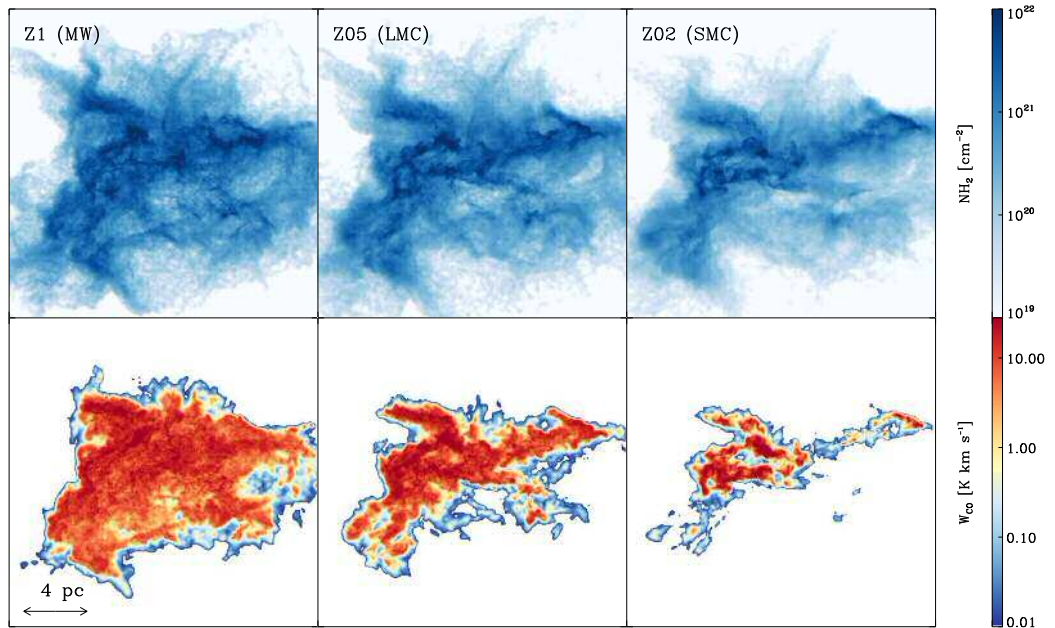


Figure 6.1. Top row: H_2 Column densities for GMCs with metallicities of $Z = Z_\odot$, $Z = 0.5Z_\odot$ and $Z = 0.2Z_\odot$ from left to right. Bottom row: Integrated intensities of the first rotational transition line of ^{12}CO for each cloud.

above there are different ways to observationally calculate each of the quantities comprising Equation 6.1. As we shall see they have a direct impact on the derived virial parameter and therefore our interpretations of the dynamical state of the system.

Simulation and Observation

Equation 6.1 is defined observationally, however as previously mentioned σ , R and M can all be calculated from the simulation. Thereby we can calculate an observationally motivated virial parameter while using quantities derived from simulations. We shall explore in the next Section whether this is an indeed useful exercise or even physically meaningful as a result.

6.4 RESULTS

The first row of Figure 6.1 shows the column density of H_2 for the each cloud at a different metallicity. It is clear that the general structure of the cloud is preserved regardless of the metal content. Small differences start to show at the edge of the cloud towards more diffuse regions where at lower metallicities less H_2 is formed

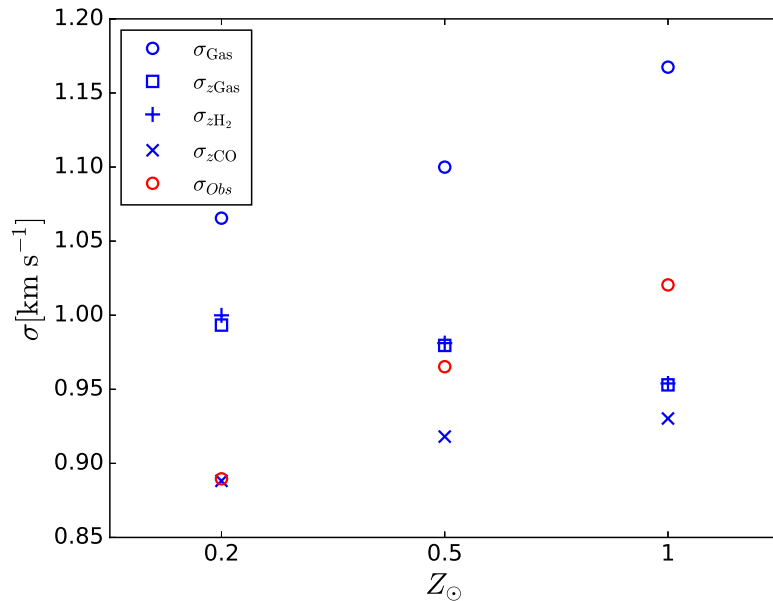


Figure 6.2. Figure showing how σ changes as a function of metallicity. Blue symbols represent quantities calculated from simulations while red symbols are calculated from synthetic observations.

given the reduced shielding capacity of the gas. The bottom row shows the synthetic observations for the first rotational transition line of ^{12}CO . In this case, the size and total brightness of the cloud is considerably reduced towards lower metallicities.

Simply comparing the top and bottom row of Figure 6.1 highlights the differences between a numerical simulation perspective and an observational one. Note that even though these are “ideal” synthetic observations they are enough to stress the contrast between both pictures and the importance in understanding their limitations. It is therefore important to quantify these differences. To do so we shall look at how the velocity dispersion (σ), the radius (R) and the mass (M), vary between a numerical and observational perspective by using the different methods described in the previous Section.

6.4.1 σ , M AND R

Each panel of Figure 6.2 shows σ , M and R as a function of metallicity. Where each symbol represents a different way of calculating either σ , M or R as described in the previous section. Blue and red symbols distinguish whether the value was calculated from the GADGET-2 snapshot or from the synthetic observations produced with RADMC-3D.

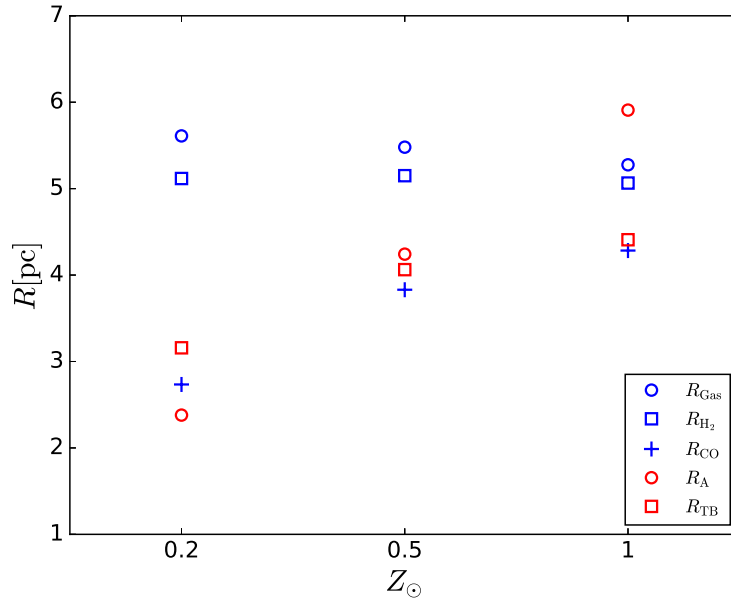


Figure 6.3. Figure showing how R changes as a function of metallicity. Blue symbols represent quantities calculated from simulations while red symbols are calculated from synthetic observations.

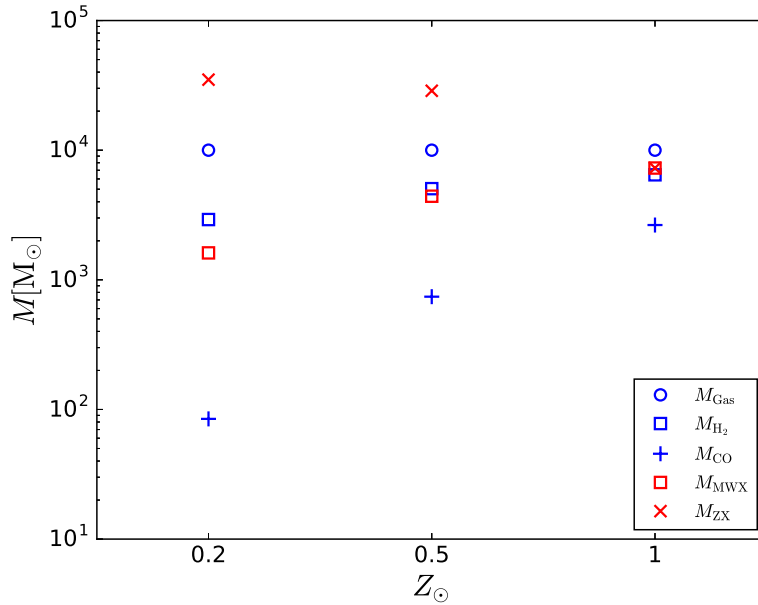


Figure 6.4. Figure showing how σ as a function of metallicity. Blue symbols represent quantities calculated from simulations while red symbols are calculated from synthetic observations.

Velocity Dispersion

In the top panel of Figure 6.2 the velocity dispersion as a function of metallicity is shown. First thing to note is the difference between the blue circles (σ_{Gas}) and blue squares ($\sigma_{z\text{Gas}}$). Having a larger velocity dispersion when considering the 3D structure of the cloud suggests that the turbulent field is not isotropic. This is also highlighted by the fact that $\sigma_{z\text{Gas}}$ slightly decreases with increasing metallicity while σ_{Gas} considerably increases with metallicity. This difference may be reflected in the total kinetic energy of the cloud thereby leading to an inaccurate calculation of the virial state of the cloud.

One possible explanation for the change in σ is given by the set-up of our clouds, where each cloud is allowed to evolve until the onset of star formation is triggered. The lower the metallicity the longer the cloud is allowed to evolve since it takes longer to form molecular gas, thereby leading to a delay on star formation and longer running times. Since turbulence is left to decay it means that, for clouds with lower metallicity, the turbulent field has been allowed to decay for longer and therefore the anisotropic differences reduced. An alternative explanation comes from the fact that lower metallicity clouds have a smaller shielding factor and therefore contain warmer gas. This means that the sound speed of the gas is larger which leads to higher Mach numbers and more violent shocks that effectively transform the turbulent kinetic energy into high density regions.

Comparing $\sigma_{z\text{Gas}}$, $\sigma_{z\text{H}_2}$ and $\sigma_{z\text{CO}}$ highlights how the velocity field and therefore the dynamical structure of the cloud changes when considering different components of the gas. $\sigma_{z\text{Gas}}$ and $\sigma_{z\text{H}_2}$ yield very similar dispersions where differences are marginally higher as metallicity decreases. When considering $\sigma_{z\text{H}_2}$ part of the velocity field will be contained in atomic gas and therefore will be unmeasured. Since lower metallicities imply a smaller fraction of the atomic gas is converted into molecular gas, it follows that the difference between $\sigma_{z\text{Gas}}$ and $\sigma_{z\text{H}_2}$ will increase as metallicity decreases. Additionally, both exhibit a slight decrease ($\Delta\sigma < 0.05 \text{ km s}^{-1}$) in velocity dispersion as metallicity increases. However, since $\Delta\sigma$ is so small we consider this to be a consequence of the random turbulent seed rather than an overall trend. Lastly, $\sigma_{z\text{CO}}$ yields a considerable smaller velocity dispersion ranging from $\Delta\sigma \sim 0.05 \text{ km s}^{-1}$ at $Z_{\odot} = 1$ to $\Delta\sigma < 0.1 \text{ km s}^{-1}$ at $Z_{\odot} = 0.2$. Glover & Clark (2016) showed that CO only forms in dense cores at lower metallicities, meaning that $\sigma_{z\text{CO}}$ will trace considerably less of the velocity field in the diffuse gas as metallicity decreases.

Finally we consider σ_{Obs} , that is the observed line-width of our synthetic observations that is calculated using Eq. 6.2. First thing to note is that σ_{Obs} , as opposed

to the previously considered σ , contains a thermal component emerging from the post process radiative transfer performed on the SPH data. Keeping this in mind, σ_{Obs} clearly decreases as metallicity decreases which follows from the qualitative description of Figure 6.1. Considering that σ_{Obs} is derived from the emission of the first rotational line of CO, it is reasonable to expect that σ_{Obs} has a similar behaviour to $\sigma_{z\text{CO}}$. As it can be seen σ_{Obs} is not simply compared to its numerical counterparts and whether $\sigma_{z\text{CO}}$ is the ‘true’ velocity dispersion remains to be seen. For now we delay this discussion for Section 6.5.

Radius

The middle panel of Figure 6.2 plots the radius of the cloud as a function of metallicity. First we examine R_{Gas} , R_{H_2} and R_{CO} . As expected the apparent size of the cloud decreases when considering N_{Gas} , N_{H_2} and N_{CO} respectively. This reflects the ideal and common description of an onion-layered GMC, where you have an outer layer of diffuse ionized gas followed by layers of molecular gas (See Figure 8, Bolatto, Wolfire & Leroy 2013). Moreover as seen in this Figure, when the metallicity decreases the central molecular layers become smaller and eventually non-existent. This is also reflected in our results as the differences between R_{Gas} , R_{H_2} and R_{CO} become considerably larger as metallicity decreases. One further thing to note is that R_{Gas} slightly increases as metallicity decreases. Since a larger fraction of the gas will be unshielded and therefore warmer, this delays the collapse of the cloud and yielding a larger radius, albeit of diffuse atomic gas.

R_{A} and R_{Tb} represent the radius of the cloud from an observational perspective. R_{A} is highly dependent on the geometry of the cloud and therefore what is seen here is a measure of the change in the total brightness of the cloud. That is, as the metallicity decreases there is less CO and therefore significantly less emission which is reflected in the radius. More importantly since this is a simple sum, the radius does not plateau like it does for R_{Tb} . On the other hand R_{Tb} and R_{CO} are quite similar which is to be expected. First the $J = 1 - 0$ transition line directly traces the CO molecular gas, even when accounting for the different radiative transfer effects. Second, intensity could be considered a reasonable first approximation to mass, making the overall effect of a different μ_i for Equation 6.3 minimal.

Finally it should be said that there is no ‘true’ radius to which we can compare and assess the accuracy of the different methods. Each R_i represent a measure of what a cloud is defined to be and as such each has its own validity when applied correctly. This is only to say that it is important to consider what is exactly being measured and

why when making statements about the dynamics and properties of what we define as clouds. We shall explore this further when we look at how different R s affect the virial parameter and in Section 6.5.

Mass

Finally the bottom panel of Figure 6.2 has the Mass of the cloud as a function of metallicity. From a numerical standpoint obtaining the mass is somewhat intuitive since it is only a fraction of the total gas content, where no other uncertain effects, such as optical effects, have to be factored in. As such, results for M_{Gas} , M_{H_2} and M_{CO} are straight-forward to interpret, since they just highlight the effect metallicity has on the production of molecular gas. This has been already studied in detail by many authors (Glover & Clark, 2016).

On the other hand, obtaining a measure of mass observationally relies on considerable intrinsic assumptions and arguably is where a lot of the uncertainty arises. In this case we consider how mass is derived from CO emission. From equation 6.6 it is clear that the accuracy on M is dependant on, how well correlated is CO intensity to CO mass and CO mass to H_2 mass. Therefore observationally derived values of mass could be considered more accurate the closer they are to M_{H_2} .

From the bottom panel of Figure 6.2 we can see that M_{MWX} is fairly similar to M_{H_2} while M_{ZX} does a poorer job as metallicity decreases. This is highly unexpected since M_{ZX} makes use of a conversion factor that is intended to account for changes in metallicity. This would suggest that conversion from CO mass to H_2 mass is invariant with respect to metallicity, however we can confidently say this is not the case since we see that the difference between M_{H_2} and M_{CO} is not constant. The effect here is a more subtle one and relies on the fact that CO's first rotational transition line becomes bright very quickly once $\tau > 1$. As such, the decrease in intensity is not proportional to the decrease in mass as metallicity decreases and tends to overestimate M_{CO} . However, by using a the standard Milky Way conversion factor, which naturally underestimates the amount of H_2 gas at $Z = Z_{\odot}$ (Clark & Glover, 2015), the value of M_{MWX} then approaches M_{H_2} .

Surprisingly, our results here suggest that it is more accurate to use the Milky Way value of $X_{\alpha\text{CO}}$ when calculating M_{H_2} . This is because the uncertainties and biases of L_{CO} in Equation 6.6 seem to naturally compensate the changes in metallicity. Whether there is a correlation between how L_{CO} and $X_{\alpha\text{CO}}$ change with metallicity remains to be seen.

6.4.2 α VARIABILITY

As mentioned before the virial parameter is a well defined number that describes the interplay between gravitational energy and turbulent kinetic energy. The value for the virial parameter is a simple and effective manner of quantifying the dynamical state of the cloud and therefore predict its evolution. As mentioned in the previous Section how we calculate and define α differs from a numerical and observational perspective. In Figure 6.5 we show how the final value of α changes depending on the method used.

First thing to note are the values of importance when considering the virial parameter. Namely when $\alpha < 1$ the cloud is gravitationally bound, $1 < \alpha < 2$ means the cloud is gravitationally bound however turbulence is non-negligible and $\alpha > 2$ signifies the cloud dynamics are driven by turbulent kinetic energy.

Keeping this in mind we start by looking at the values of α_{Gas} , α_{H_2} and α_{CO} which are derived directly from the simulation and using Equation 6.7. It can be observed that when considering different species, that is a different fraction of the total gas of the cloud, the value of the virial parameter slightly varies. Since we are effectively considering a lesser amount of the total gas, it makes sense that both the mass and the size of the ‘cloud’ will be smaller. However since, proportionally, the difference in mass is much larger than the difference in size, this leads to the cloud appearing to be more unbound when a lower fraction of the gas is considered i.e. a larger value of α . Naturally, when considering lower metallicities this behaviour will be magnified. This follows from the already discussed fact that total H_2 and CO gas are significantly reduced as metallicity is lowered.

It is important to recall that Equation 6.1 is an observationally derived, one-dimensional approximation of the virial theorem. By calculating α_{SOGas} we can test the validity of Equation 6.1 by comparing α_{SOGas} to α_{Gas} since the latter can be considered the ‘true’ value of α as it is derived directly from the three dimensional distribution of gravitational energy and turbulent kinetic energy. Our results show that Equation 6.1 is an acceptable approximation of the three dimensional virial state of the cloud from a one dimensional velocity dispersion. Now when considering other species, as we have done so above, we can see that calculated virial parameter has similar values to their corresponding ‘true’ virial parameter (See Table 6.1). However, it is important to note that α_{Gas} suggest that the cloud is slightly gravitationally unbound while α_{SOGas} suggests its gravitationally bound, this follows from the difference between σ_{Gas} and $\sigma_{z\text{Gas}}$. Lastly, calculating α through this method leaves the final value relatively unchanged as metallicity varies.

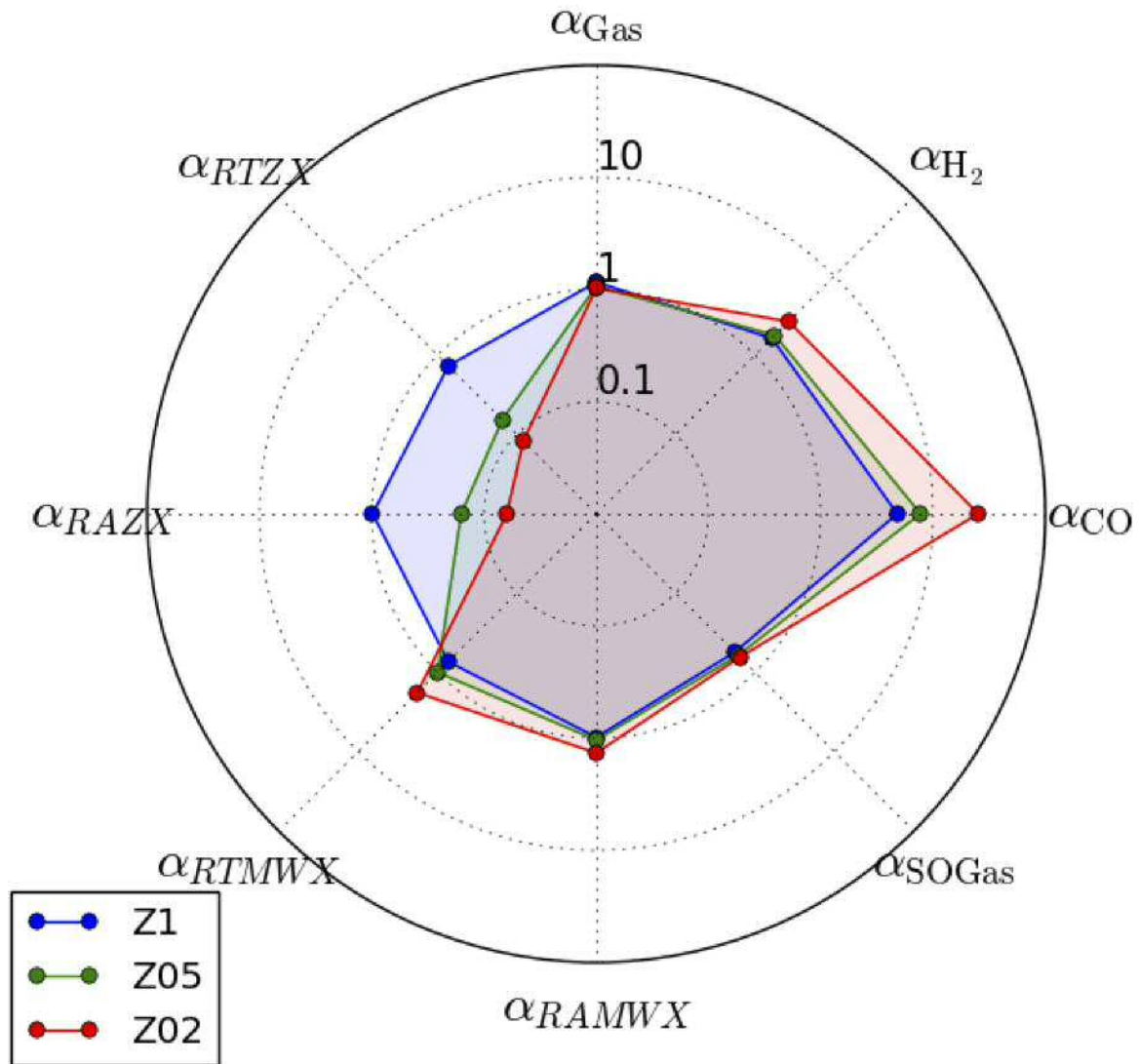


Figure 6.5. Graph showing the different values of α depending on the method used. α_{Gas} , α_{H_2} and α_{CO} represent the virial parameter calculated from the numerical simulations using Equation 6.7. α_{SOGas} is calculated by using Equation 6.1 and σ_{Gas} , R_{Gas} and M_{Gas} which are obtained directly from the numerical simulations. To calculate α_{RAMWX} , α_{RTMWX} , α_{RAZX} and α_{RTZX} we use Equation 6.1 and a different combinations of σ, R and M as derived from the synthetic observations. Finally each color represents clouds at different metallicities

The four remaining values represent variations of α when different observationally derived values of M and R , as discussed from Figure 6.2, are considered. The largest difference in the value of α arises from considering either M_{MWX} or M_{ZX} , in fact one could say that the behaviour is completely inverted. For example, when M_{MWX} is used to calculate the virial parameter (α_{RAMWX} or α_{RTMWX}) then as metallicity is reduced clouds become observationally more unbound. Conversely, the opposite statement can be made when M_{ZX} is used, namely, clouds become significantly more gravitationally bound as metallicity is reduced. These conflicting statements can be easily explained once we understand the uncertainties and biases when observationally deriving mass as explained above. Keeping this in mind is paramount in order to make an accurate assessment of extragalactic star formation where local environmental conditions, such as metallicity, are prone to vary.

On the other hand, α is much less sensitive to changes in size, that is when considering either R_{A} or R_{TB} . Much like the mass, the changes in the virial parameter can be traced back to the results in the middle panel of Figure 6.2. It must however be said that the effect of R on α is small. This could be a consequence of the simple morphology of these clouds. For example, a more elongated, filament-like cloud would have higher uncertainties arising from R_{A} that could conceivably affect the virial parameter.

Finally it can be said that regardless of which value for α we consider there is measurable differences between different methods of calculating the virial parameter. Nonetheless an important consideration should be kept in mind, the virial parameter from simulations is, for the most part, larger than its counterpart derived from the synthetic observations. In other words, clouds appear to be more unbound in simulations than they appear in observations.

6.5 DISCUSSION

6.5.1 ‘TRUE’ VALUES

Throughout this Chapter we have referred to the ‘true’ value of a given quantity to be its corresponding numerically obtained counterpart. However, it is not always clear or straight-forward what this ‘true’ value should be, especially when considering that in most cases there is more than one value from simulations which we could consider ‘true’.

Take for example the ‘true’ values for σ , R and M as described and discussed in the previous Section. In this case, the values that should be used in order to

ID	Z1(MW)	Z05 (LMC)	Z02 (SMC)	Source	Method
		σ^2 [km ² s ⁻²]			
σ_{Gas}	1.17	1.10	1.07	S	Eq. 6.2
$\sigma_{z\text{Gas}}$	0.95	0.98	0.99	S	Eq. 6.2
σ_{H_2}	1.15	1.07	1.03	S	Eq. 6.2
$\sigma_{z\text{H}_2}$	0.95	0.98	1.00	S	Eq. 6.2
σ_{CO}	1.11	0.99	0.82	S	Eq. 6.2
$\sigma_{z\text{CO}}$	0.93	0.92	0.89	S	Eq. 6.2
σ_{Obs}	1.04	0.93	0.79	O	Eq. 6.2
		R [pc]			
R_{Gas}	5.28	5.48	5.61	S	Eq. 6.3
R_{H_2}	5.06	5.15	5.12	S	Eq. 6.3
R_{CO}	4.28	3.83	2.73	O	Eq. 6.3
R_A	5.91	4.24	2.38	O	Eq. 6.5
R_{Tb}	4.41	4.06	3.16	O	Eq. 6.3
		M [M_\odot]			
M_{Gas}	10^4	10^4	10^4	S	$\sum m_i$
M_{H_2}	6.46×10^3	5.05×10^3	2.92×10^3	S	$\sum m_i \chi_{\text{H}_2}$
M_{CO}	2.65×10^3	7.41×10^2	84.6	S	$\sum m_i \chi_{\text{CO}}$
M_{MWX}	7.28×10^3	4.41×10^3	1.61×10^3	O	Eq. 6.6
M_{ZX}	7.28×10^3	2.87×10^4	3.5×10^4	O	Eq. 6.6
		α			
α_{Gas}	1.16	1.07	1.03	S	Eq. 6.7
α_{H_2}	1.63	1.78	2.66	S	Eq. 6.7
α_{CO}	4.80	7.72	25.27	S	Eq. 6.7
α_{SOGas}	0.56	0.61	0.64	S&O	Eq. 6.1
α_{SOH_2}	0.83	1.14	2.04	S&O	Eq. 6.1
α_{SOCO}	1.63	5.06	29.64	S&O	Eq. 6.1
α_{RAMWX}	0.98	1.04	1.36	O	Eq. 6.1
α_{RTMWX}	0.73	1.00	1.80	O	Eq. 6.1
α_{RAZX}	0.98	0.16	0.06	O	Eq. 6.1
α_{RTZX}	0.73	0.15	0.08	O	Eq. 6.1

Table 6.1. All of the results discussed in Section 6.4 are summarised in this table.

calculate α should have been $\sigma_{z\text{CO}}$, R_{CO} and M_{H_2} since they were closely related to the observed value. It is clear, especially by how each of these values is obtained, that doing so would be inconsistent and in no way physically meaningful. This perfectly illustrates how inconsistencies between what is calculated and what is intended to be traced can arise.

Now more to the topic of discussion here, it could be argued that the discussion should be centred on what is the most accurate way of describing the dynamical state of a GMC. It can then be argued that α_{Gas} is the ‘true’ virial parameter since it in considers all the gravitational and turbulent kinetic energy within the simulation. Therefore making it the best way to estimate whether the cloud will keep collapsing and whether it will form stars. Ignoring for a moment the fact the inconsistencies with the definition of ‘molecular cloud’, α_{Gas} suggests that these 3 clouds are almost in virial equilibrium. This is in stark contrast with unbound picture suggest by α_{H_2} or the bound one given by α_{RTZX} .

The conflicting nature of these definitions might be one of the reasons for the ongoing debate on the bound nature of GMCs. A potential way to solve this issue would be to accurately track each of these values of α , as the cloud evolves, therefore leading to a better understanding of which one is the ‘true’ value and more importantly their relation to star formation.

6.5.2 CAVEATS AND LIMITATIONS

There is two important considerations to bear in mind when making these comparisons. The most obvious of these being that GMCs are not created nor do they evolve in isolation. Several different studies have been carried out showing that the formation, evolution and destruction of clouds is directly affected by the surrounding environment and its relation to the galactic structure (Duarte-Cabral & Dobbs, 2016; Smith et al., 2014; Ward et al., 2016). That said, even though full or partial galactic simulations would certainly be desirable for a better comparison with real GMCs, our study here focuses more on the observational techniques and their comparison to simulations.

Another important consideration to be had is the different running times for each cloud. Given our setup, each the evolution of each cloud is tracked until star formation is triggered i.e. a sink particle is formed. This means that when comparing the virial parameters, the comparison is between clouds at different evolutionary stages. It follows then that the dynamical state of these clouds, i.e. the virial parameter, will be different since they are at different stages of evolution. At the same time

it could be argued that the onset of star formation is a dynamically more consistent measure of evolution and therefore it is precisely because of our setup that doing such a comparison is meaningful. Unfortunately to adequately answer this question we would require to track the evolution of different clouds, both numerically and through synthetic observations.

6.6 CONCLUSIONS

We have studied how the virial parameter changes with metallicity and how accurate different observational and numerical techniques are at tracking these changes. To do so, we follow the evolution of 3 numerically modelled molecular clouds with different metallicities ($Z = Z_{\odot}, 0.5 Z_{\odot}, 0.2 Z_{\odot}$) that are then post processed into synthetic observations. Our main findings can be summarized as follows:

1. The velocity dispersion, as observed through synthetic observations, shows a considerable decrease as metallicity is decreased. This follows from the reduced abundance of CO concentrated in the dense regions of the cloud where the velocity dispersion is lower.
2. Our results suggest that to calculate the mass of the molecular gas it is preferable to use a the Milky Way value of X_{aCO} than a revised value that accounts for changes in metallicity. This is because the biases of X_{aCO} and L_{CO} in Equation 6.6 compensate each-other as metallicity changes.
3. To accurately calculate the virial state of a cloud from observations it is important to clearly understand the different biases and uncertainties in its components, namely σ , R and M . Not doing so, as we have shown, can significantly change the value of α and therefore the claim that a GMC is collapsing and will eventually form stars.
4. We find that as the metallicity of the cloud changes, the virial parameter, as derived from the total gas in the simulations, very slightly decreases. That said, when α is calculated for just the molecular gas or from synthetic observations, the value of α does considerably change.
5. The debate between simulations and observations with regards to the bound or unbound nature of GMCs might have a resolution through synthetic observations. Our results show that the same cloud can appear unbound in simulations and bound through synthetic observations.

CHAPTER 7

SUMMARY

7.1 CO LINE RATIOS

In Chapter 4 we studied how the line ratio between the first two rotational transition lines (R_{21}) can serve as a probe of the physical conditions in GMCs. The main results are as follows:

1. We confirm the results from previous work that have shown that the average value for the line ratio is $R_{21} \sim 0.7$. Furthermore we found that R_{21} has a bimodal distribution with a peak centred at the previously recorder value of ~ 0.7 and a second peak centred around ~ 0.3 .
2. There is no observational evidence of the lower centred peak, since the emission associated with this peak is very faint ($T_B < 1\text{Kkms}^{-1}$). However, given the results shown in Figure 4.3 the lower peak of the bimodal distribution should be detectable since it lies just at the edge of current detection limits.
3. The bimodal distribution of R_{21} can serve as a probe of the physical conditions of the gas within a GMC. More precisely, $R_{21} \sim 0.7$ is correlated with cold ($T < 40\text{ K}$), dense ($n > 100\text{cm}^{-3}$) and optically thick ($\tau > 1$) gas. On the other had $R_{21} \sim 0.3$ is correlated with warm ($T > 40\text{ K}$), diffuse ($n < 100\text{cm}^{-3}$) and optically thin ($\tau < 1$) gas.
4. The physical processes driving this correlation are the different excitation conditions for both rotational lines and whether they are being sub-critically excited or in LTE. This difference is highlighted by the line ratio of the two lines.

7.2 ENVIRONMENTAL DEPENDENCE OF CO EMISSION

Following up on the potential of R_{21} being a good tracer of physical conditions, in Chapter 5 we looked at how CO line ratios vary with differing initial conditions as well as environmental conditions. The main results are:

1. After studying changes in different initial conditions, it is clear that the main sources of variations for, not only R_{21} , but CO emission are the ISRF and the CRIR. These environmental changes have the biggest effect since they are the main cause for the destruction of the CO molecular gas. Even though both effects reduce the total amount of CO inside the GMC, their effect on the ratio is different. The ISRF removes any contribution from diffuse unshielded gas while the CRIR regulates the CO inside the cloud lowering the CO total column density.
2. From an extragalactic perspective, where GMCs are unresolved, line ratios are used as conversion factors to convert from W_{CO} to N_{H_2} . Our results show that the average value of R_{21} is a good first approximation for converting W_{21} into W_{10} . However, considerations of the surrounding environment can help reduce the uncertainty when converting between lines.
3. When calculating N_{H_2} , biases to X_{CO} will underestimate the column density when considering high G_0 while biases to R_{21} will underestimate the column density at low G_0 .
4. The effects are similar for line ratios of other lines (R_{21}, R_{31}, R_{32}) since its the same molecular species. Nonetheless, the distribution and average values are different given the the difference in excitation conditions.
5. We confirmed the results by Bisbas et al. (2017) that very high CRIR ($\chi_{\text{H}} \sim 10^{-14}\text{s}^{-1}$) can help regulate CO formation. This is an important result insofar that the chemical modelling used by Bisbas et al. (2017) is different from the one used in our simulations.

7.3 THE VIRIAL PARAMETER

In Chapter 6 we tested how the different techniques and assumptions involved in calculating the virial parameter can affect its final value and therefore its predictive power. The main results are:

1. The velocity dispersion of a GMC decreases as the metallicity of the cloud is decreased, when observed through synthetic observations of the first rotational transition line of CO. This is a consequence of the depleted CO abundance and therefore the more compact nature of the observed clouds.
2. Biases to the X-factor compensate the biases of the CO surface integrated intensity at lower metallicities. This means that when estimating the molecular mass of a GMC ($M_{\text{H}_2} = X_{\text{CO}}L_{\text{CO}}$) it is better to use the Milky Way calibrated X-factor rather than the revised value that accounts for metallicity.
3. How σ , M and R are calculated have a direct impact on the value of the virial parameter α . Therefore understanding the biases and uncertainties is very important in order to strengthen any conclusions made on the dynamical state of clouds and therefore its potential of forming stars.
4. The virial parameter calculated from simulations is systematically larger than the one calculated from synthetic observations. That is the difference between bound GMCs and unbound GMCs might be due to the radiative transfer effects

7.4 FUTURE WORK

The results of this thesis show how synthetic observations, in the context of star formation, can help broaden our understanding of molecular tracers. Moreover they can be used to quantify the different biases and uncertainties in observational techniques. However there is still much work to be done that can help improve our knowledge on GMCs and star formation.

7.4.1 GLOBAL GMC EVOLUTION

One of the questions I am interested in pursuing is: how are GMCs defined? The contrast between a numerical definition and an observational one, as seen in this thesis, can lead to discrepancies between results and it is important to work towards a more universal definition. With this in mind, I intend to address this question by carrying out galactic scale simulations, with AREPO (Springel, 2010), that are able to follow the formation, evolution and destruction of GMCs in a self-consistent manner. Additionally being able to post-process these simulations to create synthetic observations of different molecular tracers will help test their limitations, valid regimes and address misconceptions.

Combined with the growing field of synthetic observations, bridging observations and simulations presents a unique opportunity to address critical questions about the different features of the ISM and their impact on star formation. Are molecular clouds bound? How much does molecular cloud evolution depend on environment? How sensitive are observationally derived star formation efficiencies on the adopted chemical tracer, and are there optical depth/ radiative transfer effects that we are not taking into account? This is key for both galactic and extragalactic star formation.

It is important to note that there has been considerable research on molecular cloud evolution from galactic dynamics (Dobbs, Burkert & Pringle, 2011; Duarte-Cabral & Dobbs, 2016; Smith et al., 2014). However this research has mostly focused on hydrodynamics and cloud formation from a simulation point of view. The intent here would be to build upon this research and strongly focus on the accuracy different molecular tracers have when recovering the physical properties of molecular clouds.

7.4.2 NON-LTE EFFECTS

I am also very interested in further studying radiative processes that can help enhance both the robustness of synthetic observations as well as reduce the computational costs of them. Particularly I am interested in testing the importance of a full non-LTE approach. More specifically quantifying the computational cost of full non-LTE approach and whether a more complete approach can significantly alter synthetic observations.

Another important question is whether an LTE assumption is a good approximation when looking at CO rotational lines from an observational point of view. Rigby et al. (2016) make use of different CO rotational lines as well as CO isotopologues in order to estimate the column densities of molecular clouds. To do so they combine the derived optical depth, the excitation temperature and $^{13}\text{CO}(3-2)$ intensity to create column density cubes. The underlying assumption here is that the emission coming from clouds is in LTE, given the results shown in this thesis this might not necessarily always be the case. It would then be important to be able to quantify in which regimes is LTE applicable to guarantee the accuracy of the derived column densities. Moreover developing new techniques for estimating the column density in non-LTE regimes would be desirable.

BIBLIOGRAPHY

Aravena M. et al., 2010, ApJ, 718, 177

Aravena M. et al., 2014, MNRAS, 442, 558

Ballesteros-Paredes J., 2006, MNRAS, 372, 443

Ballesteros-Paredes J., Klessen R. S., Mac Low M.-M., Vazquez-Semadeni E., 2007, Protostars and Planets V, 63

Barriault L., Joncas G., Plume R., 2011, MNRAS, 416, 1250

Bauermeister A. et al., 2013, ApJ, 768, 132

Begum A., Stanimirović S., Goss W. M., Heiles C., Pavkovich A. S., Hennebelle P., 2010, ApJ, 725, 1779

Bergin E. A., Hartmann L. W., Raymond J. C., Ballesteros-Paredes J., 2004, ApJ, 612, 921

Bertoldi F., McKee C. F., 1992, ApJ, 395, 140

Bigiel F., Leroy A., Walter F., Brinks E., de Blok W. J. G., Madore B., Thornley M. D., 2008, AJ, 136, 2846

Bigiel F. et al., 2016, ApJL, 822, L26

Bisbas T. G., Bell T. A., Viti S., Yates J., Barlow M. J., 2012, MNRAS, 427, 2100

Bisbas T. G., Haworth T. J., Barlow M. J., Viti S., Harries T. J., Bell T., Yates J. A., 2015, MNRAS, 454, 2828

Bisbas T. G., van Dishoeck E. F., Papadopoulos P. P., Szűcs L., Bialy S., Zhang Z.-Y., 2017, ApJ, 839, 90

- Black J. H., 1994, in *Astronomical Society of the Pacific Conference Series*, Vol. 58, The First Symposium on the Infrared Cirrus and Diffuse Interstellar Clouds, Cutri R. M., Latter W. B., eds., p. 355
- Bolatto A. D., Wolfire M., Leroy A. K., 2013, *ARA&A*, 51, 207
- Brand J., Wouterloot J. G. A., 1995, *A&A*, 303, 851
- Brinch C., Hogerheijde M. R., 2010, *A&A*, 523, A25
- Casoli F., Dupraz C., Combes F., Kazes I., 1991, *A&A*, 251, 1
- Castets A., Duvert G., Dutrey A., Bally J., Langer W. D., Wilson R. W., 1990, *A&A*, 234, 469
- Clark P. C., Glover S. C. O., 2014, *MNRAS*, 444, 2396
- Clark P. C., Glover S. C. O., 2015, *MNRAS*, 452, 2057
- Clark P. C., Glover S. C. O., Klessen R. S., 2012, *MNRAS*, 420, 745
- Clark P. C., Glover S. C. O., Klessen R. S., Bonnell I. A., 2012b, *MNRAS*, 424, 2599
- Clark P. C., Glover S. C. O., Ragan S. E., Shetty R., Klessen R. S., 2013, *ApJL*, 768, L34
- Cox D. P., 2005, *ARA&A*, 43, 337
- Daddi E. et al., 2015, *A&A*, 577, A46
- Dale J. E., Ngoumou J., Ercolano B., Bonnell I. A., 2014, *MNRAS*, 442, 694
- Dame T. M., Hartmann D., Thaddeus P., 2001, *ApJ*, 547, 792
- Dame T. M., Thaddeus P., 2011, *ApJL*, 734, L24
- Dib S., Kim J., Vázquez-Semadeni E., Burkert A., Shadmehri M., 2007, *ApJ*, 661, 262
- Dobbs C. L., Burkert A., Pringle J. E., 2011, *MNRAS*, 413, 2935
- Draine B. T., 1978, *ApJS*, 36, 595
- Draine B. T., 2011, *Physics of the Interstellar and Intergalactic Medium*
- Duarte-Cabral A., Dobbs C. L., 2016, *MNRAS*, 458, 3667

- Dullemond C. P., 2012, ASCL, 1202.015
- Eckart A., Downes D., Genzel R., Harris A. I., Jaffe D. T., Wild W., 1990, ApJ, 348, 434
- Elmegreen B. G., 2007, ApJ, 668, 1064
- Evans, II N. J. et al., 2009, ApJS, 181, 321
- Federrath C., Klessen R. S., Schmidt W., 2008, ApJL, 688, L79
- Field G. B., Goldsmith D. W., Habing H. J., 1969, ApJL, 155, L149
- Fryxell B. et al., 2000, ApJS, 131, 273
- Gingold R. A., Monaghan J. J., 1977, MNRAS, 181, 375
- Glover S. C. O., Clark P. C., 2012a, MNRAS, 421, 116
- Glover S. C. O., Clark P. C., 2012b, MNRAS, 421, 9
- Glover S. C. O., Clark P. C., 2012c, MNRAS, 426, 377
- Glover S. C. O., Clark P. C., 2016, MNRAS, 456, 3596
- Glover S. C. O., Clark P. C., Micic M., Molina F., 2015, MNRAS, 448, 1607
- Glover S. C. O., Federrath C., Mac Low M.-M., Klessen R. S., 2010, MNRAS, 404, 2
- Glover S. C. O., Mac Low M.-M., 2007a, ApJS, 169, 239
- Glover S. C. O., Mac Low M.-M., 2007b, ApJ, 659, 1317
- Gnedin N. Y., Tassis K., Kravtsov A. V., 2009, ApJ, 697, 55
- Goldsmith P. F., Heyer M., Narayanan G., Snell R., Li D., Brunt C., 2008, ApJ, 680, 428
- Habing H. J., 1968, Bull. Astron. Inst. Netherlands, 19, 421
- Harries T. J., 2011, MNRAS, 416, 1500
- Hartmann L., Ballesteros-Paredes J., Bergin E. A., 2001, ApJ, 562, 852
- Hartwig T., Clark P. C., Glover S. C. O., Klessen R. S., Sasaki M., 2015, ApJ, 799, 114

- Hasegawa T., 1997, in IAU Symposium, Vol. 170, IAU Symposium, Latter W. B., Radford S. J. E., Jewell P. R., Mangum J. G., Bally J., eds., pp. 39–46
- Haworth T. J., Glover S. C. O., Koepferl C. M., Bisbas T. G., Dale J. E., 2017, ArXiv e-prints
- Haworth T. J., Shima K., Tasker E. J., Fukui Y., Torii K., Dale J. E., Takahira K., Habe A., 2015a, MNRAS, 454, 1634
- Haworth T. J. et al., 2015b, MNRAS, 450, 10
- Heiles C., Troland T. H., 2003, ApJS, 145, 329
- Heyer M., Krawczyk C., Duval J., Jackson J. M., 2009, ApJ, 699, 1092
- Kennicutt R. C., Evans N. J., 2012, ARA&A, 50, 531
- Kennicutt, Jr. R. C., 1998, ApJ, 498, 541
- Keto E., Caselli P., 2008, ApJ, 683, 238
- Klessen R. S., 2000, ApJ, 535, 869
- Klessen R. S., Glover S. C. O., 2016, Star Formation in Galaxy Evolution: Connecting Numerical Models to Reality, Saas-Fee Advanced Course, Volume 43. ISBN 978-3-662-47889-9. Springer-Verlag Berlin Heidelberg, 2016, p. 85, 43, 85
- Koda J. et al., 2012, ApJ, 761, 41
- Koepferl C. M., Robitaille T. P., Dale J. E., Biscani F., 2017, ApJS, 233, 1
- Kulesa C. A. et al., 2013, in IAU Symposium, Vol. 288, Astrophysics from Antarctica, Burton M. G., Cui X., Tothill N. F. H., eds., pp. 256–263
- Larson R. B., 1981, MNRAS, 194, 809
- Leroy A. K. et al., 2009, AJ, 137, 4670
- Liszt H. S., Lucas R., 1998, A&A, 339, 561
- Liszt H. S., Pety J., 2012, A&A, 541, A58
- Lucy L. B., 1977, AJ, 82, 1013
- Maddalena R. J., Morris M., Moscowitz J., Thaddeus P., 1986, ApJ, 303, 375

- McKee C. F., Ostriker E. C., 2007, *ARA&A*, 45, 565
- Nelson R. P., Langer W. D., 1997, *ApJ*, 482, 796
- Nelson R. P., Langer W. D., 1999, *ApJ*, 524, 923
- Nishimura A. et al., 2015, *ApJS*, 216, 18
- Offner S. S. R., Bisbas T. G., Bell T. A., Viti S., 2014, *MNRAS*, 440, L81
- Offner S. S. R., Bisbas T. G., Viti S., Bell T. A., 2013, *ApJ*, 770, 49
- Ossenkopf V., 1997, *New Astronomy*, 2, 365
- Ossenkopf V., 2002, *A&A*, 391, 295
- Ossenkopf V., Henning T., 1994, *A&A*, 291, 943
- Ostriker E. C., McKee C. F., Leroy A. K., 2010, *ApJ*, 721, 975
- Padoan P., Nordlund Å., 2002, *ApJ*, 576, 870
- Papadopoulos P. P., van der Werf P., Xilouris E., Isaak K. G., Gao Y., 2012a, *ApJ*, 751, 10
- Papadopoulos P. P., van der Werf P. P., Xilouris E. M., Isaak K. G., Gao Y., Mühle S., 2012b, *MNRAS*, 426, 2601
- Peñaloza C. H., Clark P. C., Glover S. C. O., Klessen R. S., 2018, *MNRAS*, 475, 1508
- Peñaloza C. H., Clark P. C., Glover S. C. O., Shetty R., Klessen R. S., 2017, *MNRAS*, 465, 2277
- Pellegrini E. W. et al., 2013, *ApJL*, 779, L19
- Peterson D. E. et al., 2011, *ApJS*, 194, 43
- Pineda J. L., Goldsmith P. F., Chapman N., Snell R. L., Li D., Cambrésy L., Brunt C., 2010, *ApJ*, 721, 686
- Pon A. et al., 2016, *ApJ*, 827, 107
- Pontoppidan K. M., Meijerink R., Dullemond C. P., Blake G. A., 2009, *ApJ*, 704, 1482
- Price D. J., 2012, *Journal of Computational Physics*, 231, 759

- Price D. J., Monaghan J. J., 2004, MNRAS, 348, 139
- Reissl S., Wolf S., Brauer R., 2016, A&A, 593, A87
- Rigby A. J. et al., 2016, MNRAS, 456, 2885
- Röllig M. et al., 2007, A&A, 467, 187
- Roman-Duval J., Jackson J. M., Heyer M., Rathborne J., Simon R., 2010, ApJ, 723, 492
- Sakamoto S., Hasegawa T., Handa T., Hayashi M., Oka T., 1997, ApJ, 486, 276
- Sakamoto S., Hayashi M., Hasegawa T., Handa T., Oka T., 1994, ApJ, 425, 641
- Sandstrom K. M. et al., 2013, ApJ, 777, 5
- Sawada T. et al., 2001, ApJS, 136, 189
- Schinnerer E. et al., 2013, ApJ, 779, 42
- Schmidt M., 1959, ApJ, 129, 243
- Schöier F. L., van der Tak F. F. S., van Dishoeck E. F., Black J. H., 2005, A&A, 432, 369
- Scoville N. Z., Yun M. S., Sanders D. B., Clemens D. P., Waller W. H., 1987, ApJS, 63, 821
- Shetty R., Collins D. C., Kauffmann J., Goodman A. A., Rosolowsky E. W., Norman M. L., 2010, ApJ, 712, 1049
- Shetty R., Glover S. C., Dullemond C. P., Klessen R. S., 2011, MNRAS, 412, 1686
- Shetty R., Kelly B. C., Bigiel F., 2013, MNRAS, 430, 288
- Smith R. J., Glover S. C. O., Clark P. C., Klessen R. S., Springel V., 2014, MNRAS, 441, 1628
- Sobolev V. V., 1957, SOVAST, 1, 678
- Solomon P. M., Rivolo A. R., Barrett J., Yahil A., 1987, ApJ, 319, 730
- Springel V., 2005, MNRAS, 364, 1105
- Springel V., 2010, MNRAS, 401, 791

- Springel V., Yoshida N., White S. D. M., 2001, *New Astronomy*, 6, 79
- Steinacker J., Baes M., Gordon K. D., 2013, *ARA&A*, 51, 63
- Szűcs L., Glover S. C. O., Klessen R. S., 2016, *MNRAS*, 460, 82
- Szűcs L., Glover S. C. O., Klessen R. S., 2014, *MNRAS*, 445, 4055
- Takahira K., Tasker E. J., Habe A., 2014, *ApJ*, 792, 63
- Taquet V., Ceccarelli C., Kahane C., 2012, *A&A*, 538, A42
- Tielens A. G. G. M., 2005, *The Physics and Chemistry of the Interstellar Medium*
- van der Tak F. F. S., Black J. H., Schöier F. L., Jansen D. J., van Dishoeck E. F., 2007, *A&A*, 468, 627
- van Dishoeck E. F., Black J. H., 1988, *ApJ*, 334, 771
- Vazquez-Semadeni E., 2009, *ArXiv e-prints*
- Vázquez-Semadeni E., González R. F., Ballesteros-Paredes J., Gazol A., Kim J., 2008, *MNRAS*, 390, 769
- Vlahakis C., van der Werf P., Israel F. P., Tilanus R. P. J., 2013, *MNRAS*, 433, 1837
- Ward R. L., Benincasa S. M., Wadsley J., Sills A., Couchman H. M. P., 2016, *MNRAS*, 455, 920
- Wolfire M. G., McKee C. F., Hollenbach D., Tielens A. G. G. M., 2003, *ApJ*, 587, 278
- Woodall J., Agúndez M., Markwick-Kemper A. J., Millar T. J., 2007, *A&A*, 466, 1197
- Yang B., Stancil, P. C., Balakrishnan N., Forrey R. C., 2010, *ApJ*, 718, 1062
- Zuckerman B., Evans, II N. J., 1974, *ApJL*, 192, L149